Searches for Neutrinos from Fast Radio Bursts and Other Astrophysical Transients with IceCube

By

Samuel Joseph Fahey

A dissertation submitted in partial fulfillment of
the requirements for the degree of

Doctor of Philosophy

(Physics)

at the

UNIVERSITY OF WISCONSIN – MADISON

2018

Date of final oral examination: 29 November 2018

The dissertation is approved by the following members of the Final Oral Committee:

    Justin Vandenbroucke, Assistant Professor, Physics

    Dan McCammon, Professor, Physics

    Keith Bechtol, Assistant Professor, Physics

    Paolo Desiati, Senior Scientist, Physics

Abstract

Advancements in physics and detector technology in the last half-century have enabled the efficient detection of neutrinos for astronomy. The IceCube Neutrino Observatory has detected an astrophysical component of these weakly interacting, neutral elementary particles, but their origins are mostly unknown.

This thesis focuses on analyses that seek to correlate IceCube's neutrino data with astronomical sources detected in electromagnetic channels, in hopes of associating neutrinos with their sources and furthering our understanding of astrophysical source classes. Using techniques designed for transients – objects with highly variable or pulsed emission – analyses of fast radio bursts (FRBs) and of galactic novae are covered in this dissertation.

The analyses presented here produced the first limits on neutrino emission from FRBs and the most constraining current limits for all FRBs discovered through March 2018. Methods particular to millisecond-scale transient analyses are discussed, as well as initial work towards an analysis of galactic novae and miscellaneous analysis-related projects.

Acknowledgements

This dissertation is yet another academic milestone that I owe entirely to an ensemble of friends, colleagues, mentors, and family – all of whom offered only optimism and encouragement if I doubted my abilities as a student. Any positive traits I gained during this work were learned from the ambitious and kind people I am blessed to interact with every day.

To my advisor, Justin Vandenbroucke, thank you for fostering in me an invaluable scientific mindset. With your guidance, I have become a more inquisitive and analytical person, with a careful attention to my audience and to the implications of my every statement and figure. The lessons I have learned under your mentorship will serve me well in many aspects of life: I will set goals more aggressively, communicate more assertively, and above all plot my axis labels so that they may always be read from the back of the room.

To my family – Rachel, Mom, Dad, Matt, Mike, Jackie, and all you other folks – the standards you set for work ethic and dedication to others are monumental. You taught me that one should strive to meet these goals, regardless of ability. With your patience and support, I eventually found implicit motivation and learned to follow your example; and by good fortune, ability followed. Thanks for everything!

Contents

List of Tables

List of Figures

Chapter 1

Multi-messenger Astronomy

Multi-wavelength astronomy – the study of the cosmos in energy bands across the electromagnetic spectrum – has provided scientists with invaluable information in understanding the structure and physical processes of astrophysical sources. In addition to identifying different emission mechanisms and allowing detailed study of source environments, multi-wavelength astronomy led to discoveries which have revolutionized astrophysics and cosmology: pulsars, gamma-ray bursts, and the cosmic microwave background to name a few. In the same vein, advances in detector technology have enabled multi-*messenger* astronomy, whereby many cosmic messengers – electromagnetic radiation, gravitational waves, cosmic rays, and neutrinos – are used to develop a more complete picture of our universe. This section will briefly explain the background for multi-messenger astronomy and motivate the use of neutrinos as unique cosmic messengers for particle astrophysics analyses.

1.1 Cosmic Messengers

1.1.1 Gravitational waves

Gravitational waves are distortions of space-time produced by the extreme acceleration of massive objects, such as close binary systems of black holes and neutron stars. They are the most recent

addition to the list of messengers used in astronomy – first detected in 2015 by the LIGO (Laser Interferometer Gravitational-Wave Observatory) [1] and Virgo collaborations [2], coming from a merger of two black holes that occurred 400 Mpc away from Earth [3]. They were first predicted a century earlier as a result of Albert Einstein's general theory of relativity and had previously only been observed indirectly starting in 1974 through the measured loss of rotational energy in pulsar-neutron star binary systems [4]. Currently, a dozen gravitational wave events have been published; with upgrades to current detectors and the construction of several new observatories (KAGRA [5], IndIGO [6], TianQin [7], etc.) planned, the field of gravitational wave astronomy will be developing rapidly in the next decade.

1.1.2 Cosmic rays

As early as the 19th century, scientists were aware of a pervasive kind of radiation because it caused inevitable discharge of charged objects through ionization of the air; however, the source of the radiation was unknown. In 1911, using a gold-leaf electroscope, Victor Hess discovered during balloon flights that the rate of spontaneous discharge of an electroscope by this radiation increases with altitude [8]. This result suggested that the source of the radiation was extraterrestrial, thus the phenomenon was later named "cosmic rays". Cosmic rays are energetic nuclei and electrons in space which collide with Earth's atmosphere, creating particle showers that can be detected at Earth's surface. The properties of Earth's incident cosmic ray flux have been measured thoroughly across the energy range 1 GeV – 10^{20} GeV, including measurements of the sidereal anisotropy (roughly 10^{-3} in the TeV range [9, 10]), nuclear composition [11], and energy spectrum (scaling as $E^{-2.6}$ to $E^{-3.6}$; see Figure 1-1). However, because cosmic rays are electrically charged, they are deflected by magnetic fields which permeate the galaxy and cannot be directly attributed to an extrasolar source[1]. As a result, an enduring mystery in physics is where and how such high-energy nuclei are accelerated.

---

[1]Only cosmic rays with energies above 10 EeV – 10^{10} GeV – are energetic enough to arrive at Earth without significant magnetic deflection. The Pierre Auger Cosmic Ray Observatory, a surface array of Cherenkov stations covering 3,000 km^2, detects fewer than one event per day in this energy regime [12].
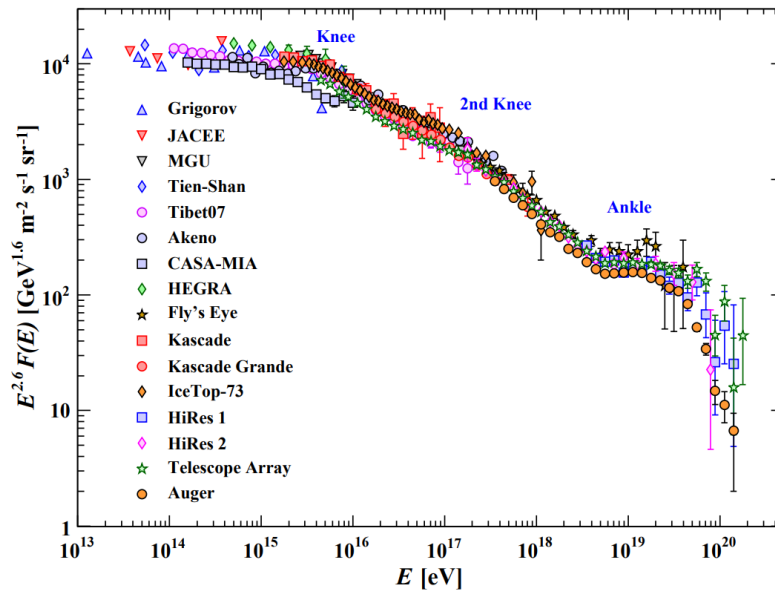
Figure 1-1: The cosmic ray spectrum above 10 TeV is shown, as measured by air shower experiments [11]. The y-axis is weighted by $E^{2.6}$ to accentuate the points where the spectral index changes, perhaps due to a change in dominant cosmic ray source classes between energy regimes.

Compact objects such as black holes and neutron stars are among the most plausible cosmic ray accelerators, because they can harbor high-energy environments by efficiently exploiting the gravitational energy of surrounding matter during accretion. Non-thermal processes are required to explain the cosmic ray energy spectrum in Figure 1-1, so the mechanism by which cosmic rays are believed to reach ultra-relativistic energies is diffusive shock acceleration (DSA). In DSA, particles in a shock front scatter elastically off of a moving magnetic region, gaining momentum from the field. If the environment can reflect these particles upstream, repeated accelerating interactions are possible, resulting in a non-thermal energy distribution among escaping nuclei. Although it is the leading theory for the acceleration of Galactic cosmic rays, there is some tension between observations and theoretical predictions [13, 14]; resolving this tension and explaining the origins of cosmic rays is a foundational goal for multi-messenger astronomy.

1.1.3 Gamma rays

Unlike cosmic rays, gamma rays are high-energy photons and aren't affected by magnetic fields, therefore it is possible to detect gamma ray emission from individual sources. Because Earth's

atmosphere is opaque to gamma rays, direct detection requires sending a telescope into orbit. Starting in 1961 with the Explorer 11 satellite, this method has been continued by satellite telescopes detecting gamma rays in the MeV-GeV energy range, where fluxes are high enough to collect high statistics with compact payloads. Their major discoveries include gamma-ray bursts[2], the Fermi Bubbles [16], and high variability from the Crab Nebula [17]. At GeV-TeV energies, experiments are limited by statistics, so ground-based observatories utilize much larger collection areas to allow detection of gamma rays via Cherenkov light from the products of air showers they induce.

Despite the successes of gamma-ray astronomy in the last half-century, gamma rays don't necessarily provide astrophysicists with a silver bullet for probing the universe's highest-energy environments. For one, gamma rays are produced through both hadronic and leptonic emission mechanisms – as examples, through neutral pion decay and inverse Compton scattering, respectively – so detection of a source in gamma rays may leave ambiguous physical interpretation. Additionally, at TeV energies, the universe becomes opaque to gamma rays at hundreds of Mpc due to interactions with photons of the cosmic microwave background ($\gamma\gamma \to e^+e^-$; see Figure 1-2).

1.1.4 Neutrinos

Fortunately, a third cosmic messenger is produced in astrophysical environments where hadrons are accelerated to relativistic energies. Cosmic rays can collide with other matter or photons, generating intermediate particles that decay into high-energy neutrinos, for example via

$$p + \gamma \to n + \pi^+ \to n + \mu^+ + \nu_\mu \to n + e^+ + \nu_e + \bar{\nu}_\mu + \nu_\mu \tag{1.1}$$

Since neutrinos are electrically neutral and interact weakly with matter, they point back to their source of origin with negligible attenuation. This makes them a useful tool for multi-messenger

---

[2]Gamma-ray bursts were an accidental discovery by the Vela satellites in 1967, which were deployed to monitor ground-based nuclear weapons tests by the Soviet Union [15].
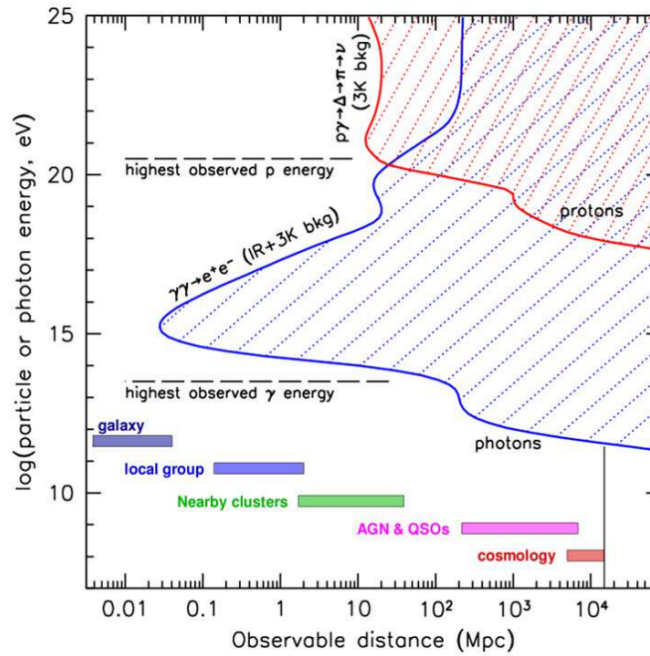
Figure 1-2: The detectable distance of high energy gamma rays is limited by attenuation with infrared and cosmic microwave background photons [18].

astronomy; but of course, their elusive properties also serve as hurdles when trying to detect neutrinos in large numbers.

1.2 Neutrino Physics and Detection

Neutrinos are neutral leptons with flavors corresponding to the charged leptons: electron, muon, and tau. Since the resolution of the solar neutrino problem [19, 20], it has been known that neutrinos must have mass, although it is so small that no experiment has measured it. This is a corollary of the discovery that a neutrino's flavor and mass state oscillates as it travels. In this thesis, I focus on neutrinos that arrive at Earth as muon neutrinos for reasons that will be explained in this section.

Figure 1-3 shows the cross sections for different neutrino-nucleon interactions. In neutral current (NC) interactions, a neutrino scatters with a quark in the nucleon via the Z boson, ejecting the target quark from its nucleus; no new charged particles are created in the process. In charged current (CC) interactions (see example for $\nu_\mu + n$ in Figure 1-4), the neutrino scatters with a
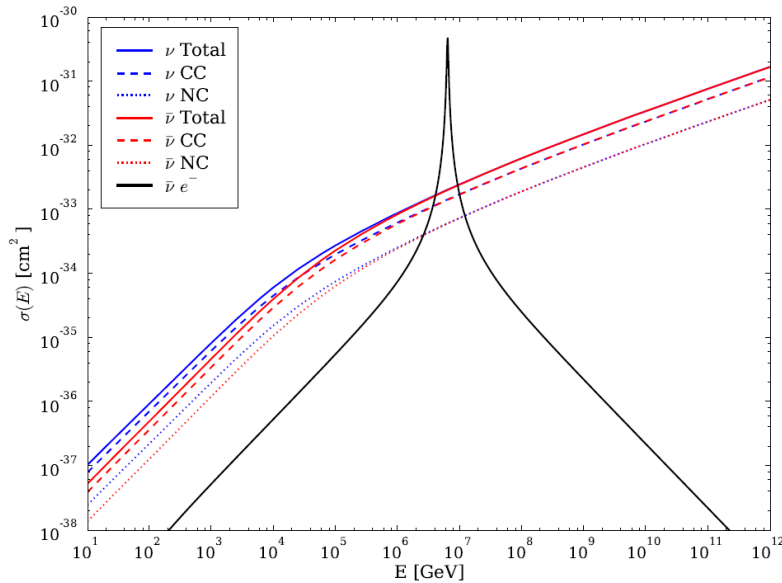
Figure 1-3: Neutrino-nucleon cross sections for neutral current (NC) and charged current (CC) interaction channels [21]. The black curve represents the cross-section for the Glashow resonance, a formation of the W boson that peaks at 6.3 PeV.

quark via the charged W boson, transforming the quark into its oppositely charged counterpart and creating a charged lepton corresponding to the flavor of the neutrino. A muon neutrino that undergoes this process creates a muon, a particle with electron-like properties except 200 times as massive and with a rest-frame lifetime of 2.2 microseconds. Ultra-relativistic muons created this way travel in roughly the same direction as the parent neutrino and can pass through kilometers of solid Earth before decaying or losing their energy. This pointing ability makes charged current interactions of muon neutrinos especially useful for neutrino astronomy, whereas neutral current interactions and charged current interactions of other flavors result in events with more spherical morphologies within a detector.

1.2.1   Cherenkov radiation

When a charged particle travels through a medium faster than the polarization it induces can propagate, its polarization results in a shock front of constructive interference that is observed as Cherenkov radiation. Figure 1-5 shows how this conical shock front forms for a particle traveling
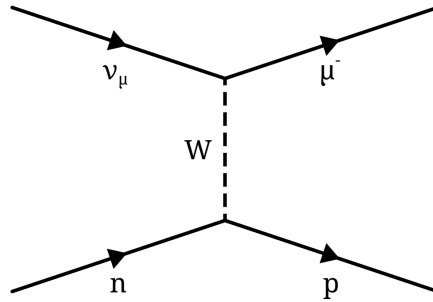
Figure 1-4: Feynman diagram for a charged current interaction

at a speed greater than c/n through a material[3]. The angle at which the Cherenkov wavefront propagates from the path of the charged particle is given by $\cos\theta_C = \frac{1}{n\beta}$. For a particle with $\beta \approx 1$ in ice, $\theta_C \approx 40°$.

The energy loss of a relativistic muon due to Cherenkov radiation is given by the Frank-Tamm equation [23].

$$\frac{d^2E}{dxd\omega} = \frac{e^2}{4\pi}\mu(\omega)\omega\left(1 - \frac{1}{n^2(\omega)\beta^2}\right) \tag{1.2}$$

$\mu(\omega)$ and $n(\omega)$ are the frequency-dependent permeability and index of refraction, respectively. The ω on the right side of Equation 1.2 means that the intensity of radiation is proportional to photon frequency for constant index of refraction. In ice, the index of refraction quickly approaches 1 in the ultraviolet region, causing a peak in intensity at blue-ultraviolet wavelengths [24]. For this reason, photomultiplier tubes in water and ice Cherenkov detectors are optimized to detect photons with wavelengths around 400 nm. This is the main radiative process by which neutrino telescopes observe charged particles from neutrino interactions.

Despite resulting in emission bright enough for muon detection, Cherenkov radiation is a negligible form of energy loss for relativistic muons in matter. Ionizing radiation accounts for orders-of-magnitude greater energy loss – continuous losses of $\sim$200 MeV/m in ice – and is the dominant

---

[3]The oft repeated analogy for this effect is a sonic boom: an aircraft travels through the air faster than the noise it generates can propagate, creating a cone of constructive interference that travels outward from the aircraft's path. Instead of a high-pressure front, the Cherenkov effect is the result of maximal polarization of atoms along the shock front, causing energy to be released through photon emission.
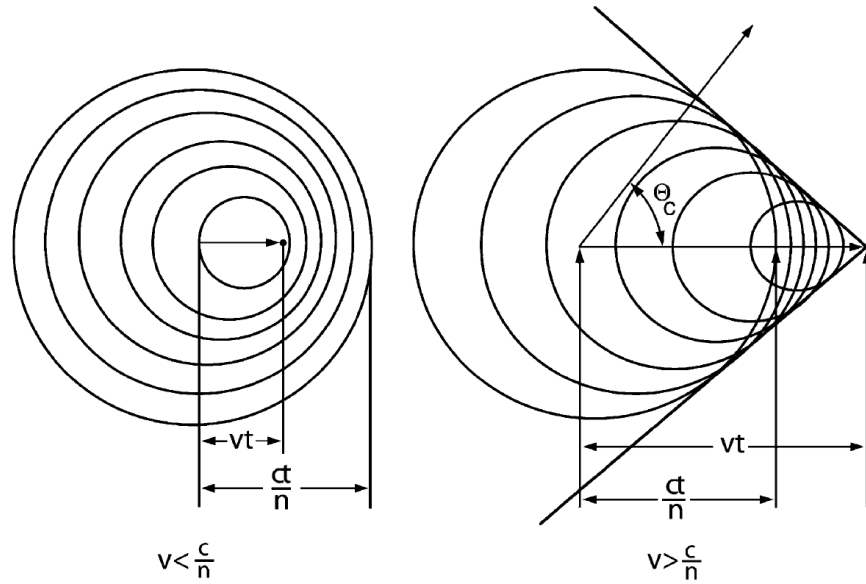
Figure 1-5: *Left:* a particle traveling slower than the speed of light in a medium. *Right:* a particle traveling faster than light in the medium, causing a wavefront where the induced polarization experiences constructive interference. The electrons in the medium at this wavefront emit Cherenkov radiation [22].

process for muons in the GeV energy range. Above 2 TeV, the dominant causes of energy loss are large, stochastic losses from interactions with nuclei: Bremsstrahlung radiation, photonuclear interactions, and e^+e^- pair-production (Figure 1-6). The losses from these interactions scale with muon energy, allowing detectors to more accurately estimate the energy of muons in the TeV energy range.

To efficiently detect neutrinos and their products, a neutrino telescope aims to maximize (1) the number of detector nucleons available for interaction, (2) the instrumented volume for particle shower containment and directional reconstruction of charged products, and (3) the transparency of the detector medium to Cherenkov photons. Intuitively, natural bodies of water and ice provide the most cost-effective medium for the construction of kilometer-scale neutrino observatories.
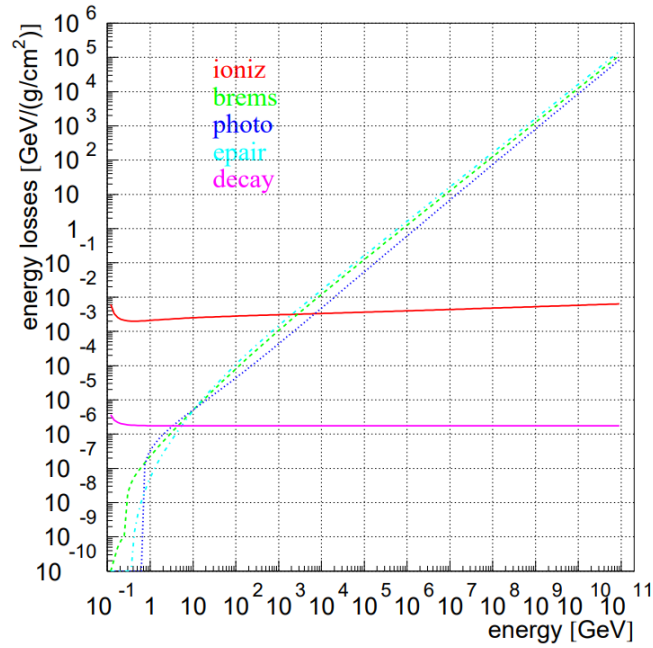
Figure 1-6: Average energy losses by several processes are shown for a relativistic muon in matter [25]. For estimates of energy loss rates in GeV/cm in glacial ice, multiply the y-axis by 0.92 g/cm^3. The "decay" curve is unaffected by this density factor – instead, it represents the product of the muon energy with the probability of muon decay while traveling 1 cm.

Chapter 2

IceCube Neutrino Observatory

2.1 The Detector

The IceCube Neutrino Observatory is a cubic-kilometer neutrino telescope instrumenting a gigaton of Antarctic ice from depths of 1.4 km to 2.4 km beneath the South Pole [26]. The detector consists of 5160 digital optical modules (DOMs) on a total of 86 cables, which are called *strings*. 79 strings make up the main detector array, forming a hexagonal grid with a string separation of 125 m, each with DOM vertical separation of 17 m. The remaining strings complete a denser sub-array in the bottom-center of the detector called DeepCore. At the surface of the ice, 162 ice-filled tanks at 81 total stations comprise IceTop, a cosmic ray air shower array sensitive to cosmic rays in the PeV to EeV energy range. A schematic of the detector is shown in Figure 2-1.

Each DOM (Figure 2-2) contains a $10''$-diameter photomultiplier tube (PMT) facing downward in a spherical glass housing; the top half of the DOM contains circuit boards that perform data acquisition, calibration, communication, and voltage conversion. The PMT is designed for detection of photons in the the wavelength range $300\,\mathrm{nm} - 650\,\mathrm{nm}$ with a peak quantum efficiency of roughly 25% at $390\,\mathrm{nm}$ [26]. When the PMT detects a photon (a "hit"), its waveform is recorded with nanosecond time resolution and digitized by the main board, and the DOM sends a signal to
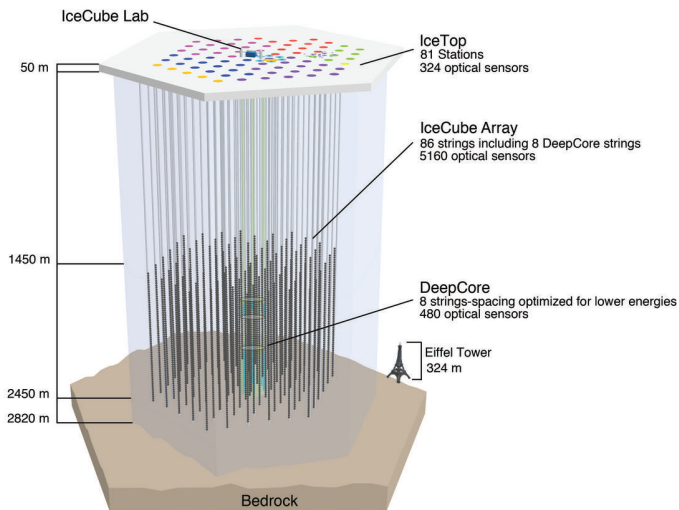
Figure 2-1: IceCube Neutrino Observatory
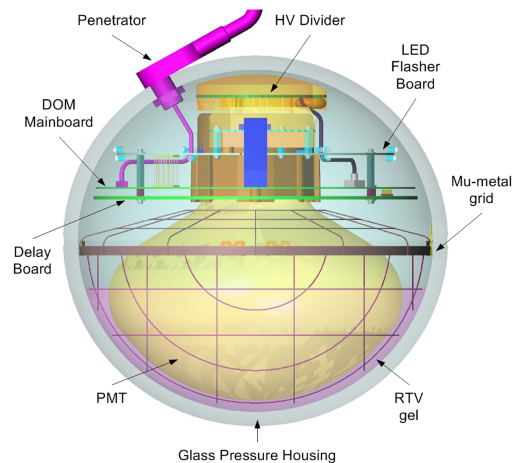
Figure 2-2: Digital optical module

its neighboring DOMs. If a DOM within two vertical spacings on that string records a hit within 1 μs, hard local coincidence (HLC) is satisfied and the compressed waveforms are saved and sent up to the data acquisition system (DAQ) at the surface. Otherwise, for an isolated hit (soft local coincidence, SLC), the waveform is discarded and only the time stamp and charge are sent.

The DAQ runs trigger algorithms at the surface that identify interesting correlation of HLC hits in the detector. For example, a simple multiplicity trigger (SMT) continuously checks if N or more HLC hits occurred anywhere in the ice in a sliding time window of several μs. When a set of hits meets this criterion, the trigger window is expanded until there are no more relevant hits on the HLC DOMs. Then all hits during the trigger window are saved, creating an event. SMT-8 – defined as eight HLC hits in the ice within 5 μs – is triggered at a rate of 2.1 kHz in IceCube[1]. DeepCore and IceTop also have dedicated SMT triggers: 3 HLC hits in 2.5 μs and 6 HLC hits in 5 μs, respectively. Other triggers are tuned to look for unique physics events, like the Slow Particle trigger (SLOP), that attempts to detect magnetic monopoles catalyzing nucleon decays along their trajectories at sub-relativistic speeds.

---

[1]The vast majority of SMT-8 events are triggered by atmospheric muons penetrating the ice from above. These are the dominant form of background for most IceCube analyses.
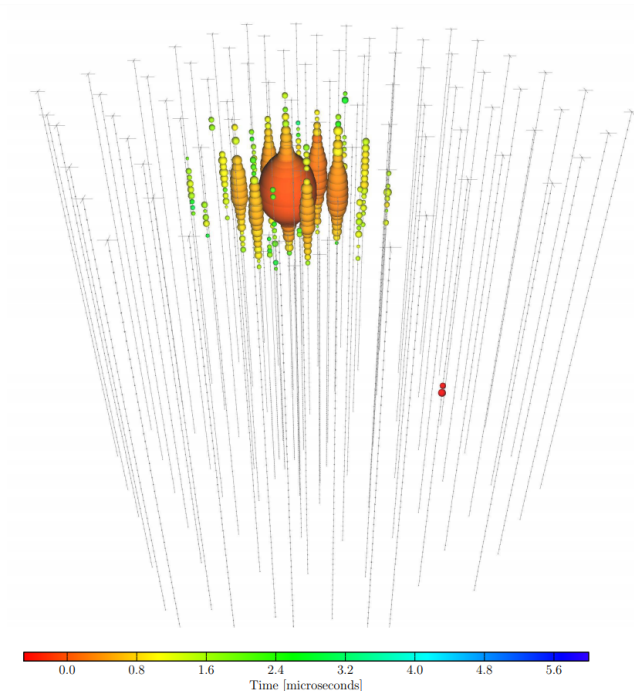
Figure 2-3: A cascade event from a candidate astrophysical neutrino with an energy of about 200 TeV [27].
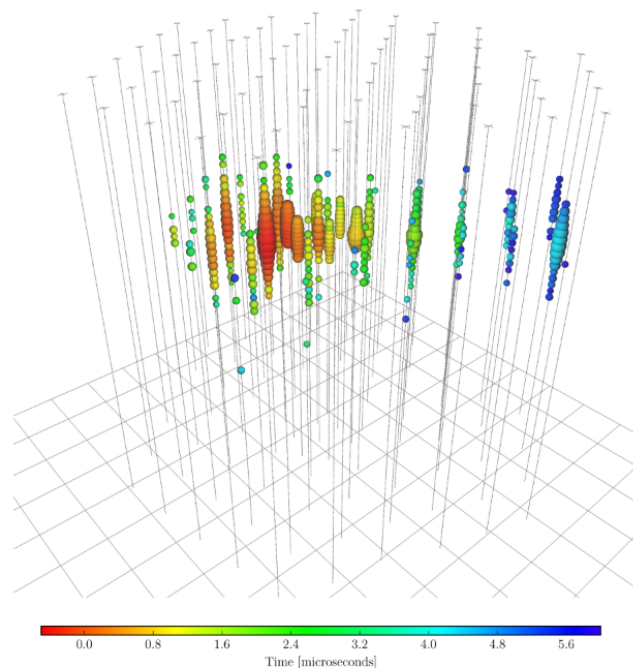
Figure 2-4: A track event from a candidate astrophysical neutrino with an energy of about 200 TeV [28].

2.2 Track Event Reconstruction

Figures 2-3 and 2-4 contrast the event morphologies of cascades and muon tracks with two generously clear examples. While the cascade has an estimated angular error[2] of 11.8°, the angular error of the track event is less than 1°. In a search for correlation of neutrinos with astronomical sources, the background scales with the resolution of the event sample (and thus the square of angular error), making event samples of track-like events more powerful for neutrino astronomy and encouraging development of the best possible neutrino reconstruction techniques.

For a muon neutrino undergoing a charged-current interaction, the expected angle of separation

---

[2]Since many IceCube events are used exclusively for neutrino astronomy, we use "angular error" to mean the statistical uncertainty in the direction of a neutrino causing a given event. Especially for most down-going events, we cannot be certain that a neutrino was involved in creating the observed interactions; however, unless otherwise specified, the angular error refers to σ of a 2-dimensional Gaussian probability distribution function (PDF) for the initial direction of a hypothetical parent neutrino.
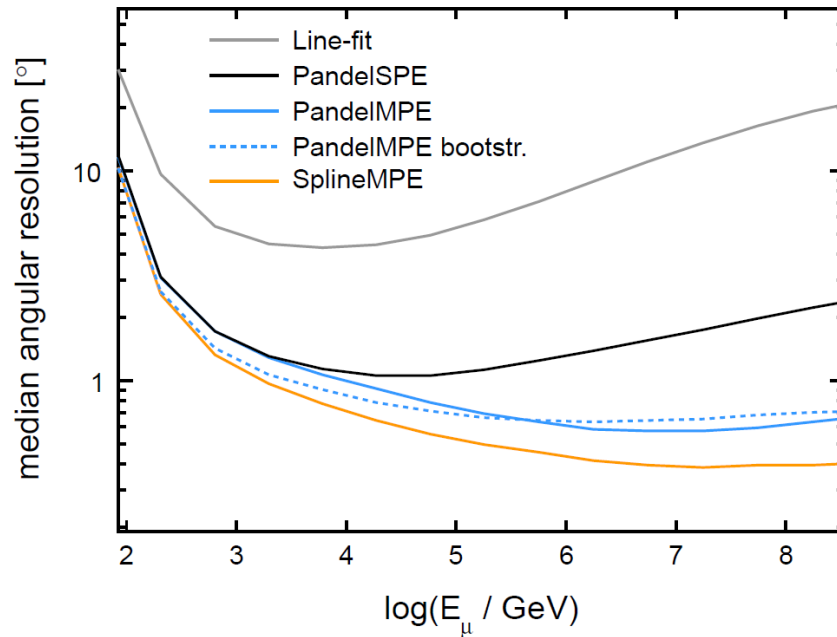
Figure 2-5: A comparison of muon track reconstruction results from increasingly sophisticated algorithms. Kai Schatto discusses each of these fits in depth in his thesis [30].

between neutrino and muon directions is given by [29]

$$\langle \Delta \Psi_{\nu_\mu,\mu} \rangle = 0.7° \left(\frac{E_\nu}{TeV} \right)^{-0.7} \tag{2.1}$$

This sets a physical limit on IceCube's reconstruction accuracy ($\langle \Delta \Psi \rangle \approx 3.5°$ for a ν_μ with $E = 100\,\text{GeV}$), however other uncertainties and statistical limits usually dominate the angular error.

The simplest track fit assumes plane-wave propagation of Cherenkov photons in the ice, ignoring scattering and absorption. This fit can be solved analytically by minimizing the total time residual from all hits in the event. Its performance is plotted in Figure 2-5 as "Line-fit".

To improve track fits, we use a likelihood method to take into account probabilistic uncertainties in photon propagation, often using the line fit as a seed. The Pandel likelihood function takes into account the distance of the track hypothesis from each DOM, as well as photon propagation specifically to the underside of each DOM, when calculating time residuals. The default best

track fit available in Level 2 IceCube data is PandelMPE[3], but for every analysis in this thesis a more sophisticated fit has also been performed; for each analysis of fast radio bursts, SplineMPE (see Figure 2-5) provides the best-fit neutrino direction. For detailed discussion of these track reconstruction algorithms, Kai Schatto's thesis is an excellent resource [30].

2.3   Astrophysical Neutrino Flux

IceCube has detected a flux of astrophysical neutrinos, consistent with isotropy, in the form of a significant excess of high-quality events at energies above 25 TeV [31, 28, 32][4]. A purely atmospheric origin of this excess is rejected with high significance ($> 6\sigma$, [34]), yet searches for steady neutrino emitters – via auto-correlation of data (clustering searches) and cross-correlation with known astrophysical objects – have not discovered a source.

In 2017, IceCube sent an automatic alert for a neutrino event with high probability of astrophysical origin ("IceCube-170922A"), suggesting multi-messenger follow-up in the direction of the event's reconstruction. Gamma-ray observatories MAGIC and *Fermi* soon found the blazar TXS 0506+056 flaring in its highest recorded state of gamma-ray activity [35, 36]. An archival study of this direction by IceCube then discovered a separate significant ($> 3\sigma$) excess of neutrino events from 2014–2015; during this flare, however, TXS 0506+056 was not found to be flaring in gamma rays. This marked the first high-energy astrophysical neutrino emitter ever discovered, but despite this development, blazars remain disfavored to cause the majority of IceCube's diffuse astrophysical flux between 10 TeV and 2 PeV [37].

Untriggered searches for transient neutrino emission have also been unable to identify sources [38],

---

[3]MPE stands for multiple photo-electron, meaning the likelihood fit uses every hit in the event. SPE (single photo-electron) fits use only the first hit on each DOM for faster optimization with comparable results at energies below 10 TeV.

[4]This excess is measured relative to a background of atmospheric neutrinos, which have a softer spectrum than the diffuse astrophysical neutrino flux. Below 500 TeV, the conventional atmospheric spectrum is one power of energy steeper than the cosmic ray spectrum because higher-energy particles are more likely to interact before decaying, resulting in an $E^{-3.7}$ spectrum. Above 500 TeV, contributions from so-called *prompt* neutrinos are theorized to dominate, resulting from decay of very short-lived charmed mesons and following the $E^{-2.7}$ cosmic ray spectrum more closely [33]

and the contribution from the Milky Way to IceCube's astrophysical neutrino flux is constrained to less than 14% (90% confidence level) [39]. Gamma-ray bursts, once thought to be promising candidate sources of ultra-high-energy cosmic rays, are limited to contributing less that 1% of the astrophysical neutrino flux [40]. Furthermore, in an untriggered search for multiplets of directionally consistent track-like events, the population density of a minute-scale transient source class contributing all of the observed flux is constrained to more than 10^{-5} Mpc^{-3} yr^{-1}, ruling out rare sources like long gamma-ray bursts and binary black hole mergers [41]. These null results motivate a search for correlation of neutrino data with a mysterious extragalactic source class of higher rate density, such as fast radio bursts (estimated $R_{FRB} = 4.8 \cdot 10^{-4}$ Mpc^{-3} yr^{-1}, [42]).

Chapter 3

Fast Radio Bursts

3.1   History of Detections

Astrophysical radio waves were first detected by Karl Jansky – who earned his bachelor's degree in physics from the University of Wisconsin-Madison and later became a professor of electrical engineering there – in 1931. The development of radio astronomy thereafter has led to many major discoveries, including the cosmic microwave background in 1964 [43] and pulsars in 1967. Pulsars, first discovered by Jocelyn Bell Burnell and Antony Hewish, are rotating neutron stars with beamed emission, causing a pulsed effect to an observer in the beam's path. More than 2500 pulsars have been discovered in the Milky Way, but none have been found outside of our Galactic neighborhood [44]. Searches for pulsars typically rely on their periodicity to distinguish signal from noise; but starting in the early 2000s, surveys for single short radio pulses became possible, leading to the discoveries two new transient source classes.

The first is rotating radio transients (RRATs), discovered in 2006 [45]. These are a Galactic population of transients that emit sporadically, but with an underlying periodicity determined by the neutron star's rotational period [46, 47][1]. The second discovery, in 2007, is of fast radio bursts: an enigmatic source class on which this chapter is focused.

---

[1] See source list and properties in the "RRATalog" – the RRAT catalog: http://astro.phys.wvu.edu/rratalog/
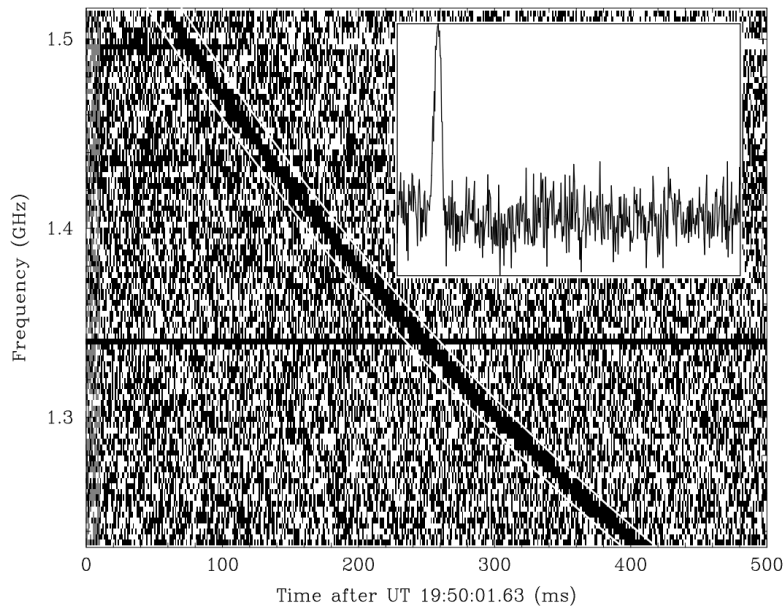
Figure 3-1: The Lorimer Burst [48]. The main panel shows the signal arriving in lower frequencies at later times, closely matching the dispersion expected from a signal passing through free electrons during its transit. The smaller panel shows the combined signal from all frequencies after correcting for the dispersion effect.

3.1.1 The Lorimer Burst (2007)

Fast radio bursts (FRBs) are a class of astrophysical phenomena distinguished by bright millisecond-scale radio emission at GHz frequencies. Their discovery was made possible only recently by computational advances that allowed radio telescopes to survey for pulsars with increased time and frequency resolution. In 2007, Lorimer et al. reported the first FRB to be discovered, in 1.4-GHz archival data from a 2001 pulsar survey of the Magellanic clouds by the Parkes radio telescope in Australia [48] (Figure 3-1). FRB 010724, sometimes referred to as the Lorimer burst, had an estimated peak flux of 40 Jy and a dispersion measure (DM, see Section 3.2) – the integrated column density of free electrons along the signal path causing a delay in the arrival time of lower frequency signal components – of $375\,\mathrm{cm}^{-3}\,\mathrm{pc}$. This number is significantly larger than the diffuse plasma in the Milky Way alone could account for at the FRB's Galactic latitude ($25\,\mathrm{cm}^{-3}\,\mathrm{pc}$) and almost twice the largest observed DM among radio pulsars in the Magellanic clouds ($205\,\mathrm{cm}^{-3}\,\mathrm{pc}$), suggesting the signal might be extragalactic.

3.1.2   Perytons and FRBs (2010 - 2015)

Three years after the Lorimer burst was reported, Burke-Spolaor et al. published the discovery of 16 new bright, frequency-swept events by the Parkes radio telescope which showed clear evidence of terrestrial origin [49]: all 13 of the telescope's receivers detected the events with similar intensity, an impossibility for an on-axis point-like source. The exact cause of the new bursts, dubbed "perytons", was unknown at the time but cast significant doubt on arguments favoring the extragalactic origin of FRB 010724. In July 2014, after several more FRBs had been discovered only by Parkes, Spitler et al. reported the detection of FRB 121102 by the Arecibo Observatory located in Puerto Rico [50]; the detection of a bright 3-millisecond FRB with characteristically large DM by a second telescope made FRBs' astrophysical origins more plausible. Moreover, less than a year later, the source of the perytons had been found. The wide-field radio bursts whose frequency-swept signals closely resembled the dispersion measure of an extraterrestrial signal were noticed to occur more frequently during the Parkes telescope's office hours, especially on weekdays around lunch time [51]. The source of the FRB-mimicking perytons was determined to be the magnetron in the site's microwave oven, creating the signal during the immediate shut-down following a premature opening of the oven door during operation. Comparisons of distributions of perytons and FRBs in time and DM confirmed that the sources were unrelated and that FRBs were likely astrophysical. Later in 2015, the discovery of FRB 110523 by the Green Bank Telescope in the United States was reported [52], and by the end of that year, 17 FRBs had been discovered by three separate telescopes. Their DMs and detected fluence[2] were consistent with those expected from a uniform distribution of extragalactic sources [53].

3.1.3   FRB 121102: The repeating FRB

When FRB 121102 was discovered via Arecibo's PALFA survey, it became the first FRB detection by a telescope other than Parkes [50]. It was detected in the Galactic anti-center region with a dispersion measure $DM = 557\,\mathrm{pc\,cm^{-3}}$, roughly three times the maximum expected diffuse Galactic

---

[2]time-integrated energy flux; refer to Section 3.5

DM along its line of sight. Still, the possibility remained that the source of the burst was a Galactic rotating radio transient, perhaps with an unusually dense local environment. It was for this reason that the Parkes telescope had previously been used to monitor the locations of eight discovered FRBs in search of repeated emission [54]; in 110 hours of total observation, no repeated bursts were detected. A follow-up observation was planned for spring 2015 of the location of FRB 121102, and in just 3 hours, 10 new bursts were detected from the source direction, each with DM and pulse properties consistent with the original FRB 121102 [55].

Though no pattern could be easily seen in the bursts' arrival times, it was clear that these detections ruled out models for FRB 121102 which were cataclysmic, like evaporating black holes [56] and the collapse or merging of neutrinon stars [57][58].

3.2   Dispersion Measure

As an electromagnetic signal propagates through a plasma such as in the interstellar medium (ISM), its speed is frequency-dependent due to dispersive effects. For signals with frequency $\nu \gg \nu_p$ – the plasma frequency, which for the ISM is on the order of kHz – the time delay relative to an infinite-frequency signal is

$$\Delta t = \frac{e^2}{2\pi m_e c \nu^2} \int n_e(l) dl = \frac{e^2}{2\pi m_e c \nu^2} \cdot \mathrm{DM} \tag{3.1}$$

where the dispersion measure (DM) is defined as the integral of the number density of free electrons along the signal's path.

$$\mathrm{DM} \equiv \int n_e(l) dl \tag{3.2}$$

For astronomers observing a pulsed source emitting across a range of lower frequencies ($\sim$GHz range, as opposed to $>$THz), the time delay of signal components is readily calculated; this method is widely used for studying pulsars. From the time delay, the DM itself is easily obtained and can be used to study properties of the source and its environment [59, 60] and of the Milky Way itself
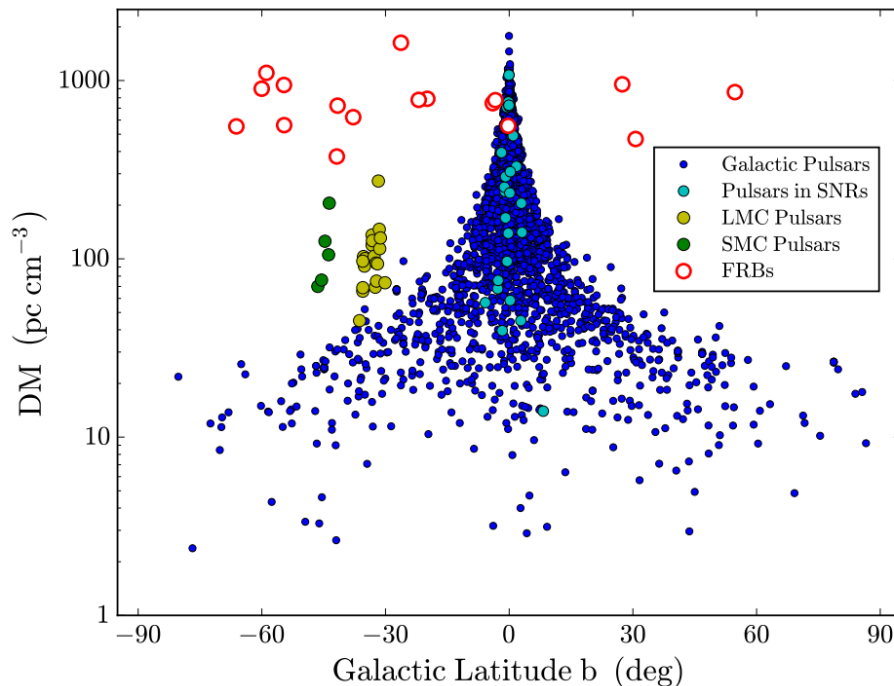
Figure 3-2: Dispersion measures of the first 17 FRBs compared to those of the local pulsar population. Cordes et al. argue that the distributions of FRB DMs are most consistent with a extragalactic source class hypothesis [62].

[61]. Figure 3-2 shows that for FRBs, the values of DM aren't strongly dependent on Galactic latitude as is the case for Galactic pulsars. Without evidence of strong contributions to the DM from the immediate source environment [62, 63], this suggests that FRBs must be extragalactic.

Rate $(\text{sky}^{-1}\text{d}^{-1})$; C.L.	frequency	radio fluence (Jy ms); width (ms)	source
$7^{+5}_{-3} \times 10^3$; 95%	1.4 GHz	0.13; $0.128 - 1.5$; 16	[64]
$4.4^{+5.2}_{-3.1} \times 10^3$; 99%	1.4 GHz	4.0; n/a	[65]
$0.78^{+1.24}_{-0.57} \times 10^2$; 95%	843 MHz	>11; $0.655 - 42$	UTMOST, [66]
37 ± 8; 68%	1.3 GHz	>26; <1.26	ASKAP, [67]

Table 3.1: A list of recent all-sky FRB rate estimates. Measurements depend on the reference frequency of observation, the radio energy fluence incident at Earth, and the maximum pulse width searched in surveys.

3.3   Outlook for FRB Discoveries

The reported rate of FRB events each day depends on the radio frequency and brightness to which a radio observatory is sensitive. Table 3.1 shows that the rates quoted for parameters relevant to single-dish telescopes are between 10^3–10^4 sky^{-1}d^{-1}; for interferometers, a larger fluence is needed for high signal-to-noise, so the rate is smaller as reported. Despite the implied occurrence rate of FRBs, the Parkes telescope (beam width $0.25°$) requires roughly ten days of observation to detect a single FRB [68].

Fortunately, newly operating observatories boast orders-of-magnitude larger fields of view and anticipate substantial additions to what is currently a rather small source list. As of October 2018, the Australian Square Kilometre Array Pathfinder (ASKAP) has discovered 20 FRBs using a survey with a 30 deg^2 field of view [67]. In the northern sky, where detections are sparse so far, the Canadian Hydrogen Intensity Mapping Experiment (CHIME) expects to detect more than one FRB per day using a >200 deg^2 field of view interferometer [69]; its first reported detection is FRB 180725A (ATel 11901).

3.4   Multi-messenger Follow-up

In 2016, Delauney et al. reported the detection by Swift of a gamma-ray transient coincident with FRB 131104 [70], finding a directionally coincident flare 300 seconds after the radio burst. Although a significance of 3.2σ was reported, the search which initially intended to analyze four sources was stopped after a search of the first source returned significant results (thereby avoiding a trials penalty), and the p-value was calculated a posteriori in time and space. Assuming the Swift transient is a gamma-ray counterpart to FRB 131104, a comparison of the all-sky rates of FRBs and comparable gamma-ray transients finds it would be a unique one; only one in roughly 500 FRBs could possibly be associated with a comparable Swift-detected transient due to the disparity in their observed rate [71]. Additionally, in a follow-up using archival gamma-ray data from *Fermi*-LAT, no significant coincidence was found with any of 15 FRBs, including FRB 131104

for a time window of roughly 1.5 to 3 hours after radio detection [72].

Archival searches for a multi-messenger counterpart to FRB 121102 found an extragalactic optical source with a chance probability $< 3.5 \times 10^{-4}$; no infrared or X-ray counterparts were found [73]. This was done by first improving the Arecibo localization by three orders of magnitude, using data from the Karl G. Jansky Very Large Array (VLA). Despite its unique repeating behavior, FRB 121102 and its host galaxy provide a wealth of information for follow-up studies, allowing thorough inspection of a source environment capable of creating short, non-periodic radio bursts [74].

In the neutrino sector, archival searches for neutrino events coincident with FRBs have been conducted with IceCube [75, 76] – these analyses were led by myself and colleagues and are discussed in this dissertation – and ANTARES [77]; none have found evidence of neutrino emission, but as will be discussed in this thesis, that may be due to statistical limitations from the small number of detected sources.

3.5 Defining "Fluence"

"Fluence" is used to refer to the time-integrated form of an observed rate, usually a flux. Since the term "flux" carries its own subfield-specific tendencies, the use of "fluence" without modifiers can cause confusion and should be avoided.

$$\mathscr{F} = \int F(t)dt \rightarrow [\mathscr{F}] = [F][time] \tag{3.3}$$

For example, in neutrino astrophysics, we often use "flux" to refer to a particle flux with units such as $\mathrm{GeV}^{-1}\ \mathrm{cm}^{-2}\ \mathrm{s}^{-1}$; this fluence would have units of $\mathrm{GeV}^{-1}\ \mathrm{cm}^{-2}$. In radio astronomy, however, "flux" refers to an energy flux with units in the form of $\mathrm{erg}\ \mathrm{cm}^{-2}\ \mathrm{s}^{-1}\ \mathrm{Hz}^{-1}$ [53]. Since the messenger they detect isn't as countable as neutrinos or high-energy photons, their flux is already energy-integrated, and the corresponding fluence has units such as $\mathrm{erg}\ \mathrm{cm}^{-2}\ \mathrm{Hz}^{-1}$.

The confusion between definitions is especially problematic because of our tendency to report a

particle fluence multiplied by E^2 (e.g., in [78]). This is done to make spectral shapes with $\gamma \approx -2.5$ easier to compare and analyze, but it also results in plotted units of GeV cm^{-2} – the same units an astronomer might expect if the fluence were derived from an energy flux and integrated over the bandwidth – and worse yet, we often ignore the factor of E^2 and call the entire value $E^2\mathscr{F}$ simply "fluence". This can be ameliorated by initializing uses of "flux" or "fluence" in any paper with the appropriate modifier: "particle", "energy", "mass", etc. Alternatively, if a paper might attract attention from subfields with varying definitions, "fluence" should be avoided altogether in favor of "time-integrated flux" where the flux is defined as "particle flux".

3.6   Theoretical Models

Due to a scarcity of detections and observational constraints, there are many competing models for FRBs. From basic source properties – their brightness at extragalactic distances and brevity of outbursts – most models involve compact sources $(R < 10^3 \text{ km})^3$ with beamed emission [79]. Although models do not currently delve into the implications for neutrino observations, some directly result in or imply qualitative radio-simultaneous neutrino emission. Examples of these models are binary neutron star mergers [58], neutron stars collapsing into black holes ("blitzars") [57], and collapse of a normal hadronic crust onto a strange (as in the quark flavor) star [80]. All of these require cataclysmic scenarios, thus assuming FRB 121102 to have a separate physical explanation to allow repetitions. A model that may incorporate all FRBs is a neutron star colliding with an asteroid or comet [81], whereby radio emission is the result of immediate plasmafication of material in a strong magnetic environment. FRB 121102 would then represent a unique case of a neutron star passing through an asteroid belt [82].

For a catalog of dozens of working hypotheses for FRB origins and just a few models that have so far been ruled out by subsequent discoveries, I recommend "A Living Theory Catalogue for Fast Radio Bursts" by Platts et al. [83]. In this thesis, I present analyses which test the cases

---

[3]If a pulse of duration 3 ms were produced by some object, the maximum difference in distance from which the pulse originates is 3 ms $\times c = 900$ km in the simplest case – an instantaneous isotropic burst of emission.

in which neutrino emission from FRBs is predicted; however, because no model gives quantitative predictions on the flux or radio-relative timing of neutrino emission, only generic temporal and spatial correlation is considered.

Chapter 4

One-year FRB Search

This chapter briefly summarizes an analysis of four FRBs with one year of IceCube data; it was the first search for neutrino emission from FRBs. The results were published in August 2018 in *The Astrophysical Journal* [75], and the paper can be found in Appendix E.

4.1 Point Source Data Sample

The data[1] consist of 138,322 neutrino candidate events from May 2011 to May 2012, each provided with event time in integer-truncated Modified Julian Date (MJD) along with estimates of neutrino energy, direction, and reconstruction error. We performed a search for neutrino emission from four FRBs detected during the time of the event sample.

4.2 Binned Analysis Method

From the list of FRBs that were later analyzed in the six-year analysis (see Appendix F), four occurred in this year of data (Figure 4-1). Since the event times were provided at day-precision, we defined the condition for temporal coincidence as an event and FRB sharing the same time

---

[1]data was previously used in a four-year search for point-like sources of high-energy neutrino emission [84]; see https://icecube.wisc.edu/science/data/PS-IC86-2011
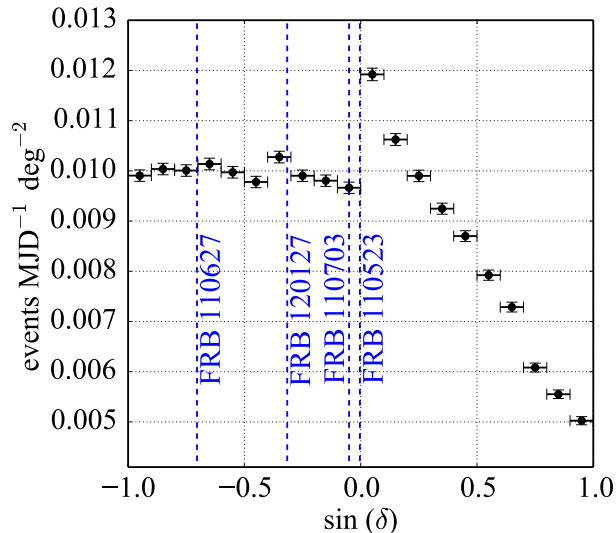
Figure 4-1: The event rate of this event sample is shown versus declination, averaged over right ascension within each declination band. The declination of each FRB is shown for reference. [75]

in integer-truncated MJD. A back-of-the-envelope background estimate informed our choice of analysis method with regard to spatial coincidence: assuming 0.01 events per day per square degree at each FRB location, and an average angular error – the standard deviation of a 2-D Gaussian PDF describing the initial neutrino direction of each event – less than $\sigma = 1°$ (Figure 4-2), one would expect fewer than 0.13 [2] events per day within σ of any of the four FRBs. It was determined that if no events were found within σ of an FRB, non-detection would be reported along with upper limits on the neutrino emission from each source. However, if one or more events were found to be coincident with an FRB, the significance would be calculated a posteriori.

For each time-coincident event, the angular separation between its reconstructed direction and the direction of its coincident FRB was calculated and compared to its estimated angular error. In every case, the angular separation was found to be larger than its angular error – defined as the radius which contains 50% of the event reconstruction's point spread function (PSF) – fulfilling our criteria for non-detection. Figure 4-3 shows all coincident events in the region of each FRB; no FRB lies within even the 99%-PSF-containment region for any coincident event.

---

[2] $\langle N_{BG} \rangle = 4 \cdot 0.01 \; day^{-1} \; deg^{-2} \cdot \pi (1 \; deg)^2 = 0.13 \; events \; day^{-1}$
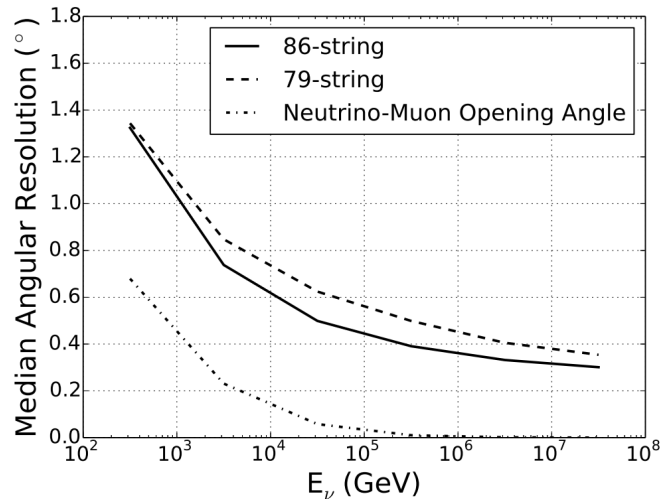
Figure 4-2: From IceCube's four-year point source search [84], the median resolution – the angle between an event's reconstructed direction and its true neutrino direction from simulation – is plotted versus neutrino energy. The median angular error assigned to experimental data events is $0.60°$ (the central 80% interval is $[0.20°, 2.2°]$).
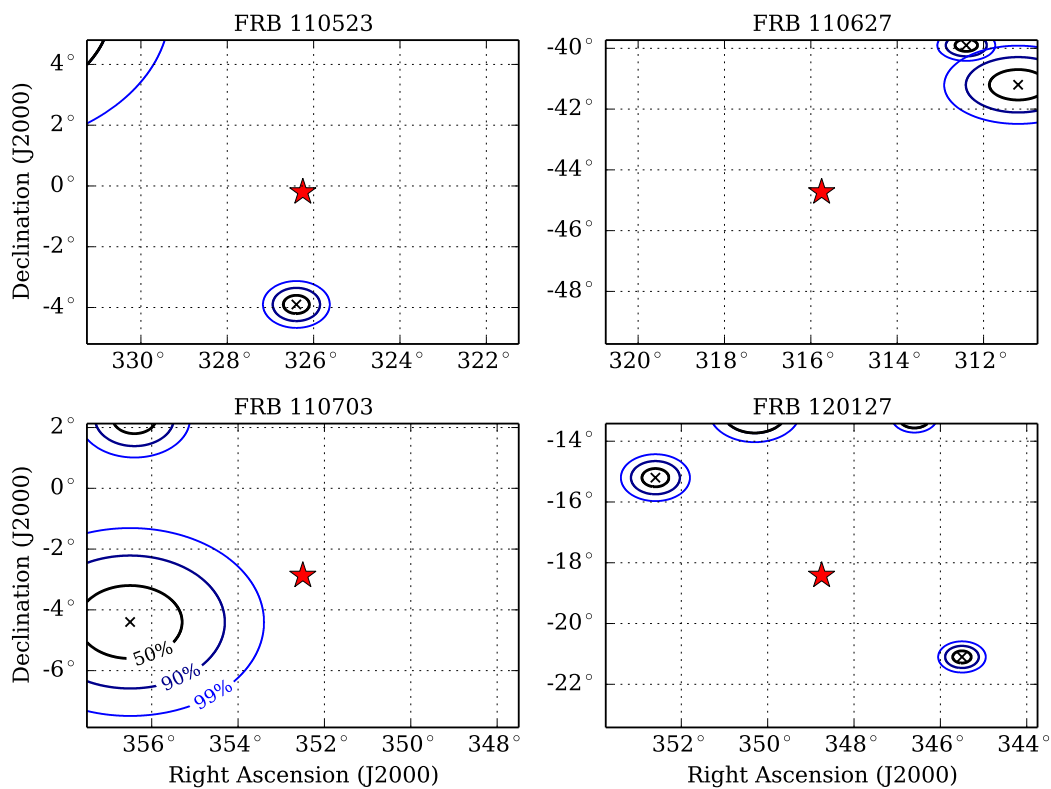
Figure 4-3: For each FRB ($\star$) in this analysis, a $10° \times 10°$ grid shows all nearby time-coincident events ($\times$). Three error circles are shown for each event, depicting 50%-, 90%-, and 99%-PSF containment properly projected onto the sphere. [75]
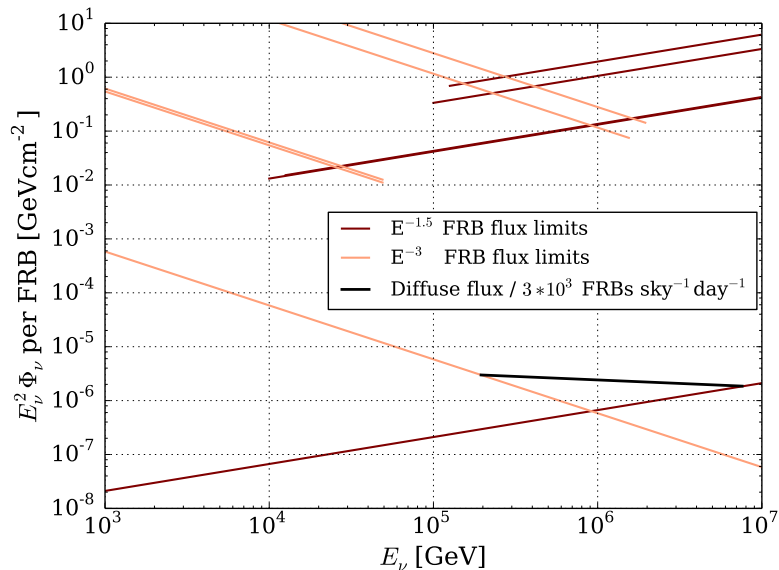
Figure 4-4: The non-detection results limit the maximum neutrino flux emitted by these FRBs over one day (with 90% confidence level). The pairs of flux lines at the top of the figure represent limits on an $E^{-1.5}$ (dark red) and E^{-3} (peach) flux from each FRB analyzed. The black line and the pair of lines it constrains show the limits inferred from IceCube's diffuse neutrino flux measurement and an estimate of 3×10^3 FRBs per day [75]

In the case of non-detection, we set upper limits on the neutrino emission from each FRB individually. Convolving an unbroken power-law neutrino flux ($\Phi_\nu \propto E_\nu^{-\gamma}$) with the event sample's effective area returns an energy distribution of hypothetically detected neutrino events (integrated over one day); the flux normalization that sets the energy-integrated sum to 2.3 events is the 90% Poisson upper limit on an observation of zero events. Figure 4-4 shows the power-law flux limited by non-detection for the hardest ($E^{-1.5}$) and softest (E^{-3}) energy spectra we considered. For this analysis, constraining a homogeneous source class of 3,000 FRBs per day to causing no more than 100% of IceCube's diffuse astrophysical neutrino flux sets limits orders of magnitude more stringent than the analysis sensitivity is capable.

Chapter 5

Six-year FRB Analysis

In April 2018, the results of this analysis were published in *The Astrophysical Journal* [76]; the paper can be found in Appendix F. 38 bursts from 13 unique directions were studied, spanning six years of IceCube data up until September 2016. In this section, I avoid repeating what is covered in the paper and instead focus on important details and discussion which were not included in the paper.

5.1   Transient Test Statistic

The test statistic (TS) for analyses of transients is derived by including a Poisson term in the standard IceCube point source TS [85]. It is described in detail in Appendix B, and it has been used in previous IceCube analyses in search of neutrino emission from gamma-ray bursts (see the theses of Mike Richman [86] and Ryan Maunu [87]).

Essentially, a steady-source analysis assumes that on timescales of years, emission from any particular source results in a negligible fraction of the total events in the data set – background-like events *subtract* from the TS via their contribution to the observed background rate. By contrast, a transient search is performed when a temporal source model allows us to reduce background by focusing on a smaller region in time. Here, signal events may comprise a non-negligible fraction of

the observed data during that time, so the background is parameterized separately from off-time data. The result is that all events – even those entirely consistent with background – can only *add* to the test statistic (though many contributions are practically zero).

We use the transient TS to determine how signal-like our results are by comparing the TS to a distribution of values generated by random background alone. In this analysis, we calculate the TS over a range of neutrino emission timescales ΔT, counting only neutrino candidates which arrive within $-\Delta T/2$ and $+\Delta T/2$ of any FRB, for ΔT expanding from 0.01 seconds to 1.94 days by factors of 2.

5.2   Sensitivity and Discovery Potential

In signal injection, a data set of simulation events (from NuGen, for example) is used to add on-source events to each realization – or *trial* – of simulated background. At a given time-integrated flux μ, events are injected probabilistically according to μ and the energy spectrum of injection so that their true neutrino directions point to the center of the source localization. A binary search finds the value of μ for which some fraction of signal injection trials – called the *confidence level* (C.L.) – exceeds a specified TS threshold.

For example, consider the background-only test statistic distribution (TSD) in Figure 5-1 (top-left). At $\Delta T = 0.01$ s, a TS value of roughly 13 would have 5σ significance[1]. Thus, the 5σ discovery potential (C.L. = 90%) is the value of μ for which 90% of signal injection trials have TS > 13 (see resulting distribution in top-right). When the threshold is the median of the background TSD, we call μ the *sensitivity* of the analysis. This is equivalent to the median upper limit in a pseudo-experiment ensemble if signal is not present.

---

[1]Notice that $\gg$ 99% of TS values are equal to zero. These are negative TS values, meaning they are more background-like than signal-like, which are set to zero for convenience. If negative values were retained, we could define hidden thresholds like 3σ and 4σ at each time window, but the size of TSD files would be prohibitively large to store each value. Instead, we store a single integer indicating the number of negative TS values in the ensemble.
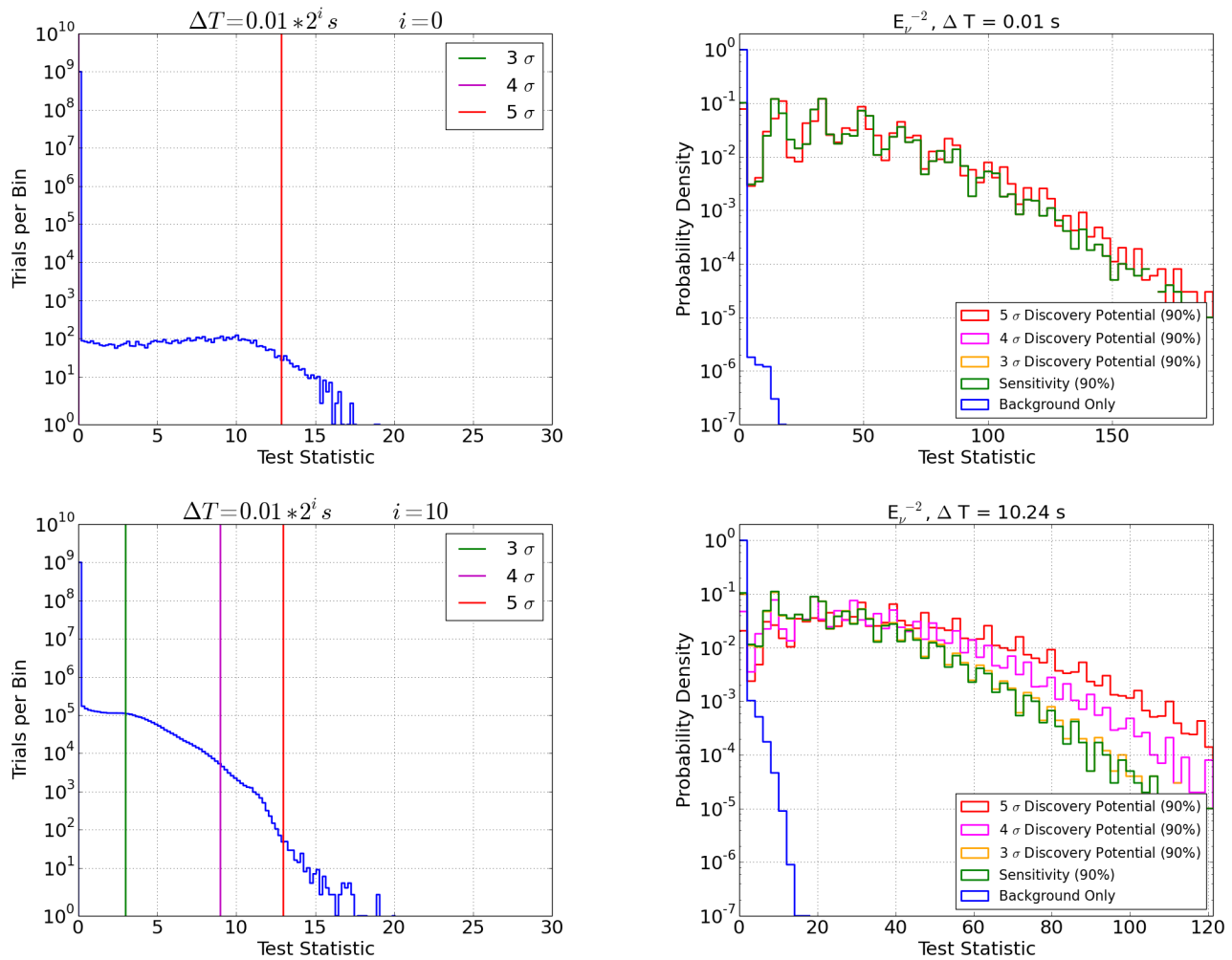
Figure 5-1: Top left: The test statistic distribution for 10^9 background-only simulation trials in the southern-sky stacking test at $\Delta T = 0.01$ s. Most trials have no events on the sky, and among those that do only a small fraction have an event near one of the nine FRBs. As a result, most TS values are zero. **Top right:** The test statistic distribution after signal injection to meet sensitivity (green) or discovery potential (red, magenta, gold). Peaks represent integer outcomes of injected events at the injected flux. E.g., when three signal events are injected, the resulting TS value is about 50 (location of third non-zero peak). **Bottom left:** The same is shown for a larger time window – $\Delta T = 10.24$ s – therefore the background is more visible. All discovery potential thresholds are all non-zero. **Bottom right:** The signal injected distributions are compared to the background distribution for this larger time window.

5.2.1   Convention of confidence levels

Within the IceCube collaboration, some groups use C.L. = 90% only for sensitivity and C.L. = 50% for discovery potentials, while others consistently use C.L. = 90% for both. There is no "correct" choice of confidence level, but for certain analyses one convention may be more appropriate than the other. Since one forgoes the ability to compare sensitivity with discovery potential when mixing confidence levels, the argument for C.L. = 50% was initially that 90% at high significance is too high a threshold to set for discovery. By requiring only 50% of signal-injected trials above threshold, the reported μ is lower, i.e. more easily attainable[2]. Now that C.L. = 50% is often used for steady-source searches, it is reasonable to adopt the convention so that the discovery potentials of analyses can be directly compared to each other.

In favor of using C.L. = 90% across the board, comparisons of sensitivity and discovery potential may be made directly within an analysis and always agree with intuition: for two values of μ, the one meeting a higher significance threshold is equal to or larger than the other. In transient analyses especially, there are regimes where the TS value of the background median is equal to those of higher thresholds like 3σ. In this case, if C.L. = 90% is used for sensitivity and discovery potential, the values of μ reported are equal (Figure 5-2, right); but when discovery potential uses C.L. = 50% (Figure 5-3), it reports a smaller μ than for sensitivity[3]. Naively, this could imply to the reader that the analysis requires less incident neutrino flux to claim discovery than to meet analysis sensitivity.

5.2.2   Sensitivity improvement at $\Delta T > 10^3$ s

In each test, there is a region where the sensitivity briefly decreases as ΔT increases. Between 10^2 and 10^5 seconds, each test transitions from a low-background regime ($TS = 0$ for $> 50\%$ back-

---

[2]This <u>does not</u> reflect a physical improvement in analysis power. A lower confidence level is only a way of making a similar statement using smaller values.

[3]We can calculate by hand the difference between low-background sensitivity and discovery potential. In the counting-experiment regime, the former requires μ such that 90% of trials inject one event: a Poisson $\lambda = 2.3$. The latter needs only one event in 50% of trials: $\lambda = 0.68$. Given that μ is proportional to λ, we expect a factor of 3.4 between sensitivity and discovery potential. Indeed, this is seen at $\Delta T = 0.01$ s in Figure 5-2.
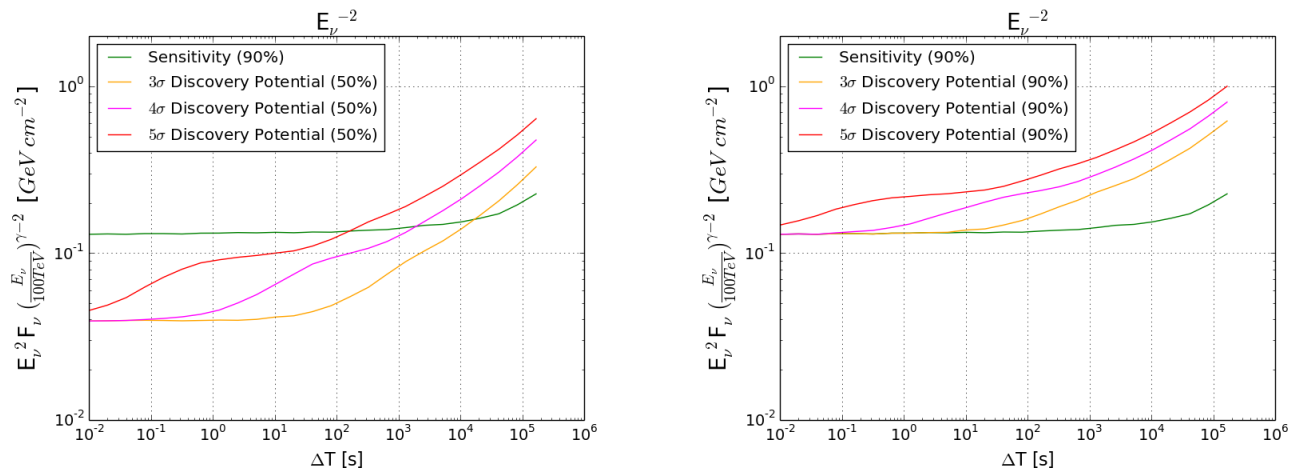
Figure 5-2: Two conventions depict the sensitivity and discovery potentials of an analysis. **Left:** In the steady-source standard, discovery potentials are reported with C.L. = 50%. The plateau features in discovery potential curves – see $\Delta T = 10^0$ s in the 5σ discovery potential – are the consequence of a changing population of background TS values exceeding 5σ. As ΔT expands, these TS values are characterized by background trials with a single event of spatial coincidence, then a single event of increasing quality of coincidence (this forms the plateau), then eventually trials with *two* events of significant spatial coincidence, and so forth. This is seen clearly in a GIF (Graphics Interchange Format) of TS distributions evolving as ΔT expands: https://wiki.icecube.wisc.edu/index.php/File:TSDexpansion.gif. **Right:** A consistent approach used more often in transient searches, C.L. = 90% is used for both sensitivity and discovery potential so that values agree with intuition about meeting certain significance thresholds.
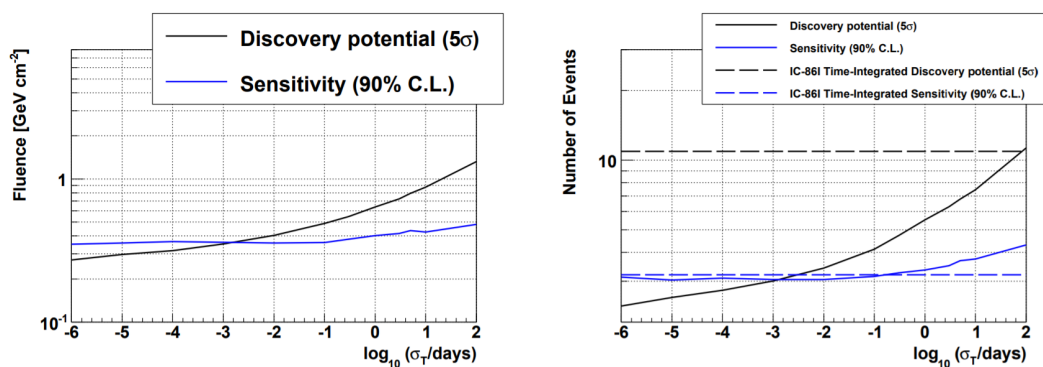
Figure 5-3: An example of a figure with mixed confidence levels in an IceCube analysis [88]. In a search for time-dependent neutrino sources with IceCube, the 5σ discovery potential – which is defined with C.L. = 50% – is lower for some emission timescales than the sensitivity (C.L. = 90%).
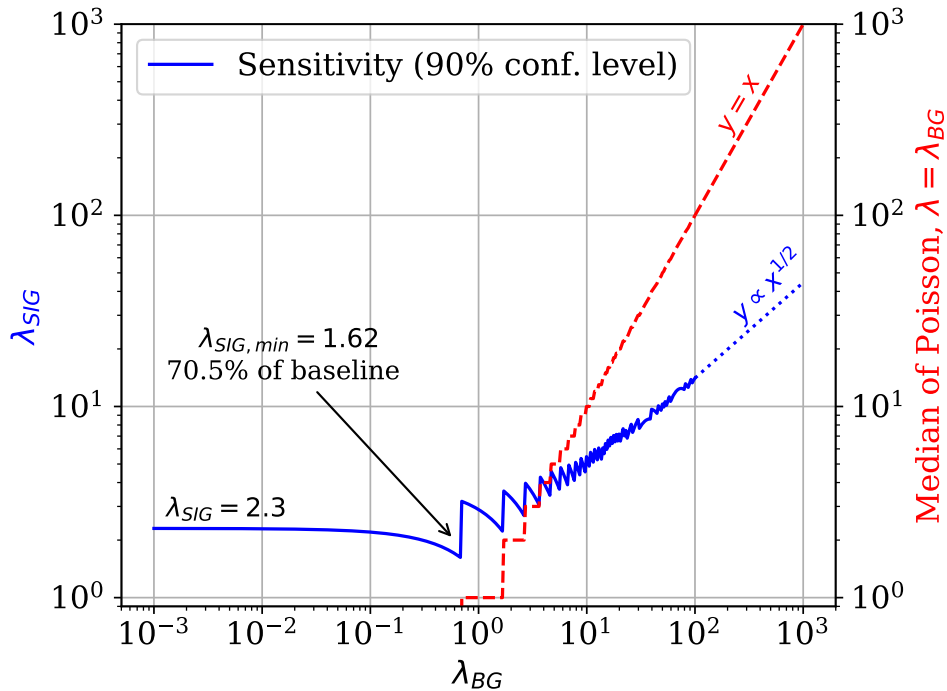
Figure 5-4: I have calculated the sensitivity (λ_{SIG}, blue) for a simple counting experiment as the background rate λ_{BG} increases; these λ's are the means of signal and background Poisson distributions. For $\lambda_{BG} \ll 1$, this is a decent approximation of the sensitivity in a search with well reconstructed tracks at small ΔT. The median counts (or test statistic) is zero, so sensitivity is flat, and the signal which produces 2.3 events on average will pass the background median 90% of the time. At larger λ_{BG}, the background median (red) begins to increase, so the required signal increases as well. In the transition between these regimes – when λ_{BG} increases but the median is constant – the level of λ_{SIG} necessary for sensitivity decreases such that $\lambda_{BG} + \lambda_{SIG}$ is constant. This causes a decrease in sensitivity to as low as 70% of the baseline flux in the transition region, after which the effects of many continuous track event PDFs make the counting experiment assumption less valid.

ground trials) to a background-saturated regime[4] (ideally, $TS = 0$ for exactly 50% of background trials). Since negative TS values are automatically set to zero, the median TS across this transition is constantly zero; however, the fraction of trials which require signal injection to exceed $TS > 0$ is shrinking (from ∼90% at $\Delta T = 0.01$ s to ∼40% at $\Delta T = 10^5$ s). The result is a non-physical improvement in the analysis sensitivity during the transition (Figure 5-4).

---

[4]I use "background saturation" to refer to the region in ΔT where in every background trial, at least one spatially coincident event (i.e., separation on the order of angular uncertainty) is expected. In the stacking searches of this analysis, this region is roughly $\Delta T > 10^5$ s.

Theoretically, the factor of $1/\langle n_b \rangle$ in each event's TS contribution down-weights injected signal at larger ΔT to counter the effect of a shifting background distribution. However, since each hemisphere combines event samples with large year-to-year differences in background rate, the contributions from each source to the background TSD evolve independently throughout the expansion of ΔT. Take the southern max-burst case: at $\Delta T = 0.01$ s, each of nine sources contribute equally to 90% of signal injection trials passing $TS = 0$. At $\Delta T = 10^4$ s, the median to pass is still $TS = 0$, but sources in IC86-2 and IC86-3 are closer to background saturation, therefore their contributions to the TSD are biased to exceed the TSD median more often from background alone. The consequence is that μ will have a larger impact on TS for the other sources, to which the analysis is more sensitive as a consequence of lower year-respective background rates. This pulls μ to lower values until the majority of sources enter the analysis' background-saturate regime.

If resources allow, this sensitivity dip could be avoided by reforming the storage of TS values. First, by setting the TS for each trial with zero events to a designated "No Events" bin in the TSD (equivalent to $TS = -\infty$); and second, by keeping *all* TS values for trials with at least one event on the sky. By retaining negative TS values, significance thresholds in the TSD will be strictly increasing as ΔT expands, resolving this behavior in sensitivity. However, as discussed, this could produce prohibitively large TSD files.

5.3   Seasonal Variation

The mean free path of pions produced in cosmic-ray interactions is anti-correlated with the atmospheric density and thus positively correlated with temperature. At higher atmospheric temperatures, a pion is more likely to decay producing a muon (and muon-neutrino), which may penetrate to and trigger the IceCube detector [89]. In IceCube event samples, the background consists of atmospheric muons and neutrinos, so a periodic fluctuation in the event rate can be seen (Figure 5-5).

In transient analyses, the number of observed events is compared to a prediction of the background
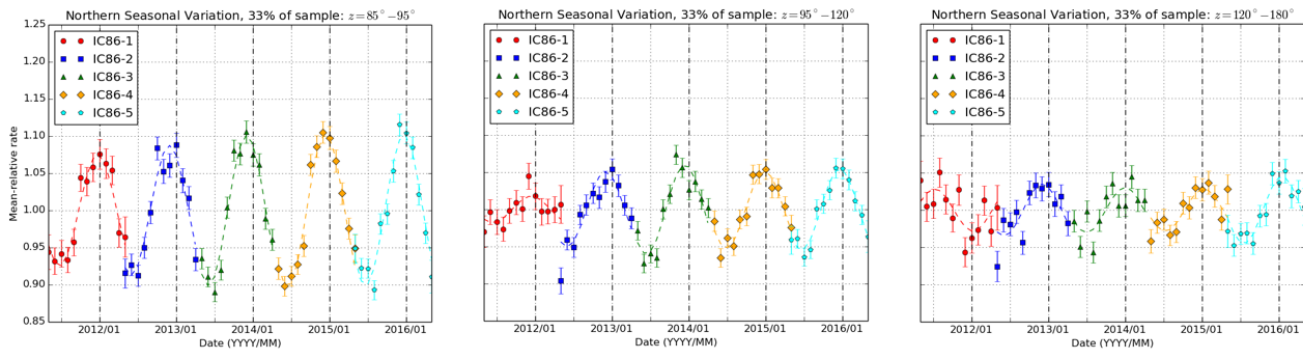
Figure 5-5: From left to right: three equal-statistics subsets of the northern-hemisphere event sample are sorted by increasing declination. The amplitude of seasonal variation is proportional to the impurity due to misreconstructed atmospheric muons. Notice that for IC86-1, the event selection happened to pick up the temperature variation in the northern hemisphere – up-going muon-neutrinos from this same process trigger the detector with a seasonal phase shift of 180°.

event rate during the time of interest (see Appendix B and the $\langle n_b \rangle$ in the likelihood). If this prediction were drawn from a yearly average, seasonal variation could result in a large systematic error. In this analysis, a sine wave with fixed period ($T = 365.25$ days) was fit to data binned by month. This sine fit is sufficient for estimating $\langle n_b \rangle$ in these background regimes; at the largest time-window, the number of events on the sky per burst is ~ 600, so the residual between the sine fit and truth at any time only has to be lower than a statistical error on $\langle n_b \rangle$ of $\sim 4\%$. In the next analysis (Chapter 6) the residual dominates random statistical error, so I argue for implementation of a more sophisticated background fit.

5.4 Discussion of Results

Figures 5-6 and 5-7 show on-time events whose coincidence with an FRB was the most significant in their hemispheres. Despite some spatial correlation, the results are consistent with the null hypothesis: $p = 0.25$ and $p = 0.84$ after trials correction for 25 time windows searched. This section addresses the perhaps surprising insignificance of the results in the southern sky, where two events overlap well with FRB 140514, one with a separation of only 0.20°.

The first and most important factor is time; had this most significant event ($\Delta\Psi = 0.20°$) been detected within < 1 minute of the FRB, its significance alone would be $> 3\sigma$ post-trials. Instead,
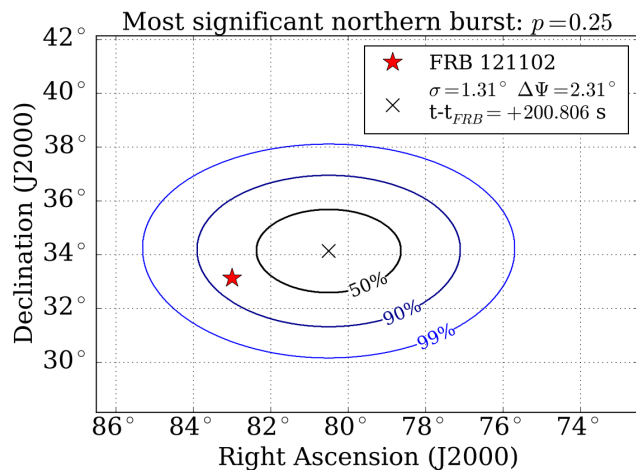
Figure 5-6: Most significant burst in northern tests [76].
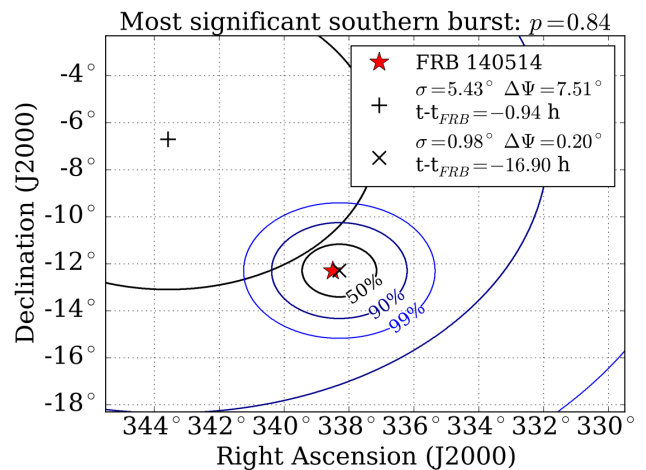
Figure 5-7: Most significant burst in southern tests [76].

the event wasn't detected until our largest search window, where the background event density at FRB 140514 is roughly one event per 300 deg^2. Adding a trials factor for the nine FRBs considered in the southern hemisphere test, one event within $\sim 3°$ of an FRB is entirely consistent with the null hypothesis.

The next important factor is the event's estimated angular reconstruction error, $\sigma = 0.98°$. Although the FRB lies well within the central 50%-containment region of the event's point spread function, an angular error roughly twice the event sample average reduces the signal likelihood of correlation by a factor of four. Section 5.4.1 discusses the effects of angular error and separation on significance calculations.

5.4.1   Resolution and containment

Analysis sensitivity is strongly dependent on the distribution of angular uncertainties (σ's) in an event sample. In background trials, an event with a large σ is more likely to have a probability distribution function (PDF) which overlaps with a source at non-negligible PDF height (e.g., $> 1/4\pi$, the all-sky average of the background PDF). This can reduce the temporal space in which an analysis is considered low-background. Furthermore, during signal injection, neutrino events from simulation are injected on-source until a significance threshold is exceeded. Here, an

simulated event's σ affects both its $\Delta\Psi$ – because its fit-to-truth separation is related to σ – and the PDF's shape, making a large impact on σ's contribution to the test statistic.

Figure 5-8 shows cross-sections of radially symmetric 2-D Gaussians with varying σ. The signal likelihood assigned to an event is proportional to the height of its PDF at the source location. For example, at $r = 0°$ an event with $\sigma = 5°$ has a signal likelihood just 4% that of one with $\sigma = 1°$. Moreover, even though a separation of 2.5° would put the source outside of the 90% containment region of an event with $\sigma = 1°$, that event would be assigned the same signal likelihood as a perfectly coincident event ($r = 0°$) with $\sigma = 5°$. For this reason, the containment region of an event should not be conflated with the spatial part of the event's signal likelihood.

Figure 5-9 shows this example carried out using `grbllh`[5]. Both events were separately injected with angular separations and σ's of ($\Delta\Psi = 2.5°, \sigma = 1°$) and ($\Delta\Psi = 0°, \sigma = 5°$). The two test statistics returned were equal to within 5%. Appendix B.2 explains how event uncertainty is implemented in the likelihood and software.

5.5   Zenith Fine Structure in Data

In the southern data sets, the event selection prefers to keep events with directions that imply a larger ice overburden and thus are less likely to be atmospheric muons. In `grbllh`, the resulting zenith distribution is modeled using 20 bins in $cos(\theta)$ and a spline fit (Figure 5-10). During checks after the analysis was unblinded, finer binning in zenith revealed fine structure; Figures 5-10 and 5-11 show that the zenith PDF in data oscillates about the original spline fit with a significant relative amplitude and a period of $\sim 3°$. This effect is neither seen in northern-sky data nor southern-sky simulation, and its cause is currently under investigation.

Until the cause of this oscillation is resolved, it is sufficient to recognize and parameterize these

---

[5]`grbllh`, which stands for "gamma-ray burst log-likelihood", is a software package used in IceCube for analyses of transient sources. As the name suggests, its functionality was originally designed with searches for neutrino emission from gamma-ray bursts in mind; but it is a useful and computationally fast tool for many transient analyses because it performs the most time-intensive likelihood calculations in the C++ programming language rather than in Python.
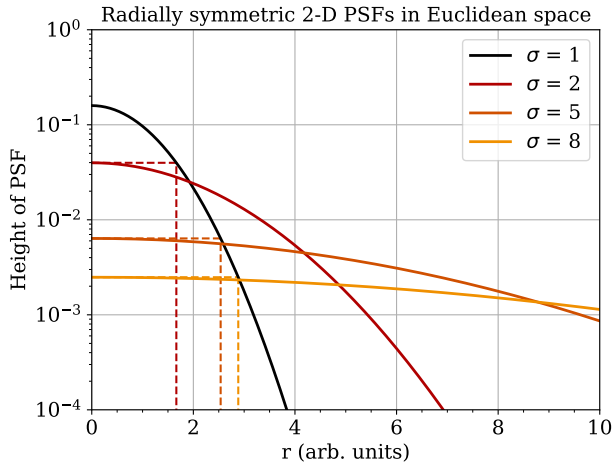
Figure 5-8: Cross-sections of several radially symmetric 2-D Gaussians in Euclidean space are shown with varying standard deviation (σ). Dotted lines indicate the separation at which a PDF with $\sigma = 1°$ would have the same signal likelihood as an on-source event with the corresponding σ.
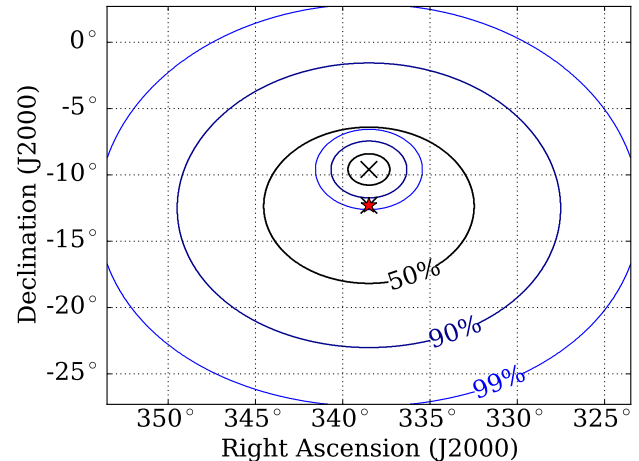
Figure 5-9: Two events were injected separately to demonstrate the dependence of the signal likelihood on σ. The first is injected with a separation $r = 2.5°$ from the source (red star) with $\sigma = 1°$. The second is injected on-source ($r = 0°$) with $\sigma = 5°$. Both return approximately the same test statistic in `grbllh`.
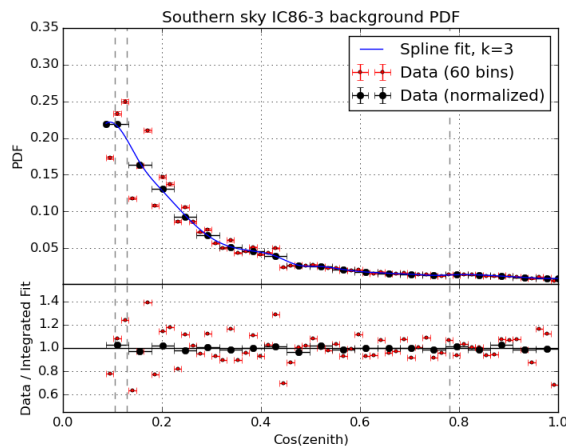
Figure 5-10: By default in `grbllh`, data are binned into 20 bins (black) in $cos(\theta)$ and fit with a spline of $k = 3$ (k determines the order of the piecewise polynomial). Finer binning reveals a fine structure in the data that is not modeled by the background PDF.
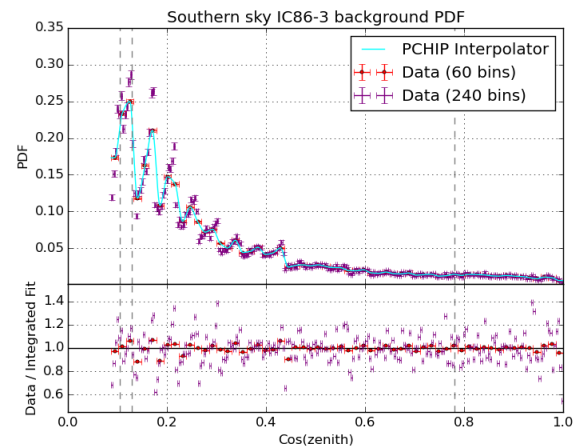
Figure 5-11: A PCHIP interpolation of data using 60 bins (red) highlights the local extrema in data zenith with a periodicity of $\sim 3°$. These features are not seen in northern-sky data or simulation.

features to remove systematic bias. Statistics permitting, data should be binned finely enough so that the angular bin width is less than the average angular error in data. Features at $0.1°$ intervals will be smoothed out in data with angular errors on the order of $1°$. Additionally, piecewise polynomial splines do a poor job of fitting non-smooth systematic effects, so a piecewise interpolator is preferred if irregularities in background PDFs are found. The Piecewise Cubic Hermite Interpolating Polynomial (PCHIP) in Figure 5-11 passes through each data point exactly and has a continuous first derivative. The fit shown is called "monotone" because unlike the spline fit, it features no local extrema between points.

Similarly, the HESE (High-Energy Starting Events) group sees an unexpected all-sky oscillation of the Monopod and Millipede (two IceCube fit algorithms) reconstructed zenith PDF about the broader structure with an amplitude of about 10% (Figure 5-12); however, their periodicity does not align with the fine structure discussed here. Neither sample has peaks which are consistent with DOM alignment, so detector geometry is not suspected to be the cause. It is possible that the reconstruction algorithms are biased to optimizing at seeded zenith values, but this hypothesis has yet to be thoroughly tested. The absence of these features in low-level data suggests that event selection methods may also be the culprit.
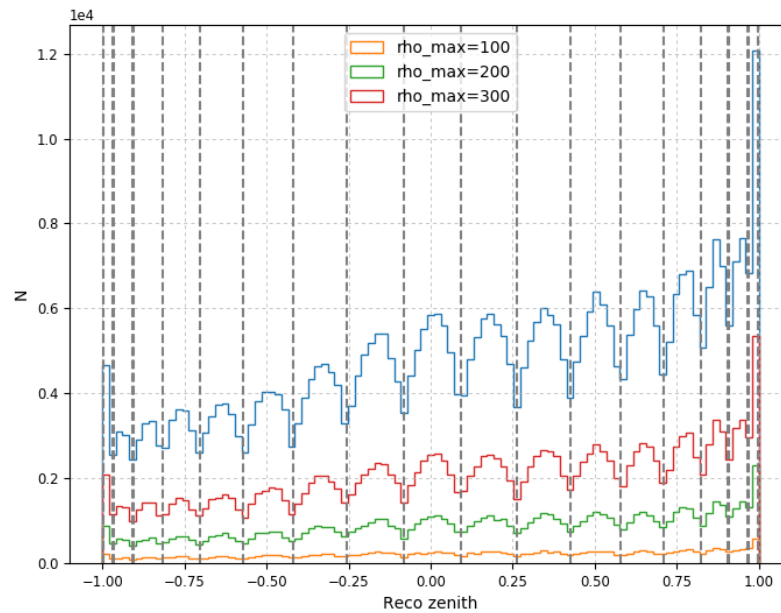
Figure 5-12: The reconstructed zenith PDF for simulated electron neutrinos passing the cuts for the high-energy starting event (HESE) sample exhibits odd behavior as well. The spikes in this figure align neither with the oscillations in the zenith data for the six-year analysis nor with obvious alignment of DOMs in the detector geometry. Plot taken from slides by the HESE Taskforce, in the IceCube Diffuse Call on 25 July 2018.

Chapter 6

FRB Analysis with Loose Cuts

Chapter 5 demonstrates that for ΔT less than one hour, analysis sensitivity in time-integrated flux is independent of ΔT as a result of a mHz-rate (all-sky) event sample. Alternatively, a more inclusive event sample would have increased acceptance to signal neutrinos and background, improving sensitivity at small ΔT in exchange for an earlier upturn into a background-dominated regime. This analysis shows that sensitivity to very short transients can be optimized with a loose event selection, improving effective area (explained in Section 6.4 at the expense of high background for $\Delta T > 10^3$ s.

A paper on this analysis[1] is currently in preparation.

6.1   Event Selection

The lowest level of directional IceCube data is called "Level 1" and has an event rate of $\sim$3 kHz due almost exclusively to atmospheric muons. At the shortest time that encompasses all FRB durations – 30 ms – this would contain 100 events on the sky per burst, with angular errors on the order of 10°; one would expect each source to be spatially coincident with a background event. Thus, when stacking many sources, Level 1 is not capable of providing a low-background regime

---

[1]The paper will cover this analysis and an analysis in search of temporal correlation of FRBs with MeV neutrinos, conducted by Ali Kheirandish.

in ΔT.

At the next data level, "Level 2" (*pass 2* specifically, after updates to Level 2 processing in 2016), events with track-like qualities pass the MuonFilter[2] at a rate of 35 Hz, with a median angular error of roughly 15°. At $\Delta T < 1$ s, this event sample is unlikely to contribute a spatially coincident background event to a source. This makes Level 2 a good starting point for an analysis of FRBs: the analysis has values of ΔT for which the expected background TS is zero, and any further cuts will reduce acceptance to astrophysical neutrinos.

Starting at Level 2 MuonFilter, simple preliminary cuts are made to remove unusable events. These are poor track-like events for which one or more attributes prevents proper analysis, including:

1. Corrupted subruns[3]: $< 0.1\%$ of data discarded

2. Non-convergent MuEX[4] value (NaN): $\sim 1\%$ of data discarded

3. Non-convergent Spline-MPE fit: another $\sim 1\%$ of data discarded

Level 2 data comes with a PandelMPE track fit (refer to Section 2.2), so I performed Spline-MPE during processing for improved directional reconstruction (Figure 6-1). As an initial plan to calculate event-wise angular uncertainty, I then performed a Paraboloid fit on the likelihood space from Spline-MPE. Due to computational limitations, this analysis instead estimates errors on Spline-MPE using random forest regression, which is explained in Section 6.2.3.

---

[2]MuonFilter is one of many event streams that are allocated a fraction of IceCube's satellite bandwidth (~ 75 GB/day) for minutes-delayed availability to IceCube researchers around the world. Cuts to reduce data size select quality track-like events to pass MuonFilter. For example, events with a line-fit zenith angle $\theta < 70°$ require eight DOMs, and for $\theta > 70°$, 10 DOMs are required. Down-going tracks must also pass a cut on the deposited charge in the event, and up-going tracks are cut on the likelihood returned by the track fitter (rlogl, specifically, which I discuss later in this chapter); both cuts were found to remove atmospheric muons more efficiently than neutrino events.

[3]IceCube data is stored in "runs", which typically last eight hours. Each run is transmitted via satellite in smaller pieces, called "subruns", and individual subrun files can sometimes be unreadable/corrupt in data storage in the North.

[4]"MuEX" is the name of an estimator of the initial muon energy for track events in IceCube. It is a more accurate estimator than the quick "MuE" estimate performed immediately at the South Pole on all events.
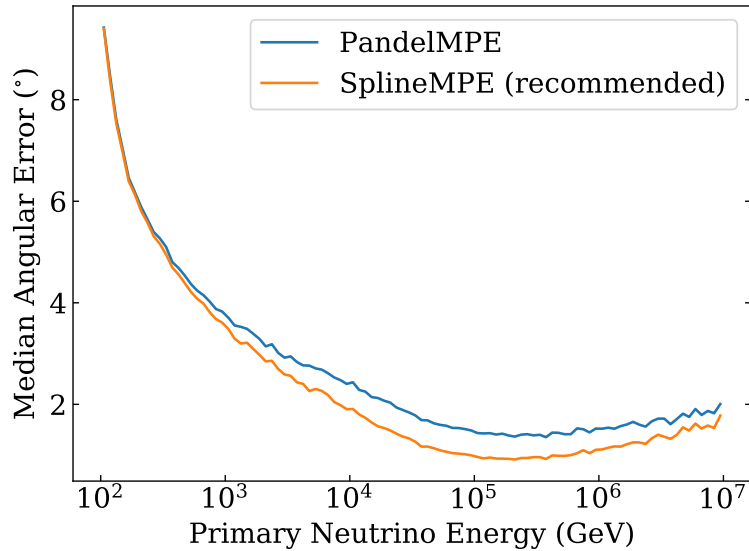
Figure 6-1: For Level2-pass2 simulation events, the median angular separation between fit and primary neutrino direction are compared for the typical PandelMPE fit and Spline-MPE fit. Note that the rate of neutrinos at energies above 10^6 GeV, where the fit results worsen slightly, is negligible for IceCube.

Figure 6-2 shows the PDFs of the data in reconstructed zenith angle (left) and azimuth (right). The zenith angle distribution peaks at the zero, where background from atmospheric muons is greatest. A filter cut from Level 1 to Level 2 removes many of these events at $\cos(\theta) > 0.3$, whereafter the cut is lessened. This causes the non-physical second peak in data at $\theta = 70°$. The seasonal variation is indicated by plotting the lower and upper bounds from the winter-minimum and summer-maximum event rates respectively.

The azimuth distribution has two key features; the first is six distinct spikes equally spaced in azimuth. The locations of these local maxima align exactly with the orientation of IceCube's hexagonal grid. Each inner string has six nearest neighbors at azimuth values corresponding to the largest six spikes. Low-energy events are likely to hit fewer DOMs on fewer strings, increasing the probability of the directional fit to converge exactly on the grid orientation. A second set of spikes can even be seen between the dominant ones, owing to the orientation of second-nearest neighbor strings in the grid.
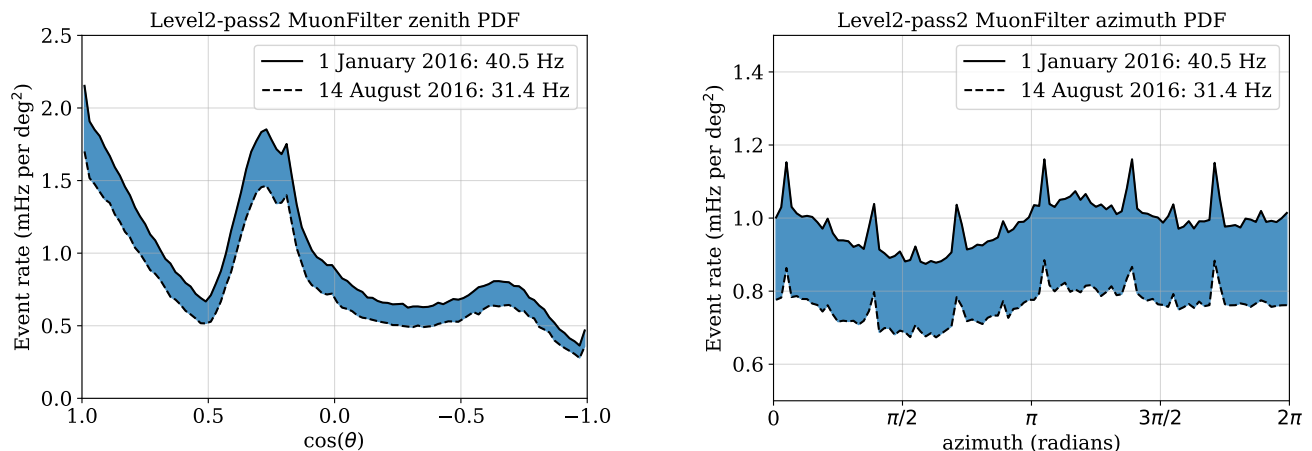
Figure 6-2: Left: Reconstructed zenith angle PDF for this event selection. Features in the southern sky are caused by zenith-angle-dependence in the MuonFilter cuts (referenced in Footnote 2). **Right**: Reconstructed azimuth PDF for this event selection. The spikes at intervals of $\pi/3$ are due to the hexagonal detector grid, but the cause of the large-scale asymmetry is presently unknown (see Appendix C).

The second feature is a large-scale shape, the cause of which is still under investigation (see Appendix C for further discussion). Regardless, all features are parameterized in the analysis background PDFs and result in no systematic bias in the results.

6.2 Angular Uncertainty

The use of Spline-MPE is motivated by its demonstrated accuracy as an average reconstruction error for an ensemble of events. However, the fit alone does not provide estimated angular errors on an event-by-event basis. For individual estimates of the separation between reconstruction and primary neutrino directions, IceCube's *Paraboloid* module is implemented.

6.2.1 Paraboloid and pull correction

Paraboloid explores the likelihood space of a muon track fit around the minimum direction returned from the chosen fitter. The expectation is that the PDF in likelihood space should have the shape of a 2-dimensional Gaussian, thus in log-likelihood space it becomes a 2-dimensional parabola – a paraboloid. The relevant output from Paraboloid is the semimajor and semiminor
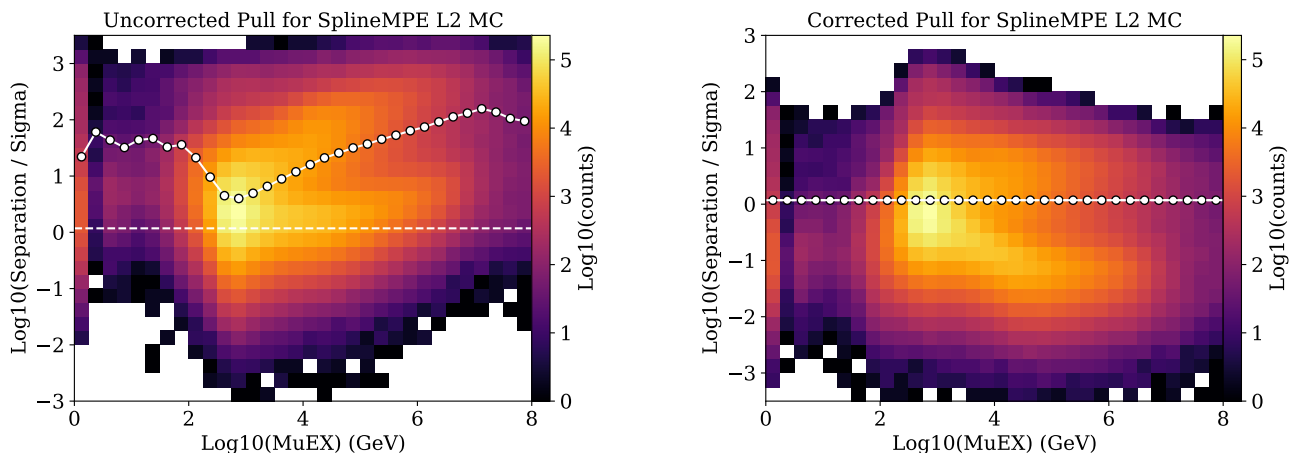
Figure 6-3: Left: The pull (y axis) is calculated with respect to MuEX for the Level2-pass2 simulation sample. **Right**: Pull correction is demonstrated for the same events. Each event's $\sigma_{parab.}$ is multiplied by a correcting factor determined by its MuEX bin so that each bin's average pull is 1.177 (the correct expectation for separation divided by σ).

axes of the event's 1σ error ellipse, which are converted to a Gaussian $\sigma_{Parab.}$ assuming radial symmetry for analysis simplification ($\sigma_{Parab.} = \sqrt{(\sigma_{minor}^2 + \sigma_{major}^2)/2}$). Since this $\sigma_{Parab.}$ is a result only from simulation, it is susceptible to unknown or unaccounted-for systematic errors in our experiment (e.g., errors in our estimation DOM photon detection efficiency and ice crystal alignment anisotropy). To account for these unknowns, we introduce the term *pull*: the ratio of an event's true angular separation over $\sigma_{parab.} \cdot \sqrt{\ln 4}$[5]. The pull is calculated for subsets of simulation sorted by one or more features; for example, the general recommendation is to bin simulation events by MuEX and return a MuEX-dependent pull correction, which is applied to $\sigma_{parab.}$ for data events (Figure 6-3). For example, events with larger MuEX tend to have overly optimistic (too small) $\sigma_{parab.}$ values, so real data with larger MuEX have their $\sigma_{parab.}$ scaled up by the factor by which $\sigma_{parab.}$ and $\Delta\Psi$ disagree on average, at the given MuEX range.

Once the pull values have been calculated, all events in data and simulation may be pull-corrected by their feature-determined pull estimates. In simulation, these final σ values may be compared

---

[5]If the angular separation of an event represents the median separation drawn from an underlying PDF, its Gaussian analog is $r_{50\%}$, the radius within which 50% of the PDF's area is contained. For a 2-D Gaussian in Euclidean space, the radius that contains a central fraction p of the PDF is $r_p = \sigma\sqrt{2\ln(\frac{1}{1-p})}$, thus $r_{50\%} = \sqrt{\ln 4} \approx 1.177$.
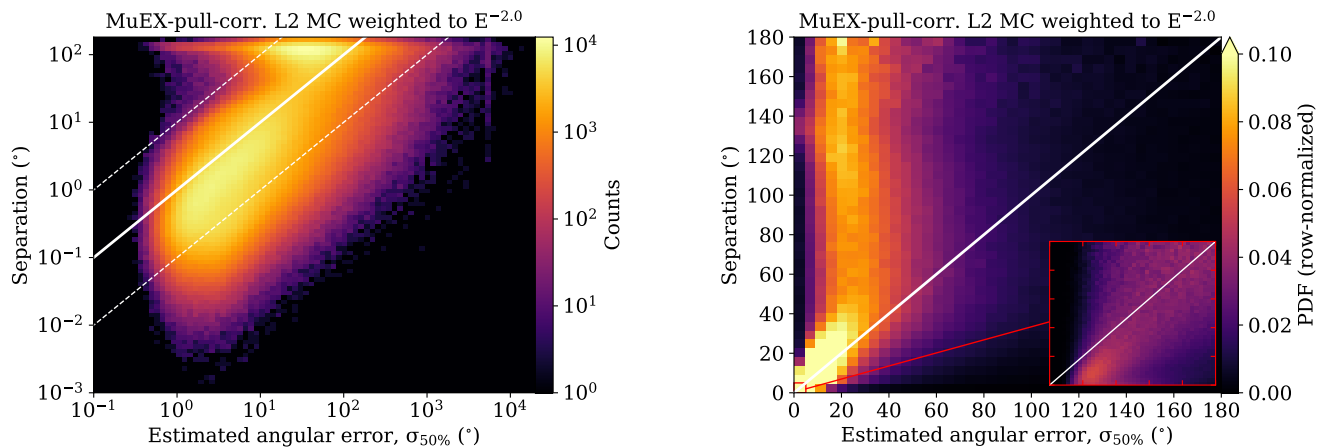
Figure 6-4: Left. The Level2-pass2 simulation has been pull-corrected with respect to MuEX (Figure 6-3); a 2-D histogram compares the pull-corrected σ from Paraboloid to the true angular separation. The white solid line denotes the axis of ideal σ-separation agreement; dotted lines form a region within a factor of ten from this line. As a result of pull correction, events with large $\sigma_{parab.}$ and sufficiently large pull may be "corrected" so that $\sigma \gg 180°$. This is an unnatural result of the pull-correction method, but since only poorly fitted events are affected, it has a negligible effect on the analysis. **Right.** The same data are plotted on a linear scale with each row representing a normalized PDF. For events with a true angular separation of more than $40°$, the assigned σ typically underestimates the fit error. The red box shows a zoomed in view from $0°$ to $5°$, so that features in the most well reconstructed events may be seen. The average pull is so large for this event selection that many accurate reconstructions (separation $< 1°$) have σ that overestimates the fit error.

to true angular separation as a measure of the Paraboloid method's quality of error estimation. In Figure 6-4 the pull-corrected σ's are compared to their respective angular separations. The broadness of the distribution around $x = y$ is evidence of Paraboloid's shortcomings when applied to Level2-pass2 data; many events appear to have been assigned σ which differ from their true separation by a factor of ten or more.

6.2.2 Multi-variable pull correction

As an attempt to salvage Paraboloid for this analysis, I first try a natural extension to the MuEX-pull-correction method: a multi-variable pull-correction method, using the event features SplineMPE zenith angle, MuEX muon energy, Spline-MPE log-likelihood (*logl*), and the reduced *logl* (*rlogl*), which is *logl* divided by the number of degrees of freedom in the fit: the number of
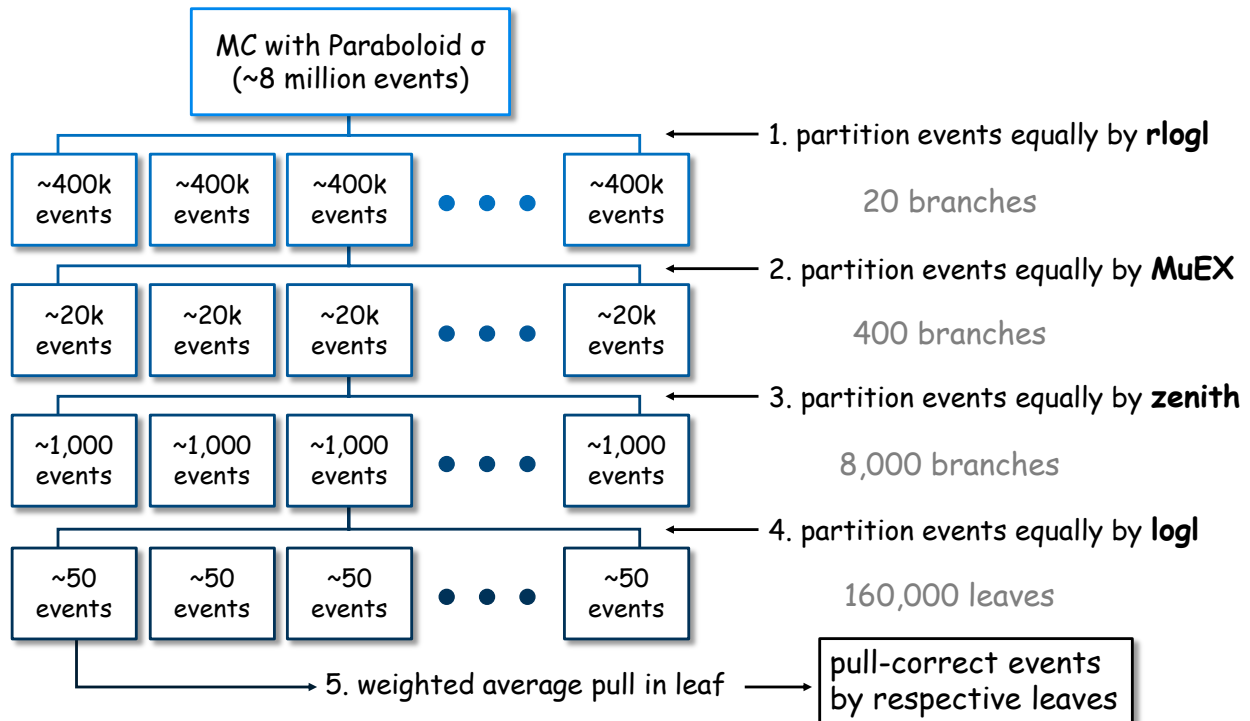
Figure 6-5: Paraboloid pull-correction tree. Simulation events (MC) are divided equally at each level into 20 bins according to one of four features. After the fourth level, the weighted pull is averaged in each leaf; data and test-case MC events pass through the tree and are pull-corrected by their respective leaves. The order shown was found to be optimal among the 24 possible feature orderings.

hit DOMs less five (x, y, z, θ, and ϕ of the track). These are the four features available in data on which fit quality is dependent. Instead of partitioning Monte Carlo events (MC) by only MuEX, I build a tree that partitions MC four consecutive times, at each level dividing MC equally by one of the four features (see Figure 6-5)). A simple cross-validation scheme tested feature order and number of branches at each level: the method that minimized the average of standard deviations of pull values in each respective leaf was found to be 20 branches per level in the partition order rlogl, MuEX, zenith angle, and finally logl. The results shown in Figure 6-6 are visibly better – closer to $\sigma_{50\%} = \Delta\Psi$ – than those from single-variable correction (Figure 6-4).
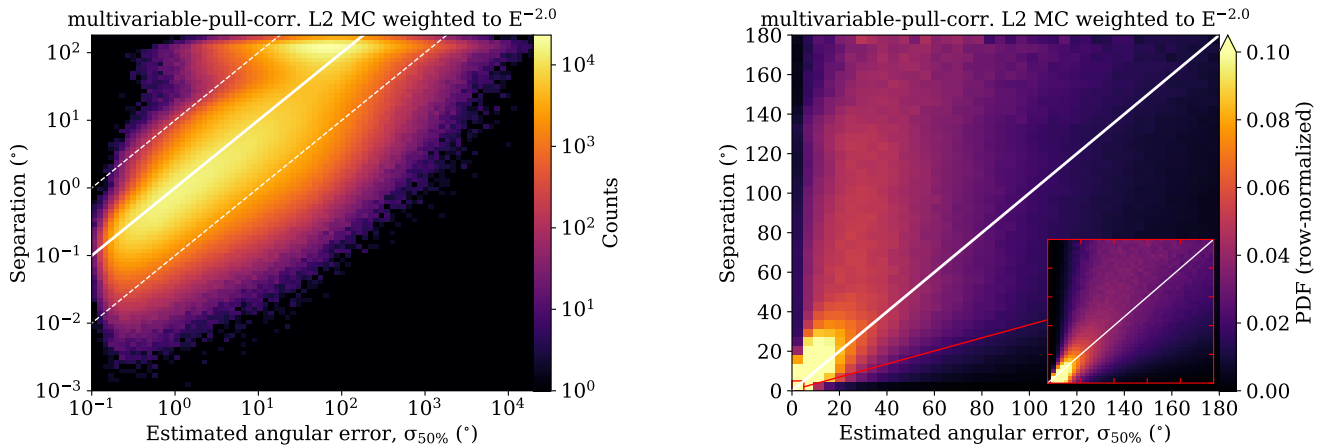
Figure 6-6: The method of multi-variable pull correction is evaluated following the format of Figure 6-4. The results are visibly improved, noting the new symmetry of the heatmap about $x = y$.

6.2.3   Implementing random forest regression

High-level data samples typically have on the order of a million events per year. If Paraboloid spends only a few seconds examining each event, the computation can be organized simply into 1,000 one-hour jobs. Level-2 MuonFilter, however, has millions of events *per day*. Faced with imperfect Paraboloid results and the inconvenience of computational and memory issues, I explored the effectiveness of a random forest regressor built to estimate angular error.

Figure 6-5 depicts a decision tree that I refer to as an untrained tree, because the branching is predetermined, and no effort is made to change branching ratios to optimize results. Here I use Scikit-Learn's machine learning modules to implement a forest of trees that search different branching values and features[6]. Instead of each leaf corresponding to a pull value (Section 6.2.2), the leaves of each tree in the random forest represent angular separation estimates.

6.2.4   Weight, target, and hyperparameters

The random forest module is built to minimize the mean squared error of true separations to predicted separations for a testing set of simulation events. The mean squared error can also be

---

[6]http://scikit-learn.org/stable/modules/generated/sklearn.ensemble.RandomForestRegressor.html
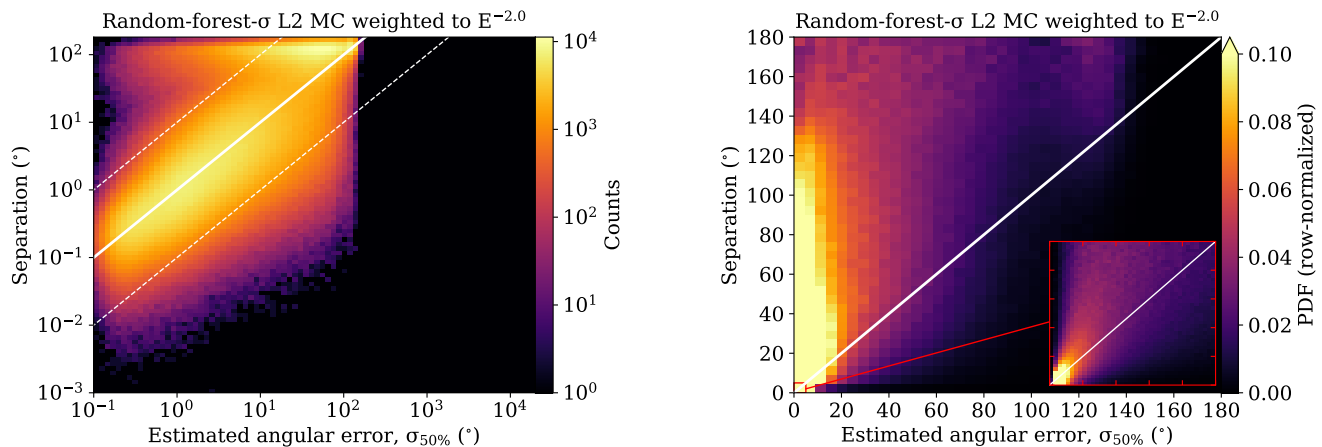
Figure 6-7: The results from the random forest method of angular uncertainty estimation are shown. Performance is similar to Figure 6-6 with drastically reduced computational resources. Another benefit is that the random forest algorithm does not assign $\sigma > 180°$.

weighted to prioritize predictive quality for a subset of data. In my random forest, the target variable is not angular separation but the logarithm of separation. The effect of the predicted separation residual on the signal likelihood space for an event is proportional to the ratio of predicted separation to true separation; when choosing branching decisions with this target, the forest minimizes the residual as a per-event error ratio, as opposed to a value in units of degrees.

$$residual = weight \ (\hat{\sigma} - \Delta\Psi)^2 \rightarrow weight \ (\ln \frac{\hat{\sigma}}{\Delta\Psi})^2 \tag{6.1}$$

The per-event weights assume an E^{-2} spectrum with an additional factor of $1/\sigma$ to optimize for precise estimation of well reconstructed events. The hyperparameters which returned the best angular error estimates, memory permitting, were found using the grid-search cross-validation module[7]: n_estimators = 40; criterion='mse'; max_depth = 42; max_features = 1; bootstrap = False. Results (Figure 6-7) are comparable to those from multi-variable pull correction. A comparison of results from methods discussed here is shown in Figure 6-8.

---

[7]http://scikit-learn.org/stable/modules/generated/sklearn.model_selection.GridSearchCV.html
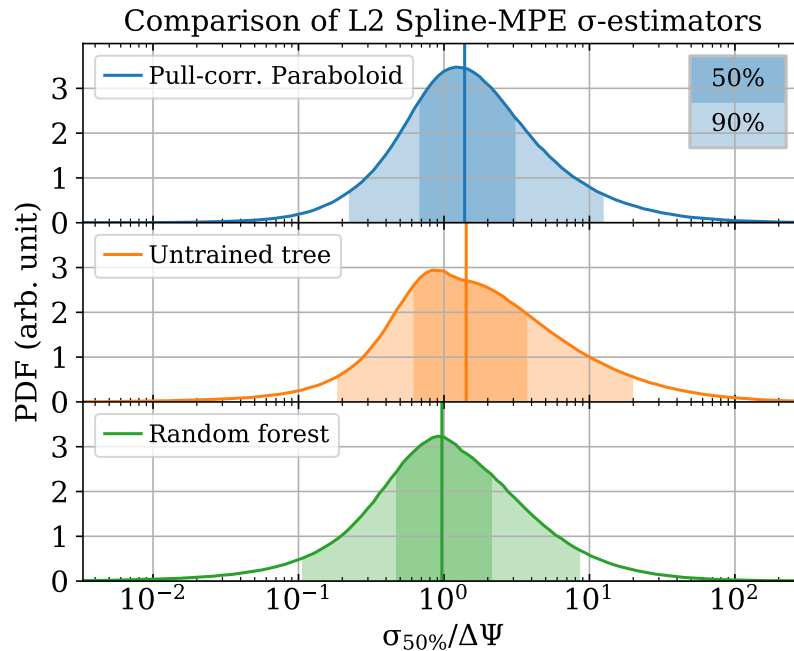
Figure 6-8: Top: For a test set (i.e., not used for training) of simulation events, the distribution of ratios $\sigma_{50\%}/\Delta\Psi$ results from angular uncertainty estimation using Paraboloid and a multi-variable pull correction. 50% of events have an estimated $\Delta\Psi$ within factors of 0.7 and 3.0 from truth; 90% within factors of 0.2 and 12. **Middle**: Using the pull-correction tree to instead estimate $\Delta\Psi$ directly, the average accuracy is worse as shown by the broader distribution. Both methods overestimate the median angular uncertainty by $\sim 40\%$. **Bottom**: A random forest performs comparatively well predicting $\Delta\Psi$ and returns a median error factor of ~ 1. This symmetry is desired to reduce bias during background trials.
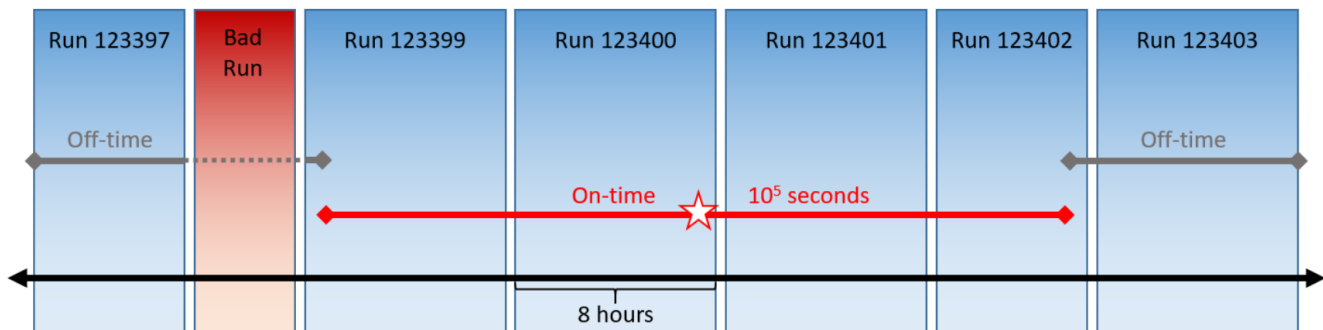
Figure 6-9: Events within $\pm 0.5 \times 10^5$ s of the center of an FRB duration are labeled as on-time and stored for unblinding. Events outside of this window until the first whole run are labeled as off-time and used for parameterization of the background.

6.3 Data Handling

6.3.1 On-time and off-time

Since this data has such a high rate, it would be impossible to store entire processed years of data as other high-level analyses do. Filtered Level-2 data[8] are stored only from times near FRB detections to form on-time and off-time data sets. Figure 6-9 demonstrates how runs are chosen: events that fall within the largest ΔT of an FRB are designated as on-time events; in the runs at the endpoints of ΔT, events outside of ΔT are designated as off-time. The nearest "Good" runs before and after these runs are also included to ensure sufficient off-time statistics.

As a measure to improve computational efficiency, the off-time is reduced randomly by a factor of 20. Each FRB has two off-time samples of roughly 1 million events, one prior to and one following the on-time sample. In each off-time sample, 5% of events are kept while the others are discarded from the final off-time sample. The nominal livetime for the sample is multiplied by the fraction of events kept (so the rounding on 5% of N is irrelevant). The final set of off-time samples for all FRBs contains 3 million events; this makes computations possible using less than 5 GB of memory and results in 100-bin directional feature histograms with 0.5% statistical error per bin.

---

[8]Data are stored in subrun `i3` files at /data/exp/IceCube/2013/filtered/level2pass2/.

6.3.2 Leap seconds

In Coordinated Universal Time (UTC), the second is defined so that the mean solar day – the average time from solar noon to solar noon the next day – in the year 1900 is exactly 24 hours (86,400 seconds) long. However, since 1900, the Earth's rotation has slowed so that the mean solar day is about 1 ms longer today. To correct for the discrepancy between solar time and UTC that accumulates over many days, an additional second is sometimes added to the final minute of either June 30 or December 31; that is, there is 1 second that begins at 23:59:60 and ends at 00:00:00 the next day.

In 2012, IceCube's master clock had a bug that mistakenly implemented the leap second on June 29 and again on the correctly scheduled June 30. As a result, every timestamp on IceCube events from 29 June 2012 until the discrepancy was resolved for IC86-2015 is 1 second behind UTC; an event with the timestamp 21 May 2014 12:00:00 actually triggered the detector in UTC at 21 May 2014 12:00:01. To account for this, all on-time events in the range of affected runs (Run 120398 through Run 126377) have 1 second added to their timestamps. This fix is being applied retroactively to other IceCube data sets as well.

In addition to this fix, FRB times are adjusted so that ΔT is centered on the time that the detected radio emission would have arrived at IceCube if the Earth were transparent to radio frequencies. For any pair of observatories on Earth, this adjustment – called a topocentric correction – is no more than 42 ms. Appendix A explains how this adjustment is performed.

6.4 Effective Area

The motivation for analysis of a looser event selection is that fewer hypothetical signal events are rejected for their background-like characteristics. To evaluate the improved efficiency of this data for detecting a neutrino flux, we compare the effective area to that of the data from the six-year FRB analysis. The effective area is a property of an event selection that quantifies the probability
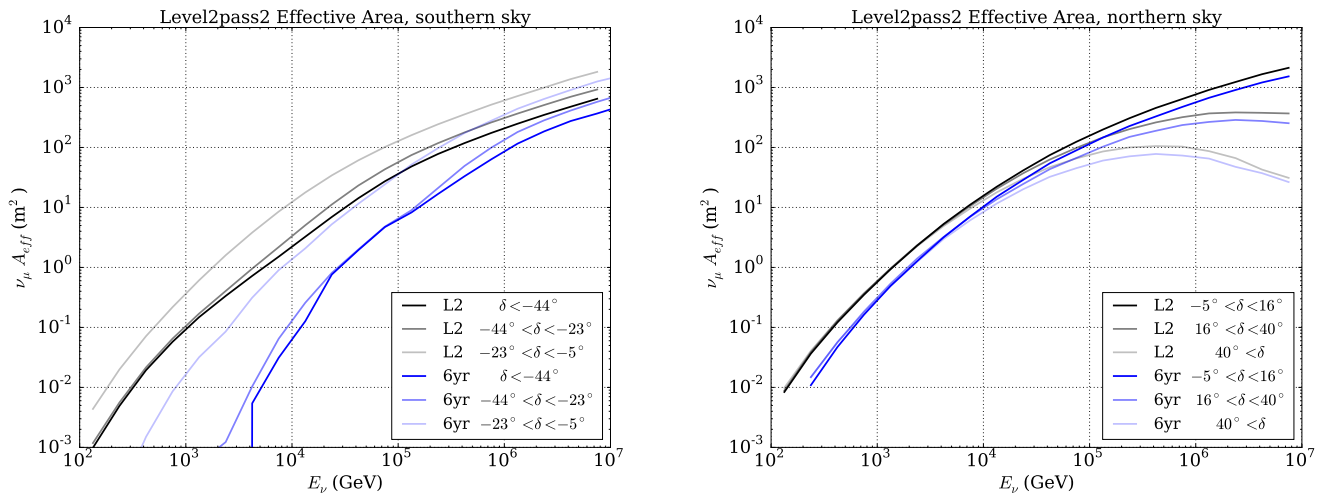
Figure 6-10: Left: The effective area of Level-2 MuonFilter to muon neutrinos from the southern sky is split into three declination ranges of equal solid angle. In blue I compare the effective area of the event selection used in the six-year FRB analysis. **Right**: Here, the same comparison is made for the effective area in the northern sky.

of neutrinos of a given energy to interact in the detector, trigger, and remain in data after the event selection process. Since neutrinos rarely interact with matter, there is a large discrepancy between the detector cross section normal to an incoming flux and the cross section of a hypothetical perfect detector that detects 100% of that flux.

For example, if some flux of neutrinos were directed at a 1 km^2 area, but only one in one million neutrinos triggers the detector, the "effective area" of the detector to that flux is 1 m^2. We often plot the effective area versus neutrino energy, because the neutrino-nucleon cross section increases with energy. It is also common to show the effective area averaged in some range of directions, because detector properties, event selection, and absorption of neutrinos by the Earth all affect the fraction of neutrinos that trigger the detector from a given direction.

Figure 6-10 shows that in the southern sky, our event sample accepts orders of magnitude more neutrino events, especially at energies below 100 TeV and at declinations nearer $\delta = -90°$. In the northern sky, high-level event samples require fewer cuts because the Earth shields IceCube from most atmospheric backgrounds; therefore, the improvement with Level 2 data is only a factor of ~ 2.
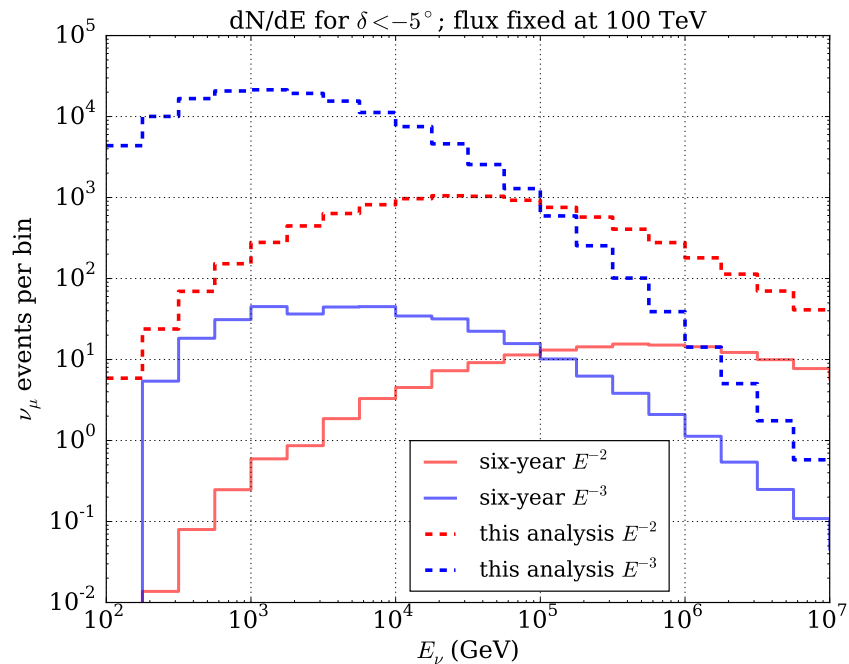
Figure 6-11: Neutrino events per energy bin for this event selection, compared to the six-year analysis, for the southern sky ($\delta < -5°$). An arbitrary flux is fixed at 100 TeV, for power law spectra E^{-2} and E^{-3}. Below 100 TeV, roughly $100\times$ as many muon neutrinos are expected in this analysis.

The expected signal distributions from a source with a power-law neutrino flux are also changed as a result of this event selection. Figure 6-11 compares distributions of detected neutrinos from southern-sky sources in the event selections of this analysis and the six-year analysis. For an arbitrary E^{-2} flux (red), the peak of the distribution shifts left from 1 PeV to about 40 TeV, and gains are larger at lower energies where this analysis makes the most significant improvements to effective area. For an E^{-3} flux, the peak shifts from about 4 TeV to 1 TeV, and more than $100\times$ as many signal neutrinos are expected in this analysis compared to the six-year analysis. Figure 6-12 shows these distributions split into ten declination bands that cover the range of source declinations in this analysis. Since cuts are looser near the horizon, more neutrino events are expected to pass event selection at these declinations.
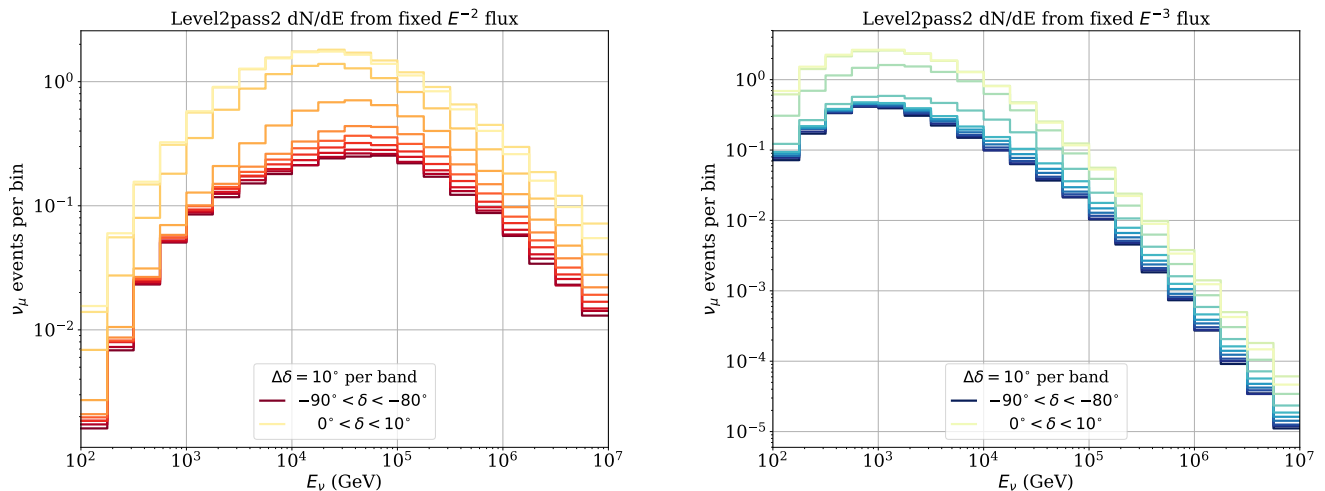
Figure 6-12: For declination bands relevant to this analysis ($\delta < +10°$), the number of events per energy bin is shown for an arbitrary flux. **Left**: For an E^{-2} flux, the curve peaks around 20 – 100 TeV. Acceptance near the horizon is almost an order of magnitude higher than at $\delta = -90°$ **Right**: For an E^{-3} flux, the curve peaks at 1 TeV.

6.5 Analysis Construction

In this analysis I perform two tests for neutrino emission from fast radio bursts, searching expanding neutrino-emission-timescale hypotheses ΔT and using the same test statistic from the six-year FRB analysis,

$$TS = -n_s + \sum_{i=1}^{N} \ln\left(1 + \frac{n_s S_i}{\langle n_b \rangle B_i}\right) \tag{6.2}$$

where TS is maximized with respect to the best-fit number of signal events n_s. N events occur in the on-time window ΔT of an FRB. The probability density of the background PDF at the event location is given by B_i, and the probability density of spatial correlation between the event and its coincident FRB is S_i (see Chapter B for further discussion).

In the stacking test, all events coincident with all FRBs contribute to the test statistic, and $\langle n_b \rangle$ is the expected number of total background events at all sources[9]. In the max-source test, each FRB's respective set of coincident events is considered separately, using $\langle n_b \rangle$ only for one FRB at a time; the largest test statistic among the 28 FRB-TS pairs is the final test result.

---

[9]For example, at $\Delta T = 1$ s, assuming 36 Hz for 28 FRBs, $\langle n_b \rangle \approx 1000$.

The smallest ΔT considered is chosen to be $\Delta T = 10^{-1.5}$ s ≈ 0.03 s so that it contains the largest radio durations in the FRB catalog (Table 6.4). In the stacking test, ΔT expands by a factor of $\sqrt{10}$ until $\Delta T = 10^5$ s (roughly one day, and similar to the stopping time of the six-year analysis). In the max-source test, the analysis sensitivity becomes worse than that of the six-year analysis by $\Delta T = 10^3$ s, so I choose to stop the expansion there.

Results are produced for each time window in each test. The most significant result among time windows in a test was then trials-factor corrected by simulating an expanded unblinding of background via a Monte Carlo program.

28 FRBs are included in this analysis (Figure 6-13 and Table 6.4); these are all FRBs detected and published from 2011 through 2018 as of the finalization of this analysis (Summer 2018). I exclude the repeater, FRB 121102, for several reasons. First, many more repetitions had been reported but not yet published from the source, and I did not want to analyze unpublished detections nor the small published fraction of known detections from the source. Second, the sensitivity of this analysis at the declination of FRB 121102 is unimproved, therefore the limits on that source would be similar to those from the six-year analysis. Third, as of 2018, the absence of detected repetitions from other FRBs suggest that FRB 121102 is an extremely unique member of the source class or a different source altogether [90]. Hadronic models for FRBs exclude FRB 121102, therefore a test for neutrinos from FRBs can justifiably remove FRB 121102 from the analysis.

6.5.1 Sensitivity and discovery potential

The method of signal injection is described in Chapter 5. Comparing this event sample to the high-energy tracks from the six-year FRB analysis, Figure 6-14 shows that the sensitivity to a majority of FRB locations is improved by roughly an order of magnitude.

In the six-year analysis, the background rate was so low that at small ΔT the TS thresholds for sensitivity and discovery potential were equally zero. Table 6.1 shows that this analysis does not start in such a "background-free" regime at $\Delta T = 0.03$ s; however, both sensitivity and discovery
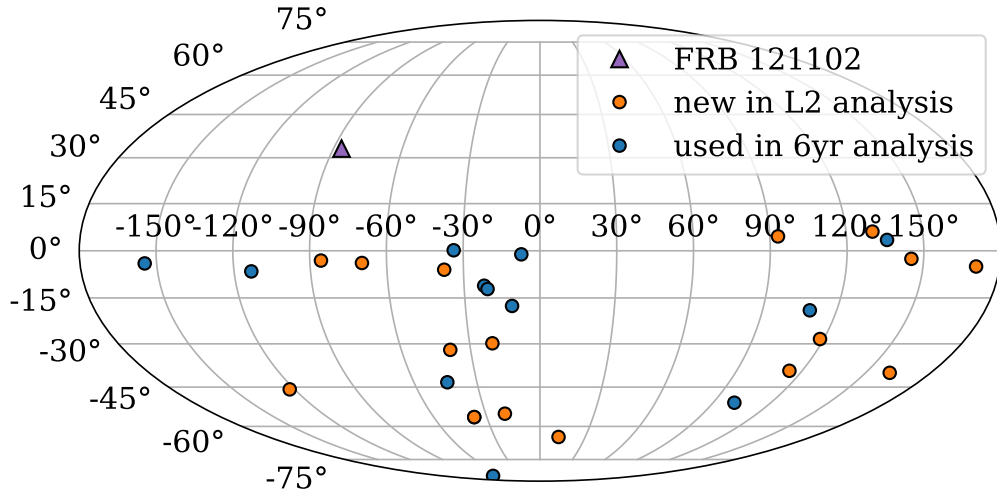
Figure 6-13: A skymap of analyzed FRBs in equatorial coordinates. The repeater, FRB 121102, is excluded from this analysis. All other sources are included, with those previously analyzed with high-energy tracks in blue and new sources in orange.
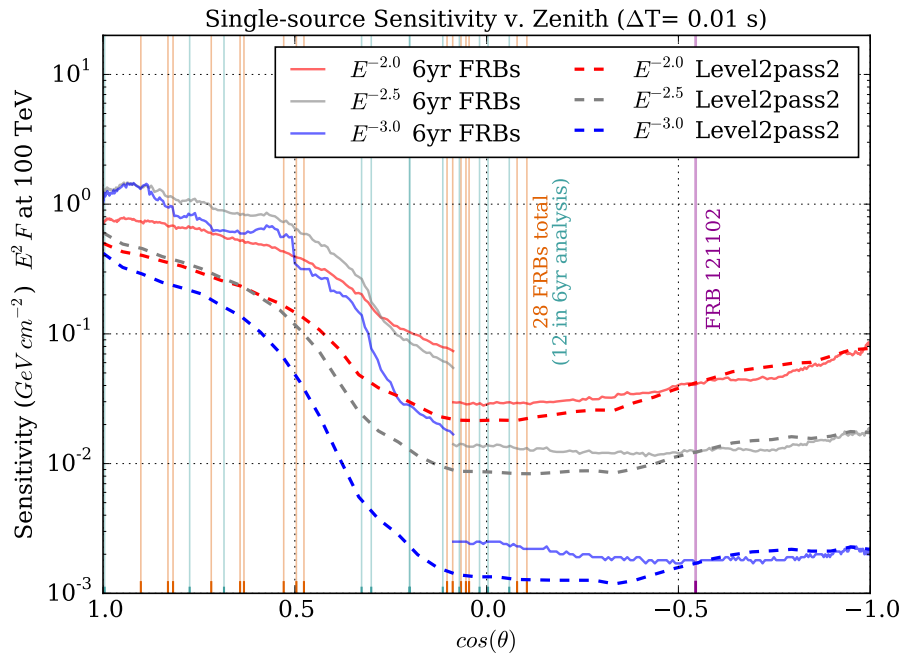
Figure 6-14: The sensitivity of Level-2 MuonFilter to a transient with a duration of 0.01 s is compared to that of the six-year analysis tracks versus zenith angle. On the left, in the southern sky, Level-2 MuonFilter boasts an order-of-magnitude improvement. This is where the majority of new FRB detections have been made. On the right, in the northern sky, the event samples perform similarly at this timescale.

Table 6.1: Test statistic thresholds for time windows in each test. Missing values are represented by "n/a", where computing time to reach sufficient statistics at large ΔT became too high. Discovery potentials are very large at these time windows, so calculating the TS values would only be necessary if the unblinded TS were found to be significantly large. In this case, resources could be dedicated to more background trials to improve the accuracy of the analysis p-value.

ΔT	Stacking TS			Max-source TS		
	median	3σ	5σ	median	3σ	5σ
3.16e-2	0	3.98	12.14	1.13	7.14	15.41
1.00e-1	0	4.10	12.29	1.21	7.29	15.28
3.16e-1	0	4.24	12.34	1.30	7.43	15.46
1.00e-0	0	4.37	12.29	1.40	7.53	16.00
3.16e-0	0	4.39	12.73	1.54	7.69	15.84
1.00e+1	0	4.49	13.25	1.76	8.10	17.11
3.16e+1	0	4.76	n/a	2.03	8.77	18.51
1.00e+2	0	4.94	n/a	2.44	9.97	19.92
3.16e+2	0	5.35	n/a	3.22	12.33	24.05
1.00e+3	0.024	6.13	n/a	5.05	15.47	n/a
3.16e+3	0.208	n/a	n/a	-	-	-
1.00e+4	0.779	n/a	n/a	-	-	-
3.16e+4	2.559	n/a	n/a	-	-	-
1.00e+5	8.023	n/a	n/a	-	-	-

potential in the stacking test are improved by factors of 10 and 50 for power law spectra E^{-2} and E^{-3} respectively (Figure 6-15) due to increased acceptance of signal neutrinos. Figure 6-15 compares these stacking sensitivity values to the constraints derived by not over-producing IceCube's diffuse neutrino flux measurement on neutrino emission from a homogeneous source class of FRBs. By constraining the power law by IceCube's measurement [91], integrating over one day, and dividing by an estimate of FRBs per day in the sky, we arrive at limits one or two orders of magnitude more constraining than from these analysis methods; this calculation is only valid if FRBs form one homogeneous source class.

6.5.2 Unblinding

For the time windows listed in Table 6.1 the TS results from the true on-time data are listed in Table 6.2 along with (pre-trial) p-values corresponding to each window. After correcting for the number of ΔT's searched, the results are consistent with expectations from background alone.
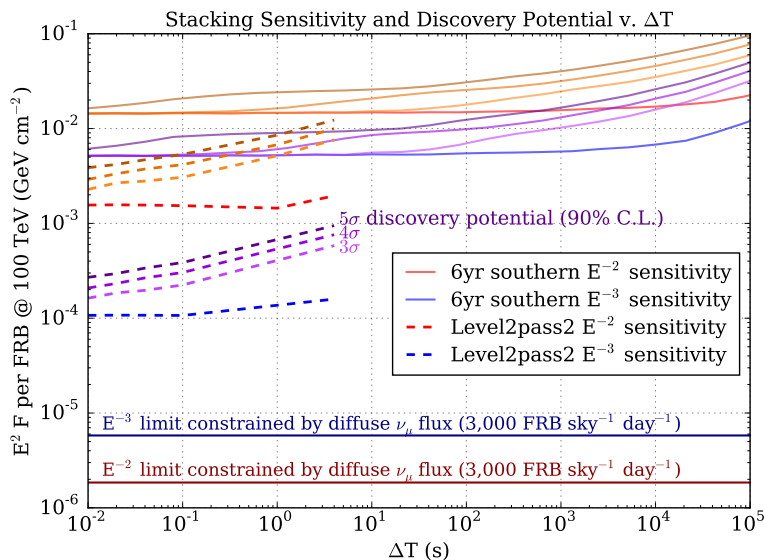
Figure 6-15: Sensitivity and discovery potential of a stacking test of 28 FRBs with Level-2 MuonFilter is shown versus ΔT as E^2 times time-integrated flux. For comparison the sensitivity of the six-year southern-sky stacking search and constraints from IceCube's diffuse astrophysical neutrino flux measurement from [91] are included.

In the stacking test, there are 10^8 events in the largest on-time window, equivalent to more than 1 TB of data to load for unblinding. For time windows larger than 10^3 seconds, I unblind each source separately, saving their respective events' individual contributions to the TS as a function of n_s. Since most events are far from their on-time source, only $\sim 1\%$ of contributions are non-negligible[10] and are saved to disk easily. The TS is then maximized with respect to n_s using a separate optimizer tool, returning the same result as if computer memory allowed a typical unblinding.

6.5.3 Systematics

In the max-source test, the significance of unblinding results increases with ΔT as a result of systematic errors in the background seasonal variation fit. As Figure 6-16 shows, the sine-wave fit implemented I implement in `grbllh` does not perfectly fit the on-time rates observed in data. In a typical transient search where $\langle n_b \rangle < 10^2$, a 2% underestimation of the rate in on-time data

---

[10]`grbllh` allows a lower threshold to be set for $r_i = S_i/(\langle n_b \rangle B_i)$. When unblinding, setting all $r_i < 10^{-10}$ to zero greatly improves computational speed without affecting analysis results.

Table 6.2: Unblinded TS values for stacking and max-source tests, with pre-trial p-values for results in their respective time windows. Both tests produce most significant results in $\Delta T = 10^3$ s, where post-trials significance for the stacking and max-source tests are $p = 0.35$ and $p = 0.33$ respectively.

	Stacking TS			Max-source TS		
ΔT	median	**result**	p	median	**result**	p
3.16e-2	0	0	1	1.13	0.32	0.87
1.00e-1	0	0	1	1.21	1.10	0.54
3.16e-1	0	0	1	1.30	1.31	0.49
1.00e-0	0	0	1	1.40	0.12	0.98
3.16e-0	0	0	1	1.54	1.35	0.57
1.00e+1	0	0.29	0.124	1.76	2.38	0.32
3.16e+1	0	0.02	0.256	2.03	2.85	0.27
1.00e+2	0	0.07	0.274	2.44	4.86	0.07
3.16e+2	0	0	1	3.22	6.06	0.08
1.00e+3	0.024	2.32	0.042	5.05	10.57	0.05
3.16e+3	0.208	1.64	0.141	-	-	-
1.00e+4	0.779	0.79	0.492	-	-	-
3.16e+4	2.559	0	1	-	-	-
1.00e+5	8.023	0	1	-	-	-

Table 6.3: The effects of an error in background rate estimation are produced by repeating the unblinding with the background rate artificially increased/reduced. A 2% change in the background estimation has a larger effect on the results at $\Delta T = 1000$ s than at $\Delta T = 10$ s.

	$\Delta T = 10$ s		$\Delta T = 1000$ s	
$f \times$livetime	TS	p	TS	p
$f = 0.98$	2.32	0.34	8.46	0.16
$f = 1.00$	**2.38**	**0.32**	**10.57**	**0.05**
$f = 1.02$	2.43	0.31	12.45	0.02

results an average counting-experiment significance of $< 0.2\sigma^{11}$, which is still background-like. The systematic error doesn't affect significance for small $\langle n_b \rangle$

However, at $\Delta T = 10^3$ s, $\langle n_b \rangle \approx 3.5 \times 10^4$. The significance of a 2% perceived excess $N = 35700$ at this $\langle n_b \rangle$ is 3.7σ. To account for this systematic effect, I compute the max-source TS for background rates between 98% and 102% of the sinusoid fit in Figure 6-16 and set limits as a range covering 90% of systematic background errors in the source list.

---

[11]If we expect 100 events, but in reality the background rate is 102 events, then the average significance above the mean in our test is $(102 - 100)\sigma/\sqrt{100} = 0.2\sigma$
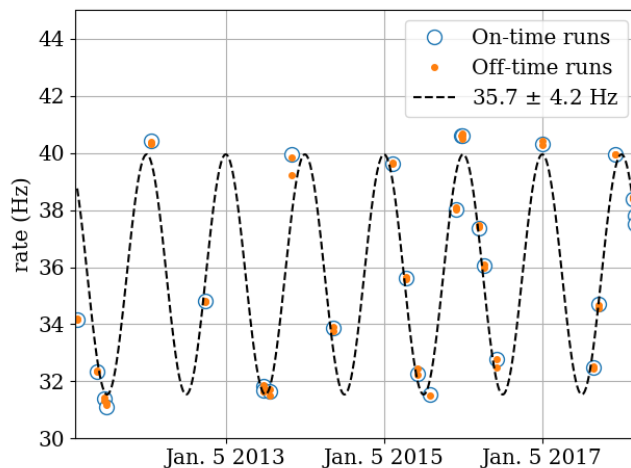
Figure 6-16: The sine-wave seasonal variation fit in `grbllh` is compared to the true rates from off-time-run rates used for the fit and the on-time-run rates it intends to predict.

Two points should be made to avoid this effect in the future.

1. In the regime where $\langle n_b \rangle$ is very large, the precedent for use of the transient TS may be lost. For example, in 10^3 s this event sample contains 35000 events, but Level-2 MuonFilter only detects about 10 astrophysical neutrino events *per day.* The Poisson term in the transient likelihood then cannot contribute significance based on a perceived excess of astrophysical events in background; it only poses a risk of biasing the observation based on background parameterization errors. Instead, the TS could transition to a steady-source likelihood in the on-time where systematic errors are an issue.

2. The sine-wave fit is designed for fits to low-rate event samples with relatively large per-run statistical error, but here a spline fit could have been applied to each off-time run; or more simply, the on-time $\langle n_b \rangle$ could be estimated by the average of adjacent off-time rates. The rate-to-rate variation in Level-2 MuonFilter can still be as high as 2%, so this change alone would not solve the issues specific to this analysis at large ΔT.
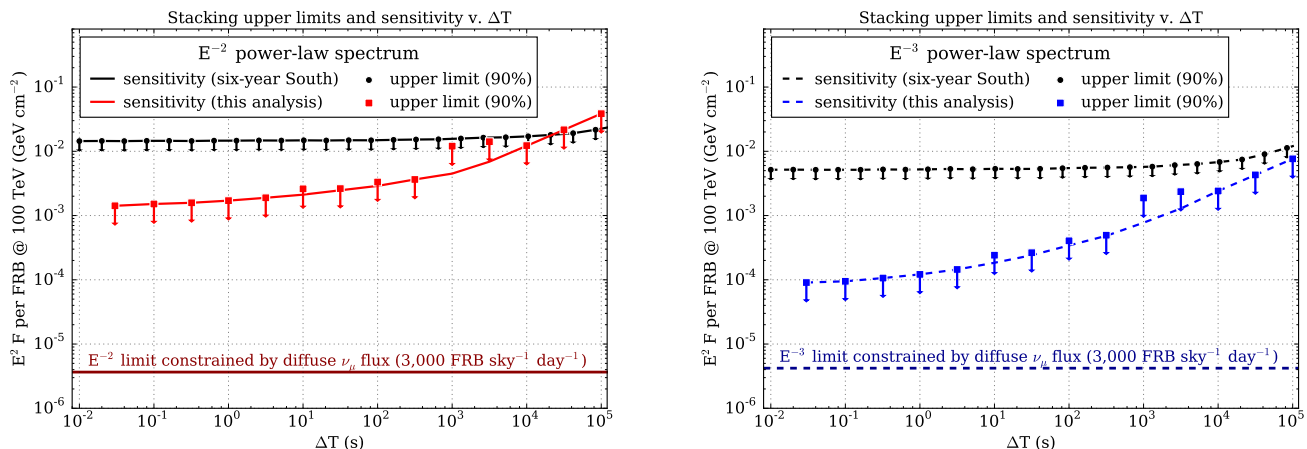
Figure 6-17: Left: Upper limits at a 90% confidence level for per-FRB time-integrated neutrino flux from a stacked search of 28 FRB sources. Limits are set for an E^{-2} power-law emission spectrum. **Right**: Stacking per-FRB limits are set for an E^{-3} power-law spectrum.

6.6   Upper Limits

The post-trials p-values for the stacking and max-source tests are 0.35 and 0.33 respectively. Because the results are consistent with the background-only hypothesis, upper limits are set on FRB neutrino emission for each ΔT by injecting signal until 90% of signal trials have a TS exceeding the observed result. If the observed TS is less than the median background TS in a time window, the sensitivity is quoted as the upper limit.

Figure 6-17 shows stacking upper limits on per-FRB neutrino emission for power-law spectra E^{-2} and E^{-3}. For E^{-2}, the limits at small ΔT are improved by a factor of 10 from the six-year analysis; at 10^4 s the background from Level-2 becomes so large that the upper limits are roughly equivalent. For E^{-3}, this analysis' larger acceptance for low-energy neutrinos results in an improvement by a factor of 50 at small ΔT.

At small ΔT, the stacking limits scale with the number of sources and the average of source-declination sensitivities. With CHIME expected to report hundreds of FRB detections per year in the northern sky [69], the limits at E^{-3} could become more constraining than those of the diffuse flux by the year $\sim$2020. Southern observatories will also be reporting more FRB detections, among
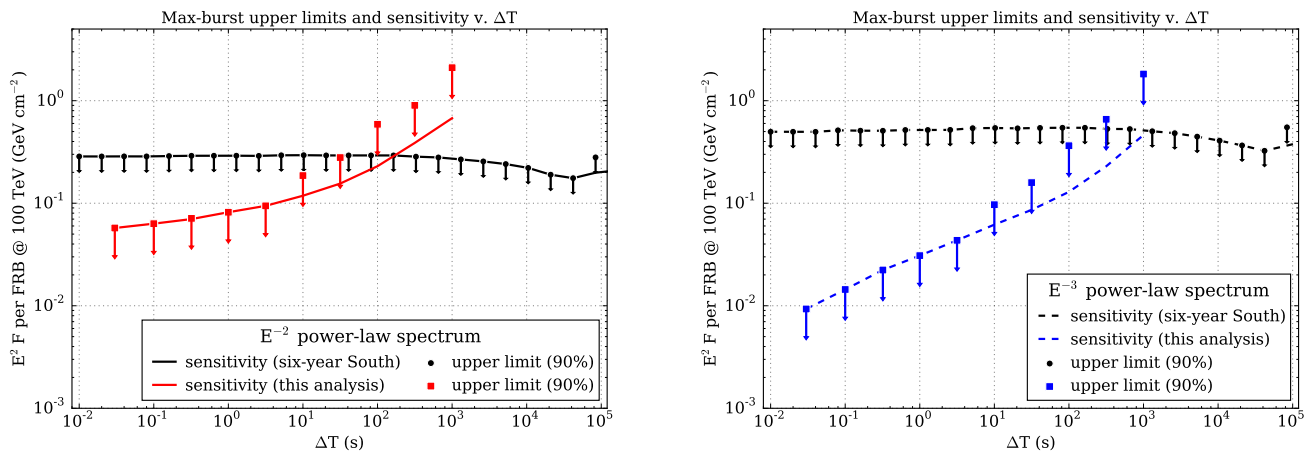
Figure 6-18: Left: Upper limits at a 90% confidence level for time-integrated neutrino flux from the brightest FRB in a max-burst search of 28 FRB sources. Limits are set for an E^{-2} power-law emission spectrum. **Right**: Stacking per-FRB limits are set for an E^{-3} power-law spectrum.

which the near-horizon sources produce larger improvements in IceCube's sensitivity. Figure 6-18 shows the limits this analysis sets on the max-source neutrino emission; this is a 90% upper limit on the time-integrated neutrino flux from the brightest of 28 sources. The steepness of the curve relative to the six-year analysis is due to a combination of factors: first and most obviously, the background rate in this analysis is four orders of magnitude larger; second, the average angular uncertainty is larger, so there is no ΔT for which zero spatially coincident events are expected among 28 sources; and third, the number of sources has increased from 9 to 28[12].

---

[12]In the max-burst test, the sensitivity does not improve with the number of sources (as it does in stacking). Approaching a background-free regime, sensitivity will scale with the 90th percentile of per-source sensitivities. As background increases, the TS threshold scales with the number of sources, increasing the steepness of the sensitivity versus ΔT.

Table 6.4: FRBs are marked by analysis with ■: "1yr", "6yr", and "L2" refer to analyses discussed here, and "SN" refers to Ali Kheirandish's analysis using the Supernova DAQ. Repetitions of FRB 121102 are denoted with "b0", "b1", etc. (http://www.frbcat.org, [92])

FRB	1yr	6yr	SN	L2	Time (UTC)	ΔT (ms)	RA	DEC
FRB 110220		■	■	■	2011-02-20 01:55:48.957	5.6	22h 34$'$	-12° 24$'$
FRB 110523	■	■	■	■	2011-05-23 15:06:19.738	1.73	21h 45$'$	-00° 12$'$
FRB 110626	■	■	■	■	2011-06-26 21:33:17.474	< 1.4	21h 03$'$	-44° 44$'$
FRB 110703	■	■		■	2011-07-03 18:59:40.591	< 4.3	23h 30$'$	-02° 52$'$
FRB 120127	■	■	■	■	2012-01-27 08:11:21.723	< 1.1	23h 15$'$	-18° 25$'$
FRB 121002		■	■	■	2012-10-02 13:09:18.402	2.1; 3.7	18h 14$'$	-85° 11$'$
FRB 121102 b0		■	■		2012-11-02 06:47:17.117	3.3	05h 32$'$	33° 05$'$
FRB 130626		■	■	■	2013-06-26 14:56:00.06	< 0.12	16h 27$'$	-07° 27$'$
FRB 130628		■	■	■	2013-06-28 03:58:00.02	< 0.05	09h 03$'$	03° 26$'$
FRB 130729		■	■	■	2013-07-29 09:01:52.64	< 4	13h 41$'$	-05° 59$'$
FRB 131104		■	■	■	2013-11-04 18:04:01.2	< 0.64	06h 44$'$	-51° 17$'$
FRB 140514		■		■	2014-05-14 17:14:11.06	2.8	22h 34$'$	-12° 18$'$
FRB 150418		■	■	■	2015-04-18 04:29:05.370	0.8	07h 16$'$	-19° 00$'$
FRB 121102 b1		■	■		2015-05-17 17:42:08.712	3.8	05h 32$'$	33° 05$'$
FRB 121102 b2		■	■		2015-05-17 17:51:40.921	3.3	05h 32$'$	33° 05$'$
FRB 121102 b3		■	■		2015-06-02 16:38:07.575	4.6	05h 32$'$	33° 05$'$
FRB 121102 b4		■	■		2015-06-02 16:47:36.484	8.7	05h 32$'$	33° 05$'$
FRB 121102 b5		■	■		2015-06-02 17:49:18.627	2.8	05h 32$'$	33° 05$'$
FRB 121102 b6		■	■		2015-06-02 17:49:41.319	6.1	05h 32$'$	33° 05$'$
FRB 121102 b7		■	■		2015-06-02 17:50:39.298	6.6	05h 32$'$	33° 05$'$
FRB 121102 b8		■	■		2015-06-02 17:53:45.528	6.0	05h 32$'$	33° 05$'$
FRB 121102 b9		■	■		2015-06-02 17:56:34.787	8.0	05h 32$'$	33° 05$'$
FRB 121102 b10		■	■		2015-06-02 17:57:32.020	3.1	05h 32$'$	33° 05$'$
FRB 150610				■	2015-06-10 05:26:59.396	2.00	10h 44$'$	-40° 05$'$
FRB 150807				■	2015-08-07 17:53:55.83	0.35	22h 42$'$	-55° 05$'$
FRB 121102 b11		■			2015-11-13 08:32:42.375	6.73	05h 32$'$	33° 05$'$
FRB 121102 b12		■			2015-11-19 10:44:40.524	6.1	05h 32$'$	33° 05$'$
FRB 121102 b13		■			2015-11-19 10:51:34.957	6.14	05h 32$'$	33° 05$'$
FRB 121102 b14		■			2015-11-19 10:58:56.234	4.3	05h 32$'$	33° 05$'$
FRB 121102 b15		■			2015-11-19 11:05:52.492	5.97	05h 32$'$	33° 05$'$
FRB 151206				■	2015-12-06 06:17:52.778	3.00	19h 21$'$	-04° 08$'$
FRB 121102 b16		■			2015-12-08 04:54:40.262	2.5	05h 32$'$	33° 05$'$
FRB 151230				■	2015-12-30 16:15:46.525	4.40	09h 41$'$	-03° 27$'$
FRB 160102				■	2016-01-02 08:28:39.374	3.40	22h 39$'$	-30° 11$'$
FRB 160317				■	2016-03-17 09:00:36.53	21.00	07h 54$'$	-29° 37$'$
FRB 160410				■	2016-04-10 08:33:39.68	4.00	08h 41$'$	06° 05$'$
FRB 160608				■	2016-06-08 03:53:01.088	9.00	07h 37$'$	-40° 48$'$
FRB 170107				■	2017-01-07 20:05:45.139	2.60	11h 23$'$	-05° 00$'$
FRB 170827				■	2017-08-27 16:20:18	0.40	00h 49$'$	-65° 33$'$
FRB 170922				■	2017-09-22 11:22:23.40	26.00	21h 30$'$	-08° 00$'$
FRB 171209				■	2017-12-09 20:34:23.50	2.50	15h 50$'$	-46° 10$'$
FRB 180301				■	2018-03-01 07:34:19.76	3.00	06h 13$'$	04° 34$'$
FRB 180309				■	2018-03-09 02:49:32.99	0.58	21h 25$'$	-33° 59$'$
FRB 180311				■	2018-03-11 04:11:54.80	12.00	21h 32$'$	-57° 44$'$

Chapter 7

Novae

This chapter describes my work preparing an analysis in search of neutrino emission from galactic novae. The analysis is unfinished, but the material here should serve as comprehensive documentation for another student considering to continue and complete this work.
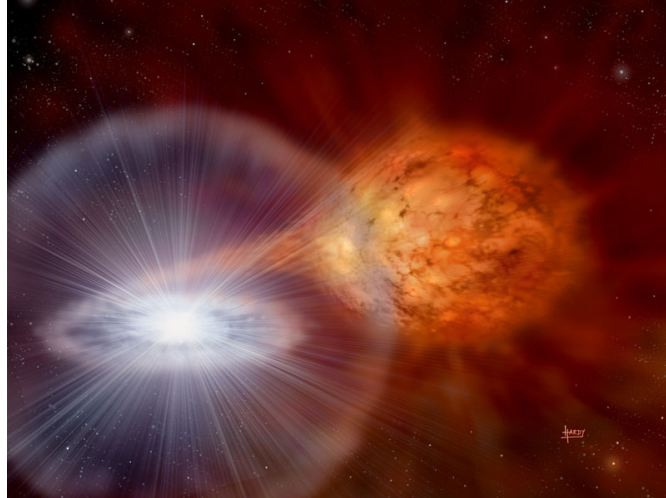
Figure 7-1: An artist's depiction of a symbiotic nova. Image from NASA's *Astronomy Picture of the Day* series (https://apod.nasa.gov/apod/ap060726.html). Credit: David A. Hardy.

7.1 History and Background

The name *nova* is borrowed from the Latin word meaning "new", first used in astronomy by the Danish astronomer Tycho Brahe, who coined the term after observing the appearance of a new star in the night sky: supernova SN 1572. The term was used for all new, extremely bright sources until the 1930s, when observed differences warranted separate classifications and "supernova" was coined by Walter Baade and Fritz Zwicky [93]. Today we know that a supernova is not technically a *new* astrophysical object, only a *newly visible* source because of the tremendous luminosity resulting from a dying star. Similarly, novae are a Galactic[1] astronomical source class – separate from supernovae – characterized by suddenly increased luminosity.

In 1954, spectroscopic observations of cataclysmic variable AE Aquarii revealed Doppler shifted emission lines consistent with orbital velocities on the order of 100 km/s in a stellar binary [94]. Further studies deduced that binary accretion is the source of energy for the outbursts [95] and that the optical properties of novae are determined largely by the binary's larger member [96]. The accreting companion was identified through the discovery of abundances of neon and heavier elements in the ejecta, most likely resulting from upward mixing of accreting matter with the surface of an oxygen-neon-magnesium white dwarf [97].

Observations of novae support two binary system classes. In a symbiotic nova, the white dwarf accretes matter from a red giant companion [98]. Ejecta from the white dwarf encounters the dense stellar wind from its companion, creating blast waves capable of gamma ray emission. In a classical nova, the companion of the white dwarf is instead a low-mass main sequence star, the environment of which is not dense enough to support the same high-energy emission models as its symbiotic counterpart. Nevertheless, both are observed to be GeV gamma-ray sources.

---

[1]Extragalactic novae have also been discovered, however the proximity of Galactic sources makes them easier to study because of their greater incident flux.

7.1.1 Gamma-ray detection

The *Fermi* Large Area Telescope (*Fermi*-LAT) is a gamma-ray detector in orbit since 2008 with sensitivity to photons from 20 MeV to 300 GeV. After *Fermi* found gamma rays from the symbiotic nova V407 Cygni [99], high-energy emission was only thought possible via interactions of white dwarf ejecta with the high-density environment provided by a red giant companion. This made *Fermi*-LAT's discovery in 2014 of gamma ray emission from classical novae even more surprising [100]. Since all *Fermi*-detected novae are at distances < 10 kpc and have otherwise ordinary properties, it may be that all novae are gamma-ray emitters.

Fermi has detected more than a dozen at $E_\gamma > 100$ MeV (Table 7.1) [101]. The majority have best-fit gamma-ray spectra with cut-off energies (E_C in Eq. 7.1), each with $E_C < 10$ GeV.

$$\Phi = \Phi_0 \cdot \Big(\frac{E}{\text{GeV}}\Big)^{-\gamma} \cdot \exp\Big(-\frac{E}{E_C}\Big) \tag{7.1}$$

However, for about half of *Fermi*'s novae, a constant power law or broken power law are also adequate fits (e.g., V1324 Sco and V339 Del, in Figure 4 of [101]).

Correlation of optical and gamma-ray light curves for ASASSN-16ma has been used to argue in favor of hadronic acceleration models for novae. The observed acceleration of nova outflow requires magnetic field properties which would imply significant synchrotron cooling in leptonic models, but this cooling is not seen [102]. In the shock acceleration model, gamma rays are produced by the decay of neutral pions created through proton-proton collisions in the outflow. Charged pions created in these collisions would produce GeV neutrinos through decay, motivating an IceCube analysis of novae.

Name	Distance (kpc)	Start Date	Duration (days)	RA (°)	Dec (°)
V407 Cyg 2010$^{Sym.}$	2.7	2010-03-10	22	315.54	45.78
V1324 Sco 2012	4.5	2012-06-15	17	267.72	-32.62
V959 Mon 2012	3.6	2012-06-19	22	99.91	5.90
V339 Del 2013	4.2	2013-08-16	27	305.88	20.77
V1369 Cen 2013	2.5	2013-12-02	39	208.70	-59.15
V745 Sco 2014	11±3	2014-02-06	2	268.84	-33.25
V1535 Sco 2015	7.3	2015-02-14	7	255.86	-35.07
V5668 Sgr 2015	2.0	2015-03-15	55	279.24	-28.93
V407 Lup 2016	3.4±1.3	2016-09-24	?	232.26	-44.83
V5855 Sgr 2016	?	2016-10-20	?	272.62	-27.50
V5856 Sgr 2016	4.2	2016-10-25	12±3	275.24	-28.36

Table 7.1: List of galactic novae with gamma-ray emission detected by *Fermi*-LAT (as of October 2018). All are classical novae with the exception of V407 Cyg, which is symbiotic as noted. Some novae have unknown duration – V407 Lup (ASASSN-16kt) and V5855 Sgr (TCP J18102829-2729590) – because they were first discovered in a declining flare state and no archival data can confirm the start date [103]. For these novae, the start dates given are the earliest known time of gamma-ray emission.

7.1.2 Signal-to-background estimates

Metzger et al. presented a back-of-the-envelope calculation predicting the number of background and signal events IceCube might see in a search for neutrino emission from nova V1324 Sco[2] [104]. In the paper, IceCube's effective area at trigger level is used when predicting signal events. However, this expectation is then compared to a background rate taken from an event selection with much stricter cuts – an IceCube-DeepCore transients paper from 2015, which is often referred to as the "Low-energy Transients" paper [38] (also Jacob Daughhetee's PhD thesis [105]) – therefore exaggerating IceCube's sensitivity to the specific test case. Using the same technique, I present a direct comparison of background and signal estimates for V1324 Sco using the same Low-energy Transients sample.

V1324 Sco became visible to *Fermi* on June 15, 2012 and remained bright in gamma rays for

---

[2]Variable stars were once named with a pair of letters and the constellation to which they are nearest. Eventually, astronomers realized their catalog of discoveries would outgrow this scheme, and they began simply numbering discoveries chronologically with "V" (for "variable") followed by their number and the constellation abbreviation ("Sco" for Scorpio, for instance).
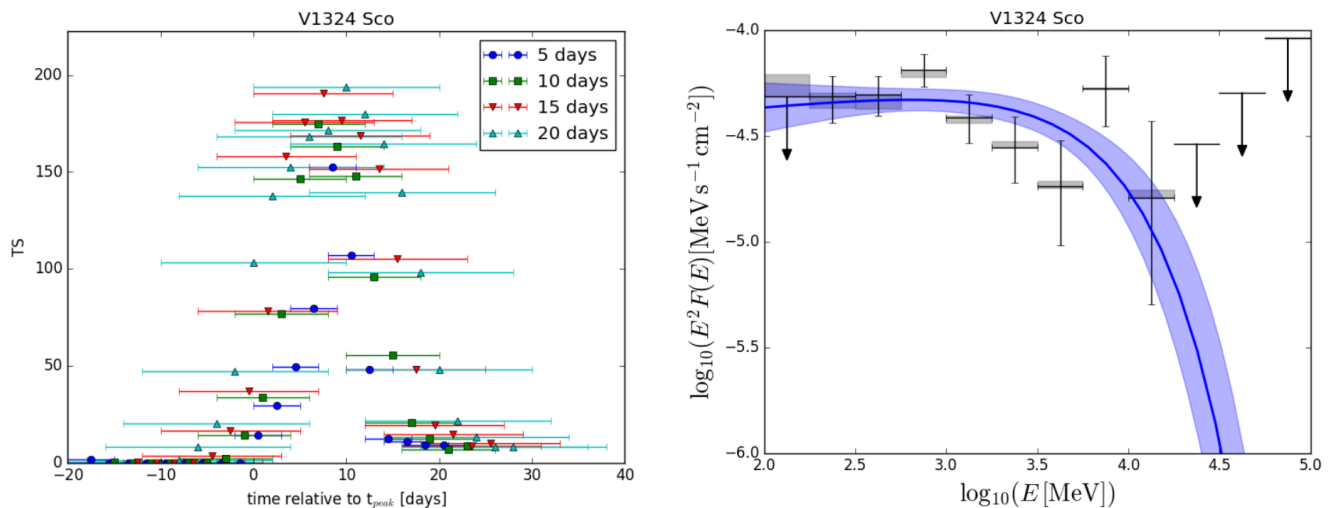
Figure 7-2: Left: The timescale of significant gamma-ray detection of V1324 Sco by *Fermi*-LAT is shown. Marker styles indicate separate temporal binning schemes to calculate a test statistic. The duration of the nova is about 17 days. **Right:** A spectral fit is performed with a cut-off energy $E_C = 7.7$ GeV. Metzger et al. fit this data with an unbroken $E^{-2.1}$ spectrum. Plots are from Franckowiak et al. [101]

17 days (Figure 7-2). Metzger et al. fit its spectrum with an unbroken power law given by $\frac{dN_\gamma}{dE} = 10^{-10} (\frac{E}{\text{GeV}})^{-2.1}$ erg s^{-1} cm^{-2}. Estimating the effective area in the relevant energy regime to be $A_{eff} \approx 4 \cdot 10^{-4} (\frac{E}{\text{GeV}})^{2.1}$ cm^2 (see Figure 7-3; $E^{2.1}$ is chosen to exactly cancel the dN/dE for this slope consistent with $\sim E^2$.), and assuming for now that neutrino emission is correlated one-to-one with the detected gamma rays, the number of signal neutrinos from V1324 Sco in IceCube can be calculated.

$$N_{Signal} = \int_{10 \text{ GeV}}^{E_{max}} \frac{dN}{dE} \cdot A_{eff} \cdot T_{emission} \cdot dE$$
$$\approx 3.7 \cdot 10^{-5} \frac{E_{max}}{\text{GeV}}$$

(7.2)

Therefore IceCube detection of a signal neutrino from V1324 Sco would only be expected if a power law spectrum for neutrino and gamma-ray emission remains unbroken up to $E_{max} > 10$ TeV.

For background comparison, the zenith distribution is roughly flat over a solid angle of 2.17π (Figure 7-4), and the median angular error assigned to events is optimistically as small as $5°$
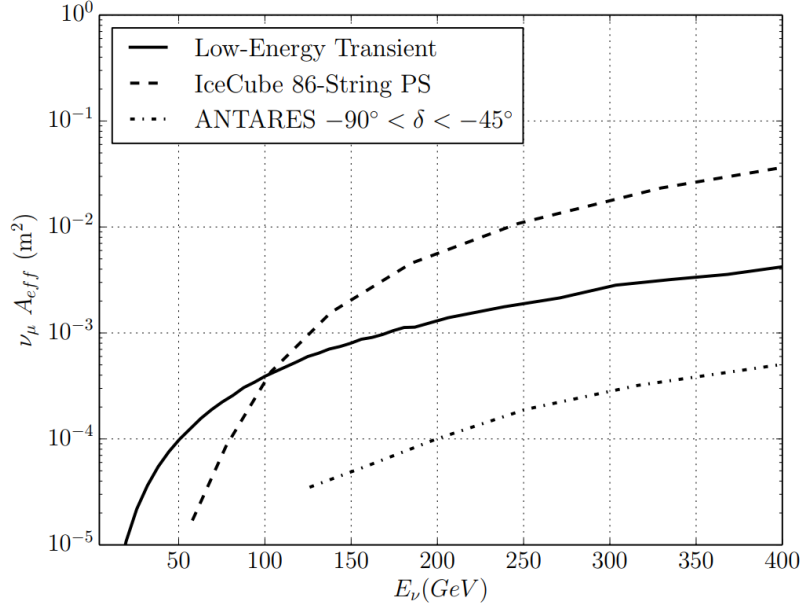
Figure 7-3: The effective area from IceCube's low-energy transients analysis [38], that compares effective area for low-energy muon neutrinos to the event selections for four-year point-source searches by IceCube [84] and ANTARES [106].
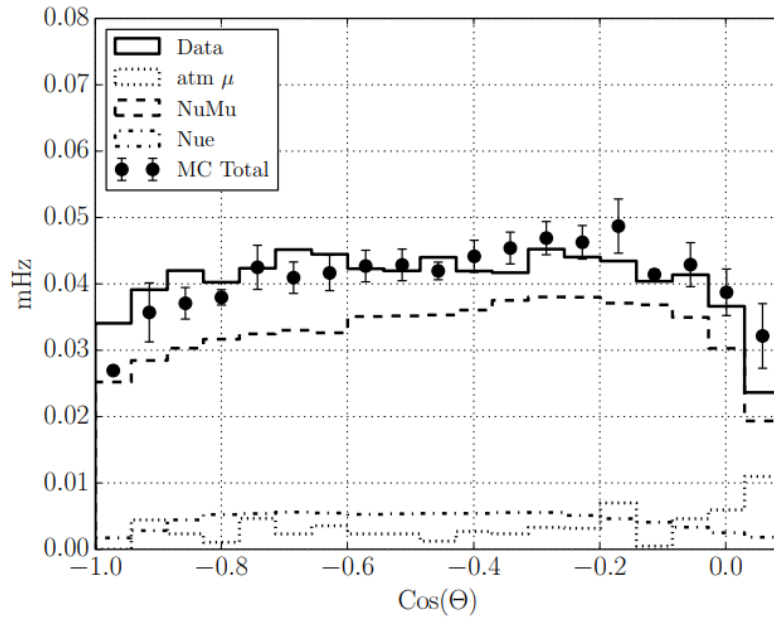
Figure 7-4: The distribution of reconstructed zenith angles from IceCube's low-energy transients analysis [38]. Real data is represented by the solid black line; contributions from various simulated species are also shown, adding to form the black points with statistical error bars.

(Figure 2 in [38]). Using this, the number of background events with 90% containment contours containing the source is given by

$$N_{Background} = (0.77 \text{ mHz} \cdot T_{emission}) \cdot \left(\frac{A_{90\%}}{2.17\pi}\right)$$
$$= (1131 \text{ events}) \cdot \left(\frac{2\pi \ (1 - \cos(10.73°))}{2.17\pi}\right) \qquad (7.3)$$
$$= 18.2 \text{ events}$$

$$\text{where} \ \ r_{90\%} = \sigma \cdot \sqrt{2 \ \ln(\frac{1}{1 - 0.90})} = \sigma \cdot 2.146 = 10.73°$$

These estimates suggest that for the "Low-energy Transients" event sample, an IceCube search may not have promising prospects for discovery. As a counterargument, in addition to optimizing a different event sample specifically for an analysis of novae, the following possibilities could yield significant sensitivity improvements:

- power law spectra can have no cut-offs or cut-offs exceeding 1 TeV

- a nova can be detected at a distance < 1 kpc (expected once per decade)

- gamma rays can be attenuated by environment; neutrino flux can exceed detected gamma-ray flux

- neutrino emission could possible occur on shorter timescales than gamma-ray emission (lower effective background per source)

- many novae could be stacked in a search

7.2   GRECO Event Sample

Measurements of nova gamma-ray spectra by *Fermi* motivate an IceCube neutrino sample to be optimized for detection at energies near the detected gamma-ray energies. For detection of

Event sample	Rate (mHz)	Coverage (sr)	Years	Active?
Low-energy Transients	0.77	2.17π ($\delta > -5°$)	IC86-2	No
GRECO	0.87	4π	IC86-2 – IC86-6	Yes

Table 7.2: Comparison of candidate IceCube event samples for analysis of novae.
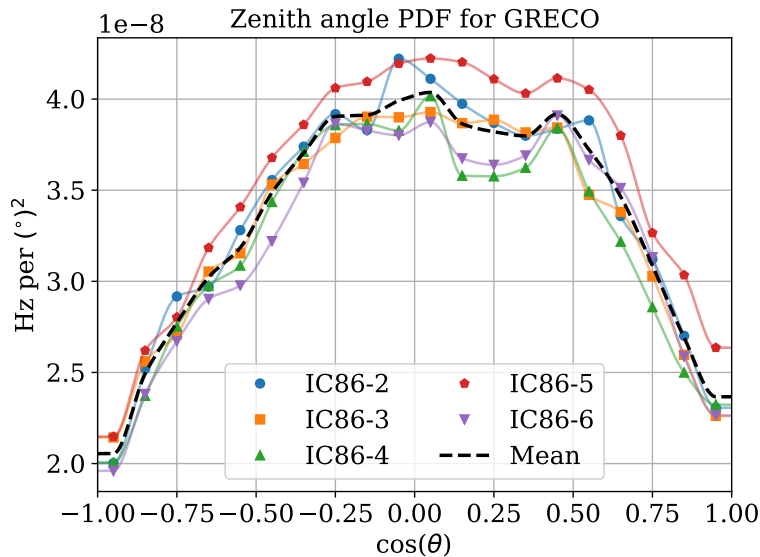
Figure 7-5: Distributions of reconstructed zenith angle from PegLeg muon track fit for events in the GRECO event selection.

astrophysical neutrinos between 1 GeV and 10 TeV, the most sensitive available IceCube sample is GRECO – GeV Reconstructed Events with Containment for Oscillations [107].

7.2.1 Data

GRECO data are currently available for the years IC86-2 through IC86-6[3] (Figure 7-5, Figure 7-6). The best fit currently available is PegLeg, which is an IceCube event reconstruction that fits both a cascade and track using information of hit and unhit DOMs (returning the interaction vertex, time, direction, track length, and energy – track energy if track length exceeds 50 meters, otherwise cascade energy). For initial studies, I use the direction and other properties of PegLeg's muon track fit.

---

[3]`/data/ana/LE/NBI_nutau_appearance/current_pickle_files/current/merged_final/Level7_data`
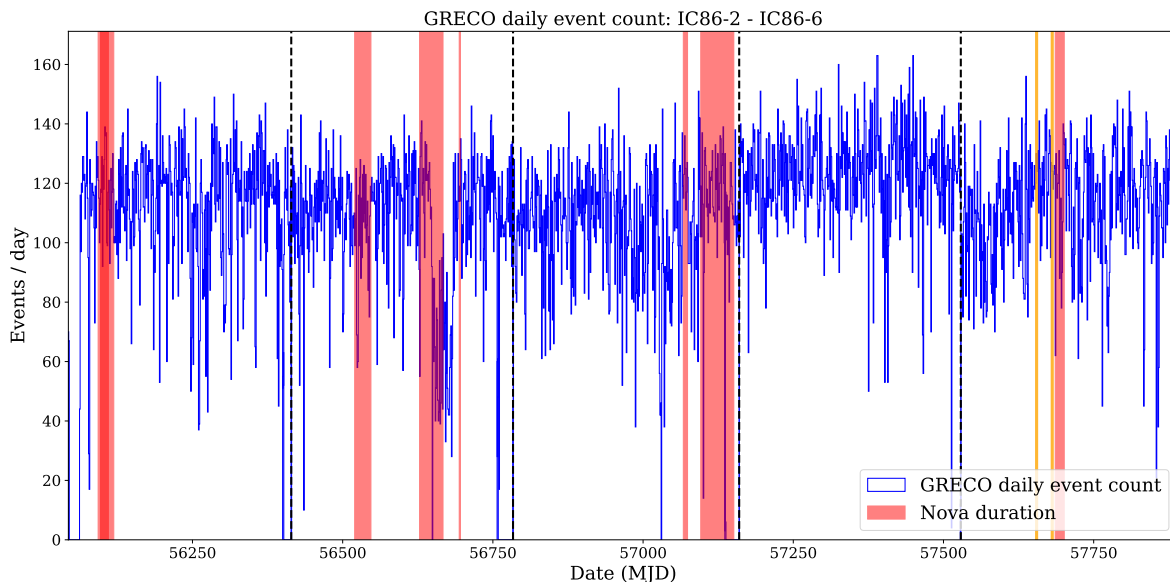
Figure 7-6: GRECO event rate during gamma-ray-detected emission from novae (Table 7.1). The gold regions in IC86-6 correspond to novae first discovered while their gamma-ray flux was in decline; the start times for these novae are unknown.

7.2.2   Simulation

GRECO simulation is split into three energy regimes: $E_\nu < 1$ TeV (Genie[4], IceCube neutrino simulation at energies below 1 TeV), 1 TeV $< E_\nu < 5$ TeV ("low-energy" NuGen[5]), and 5 TeV $< E_\nu$ ("medium-energy" NuGen[6]). There are problems with the documentation of simulation variables necessary to calculate effective areas (see effect at 5 TeV in Figure 7-8) and with a lack of higher energy simulation (lack of statistics above 20 TeV in same figure). For now though, it is sufficient to make signal estimates for novae under the hypothesis that neutrino emission closely follows the gamma-ray spectrum as measured by *Fermi*.

7.2.3   Signal estimates

Using effective area curves generated from simulation, model-dependent signal estimates can be calculated using Eq. 7.2. In Figure 7-9, the neutrino flux from V1324 Sco is assumed to have

---

[4] /data/ana/LE/NBI_nutau_appearance/level7_5July2017/genie/1x640, x=(2,4,6) for (ν_e, ν_μ, ν_τ)

[5] /data/ana/LE/NBI_nutau_appearance/level7_5July2017/nugen/numu_LE

[6] /data/ana/LE/NBI_nutau_appearance/level7_5July2017/nugen/numu_ME
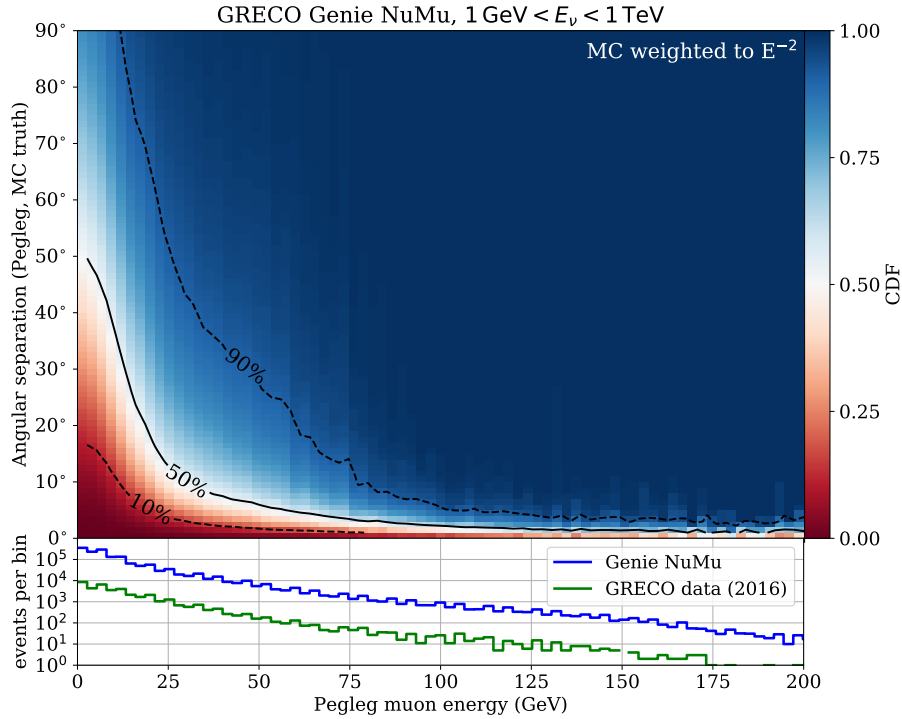
Figure 7-7: GRECO simulation is binned in estimated muon energy; within each bin, a CDF is built over the magnitude of angular separation between the PegLeg track and MC truth. Ringing in the lower histograms is due to the limited discrete values assigned by PegLeg to muon energy; bins including more or fewer of these possible values appear as small peaks or troughs in the distribution.
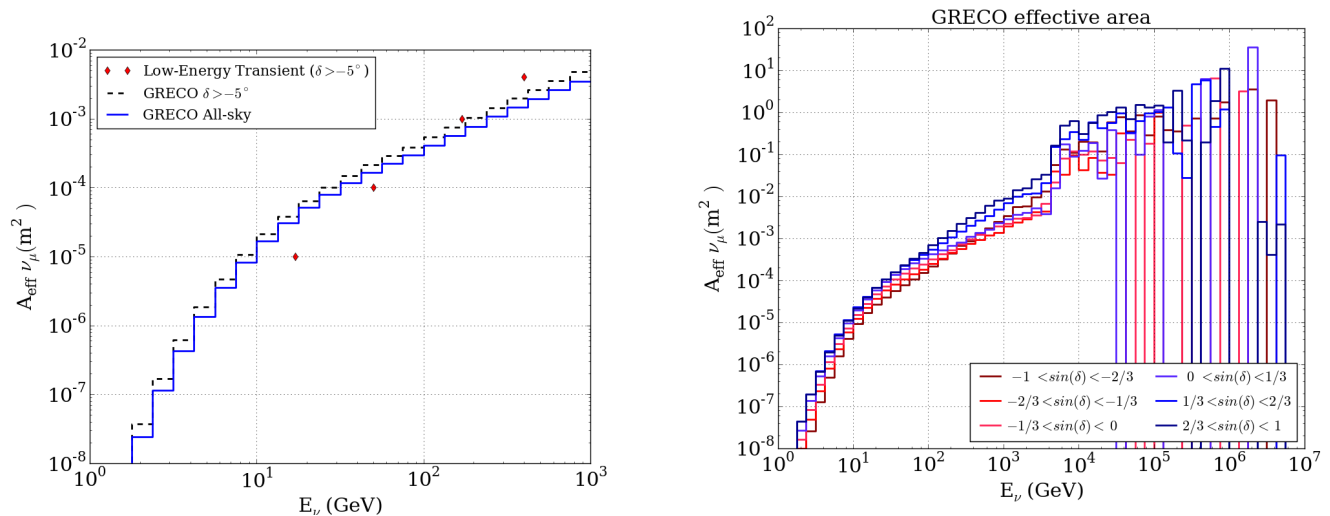
Figure 7-8: **Left:** GRECO effective area compared to the low-energy transients event sample [38]. **Right:** GRECO effective area in declination bands. Statistics need to be improved with more simulation to provide a continuous effective area at higher energies.
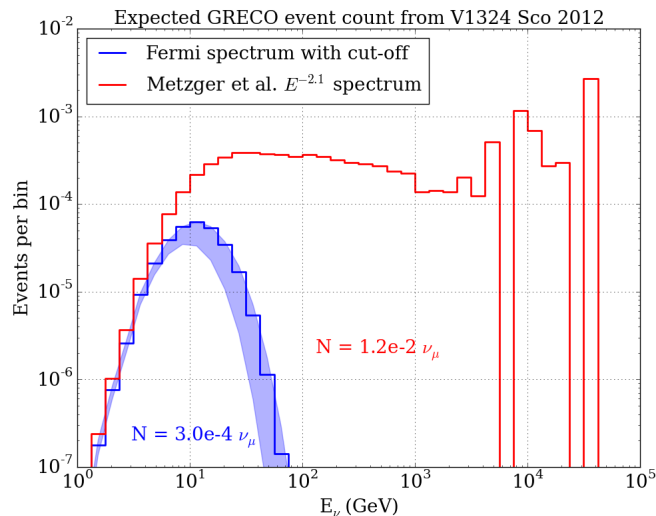
Figure 7-9: Converting the measured gamma-ray flux directly to neutrino flux, signal estimates for V1324 Sco are shown for spectral fits with and without an exponential cut-off factor.

the same spectrum and time dependence as the gamma-ray flux. Depending on the extrapolation of *Fermi* data, the expected signal under this hypothesis is 10^{-4} to 10^{-2} signal events; this is potentially greater than the signal expectation from Eq. 7.2, which assumed an effective area shape that is valid up to about 200 GeV (7.4×10^{-3} signal neutrinos). From Figure 7-5, the background density in 17 days is roughly 0.06 events per square degree – 18 events within $10°$ of the source (see distribution of angular separations in Figure 7-7).

The same estimates can be performed for any nova of known gamma-ray flux and duration. Figure 7-10 shows signal-to-background estimates for six novae from [101].

7.3 Future Work

7.3.1 Event sample

Since the current list of novae is relatively small, each additional source detection can noticeably improve sensitivity in a stacking analysis, so no specific date cut-off is planned until the analysis is more mature. Once an end date is known, data may need to be processed for additional years to analyze more recent novae.
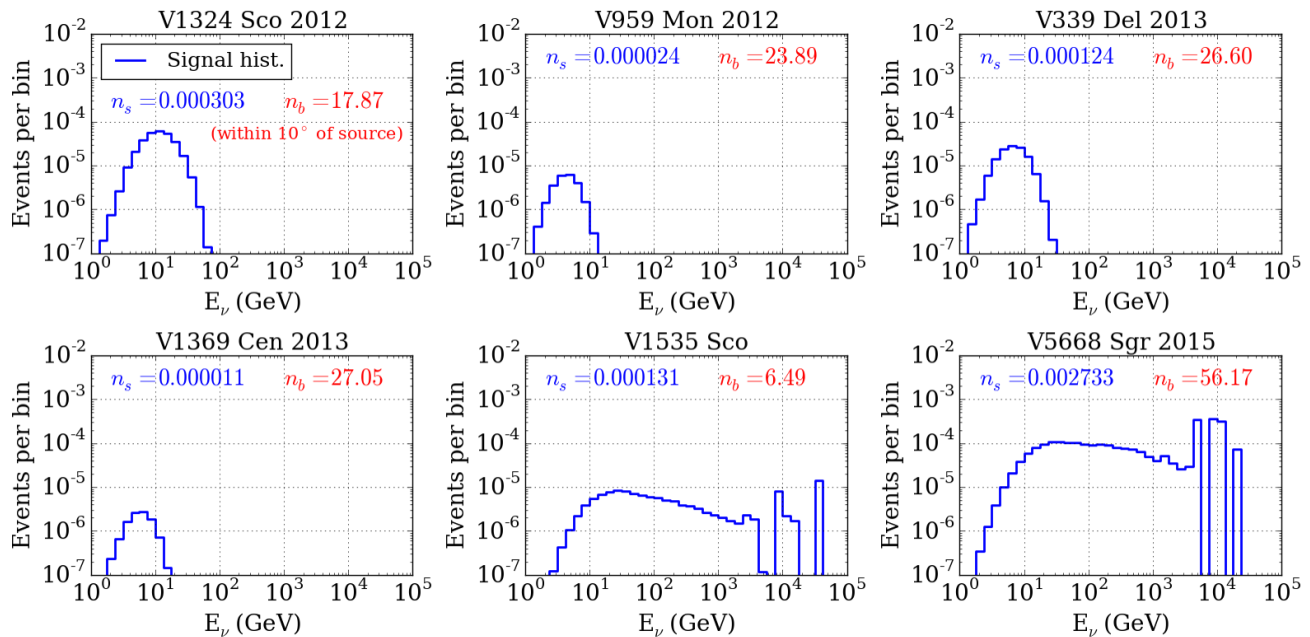
Figure 7-10: Estimates of local (within 10° of source) background and signal inferred from gamma-ray detections by *Fermi* for six novae concurrent with the GRECO event sample. I use the gamma-ray spectra from [101] as estimates for the neutrino flux. Background is given as the estimated number of events within 10° of the source in its livetime (Table 7.1)

For Monte Carlo simulation, some issues seen in the effective area are yet to be resolved. The first issue is maintaining smooth effective area transitions between simulation energy regimes (Genie to "low-energy" NuGen, then to "medium-energy" NuGen). This requires recording the number of simulation files used, the number of generated events per file, and the ratio of neutrinos to anti-neutrinos generated. In the currently available simulation dataset, we believe one or more of these numbers is wrong for at least one subset. The second issue is that statistics are very low for neutrino simulation above 20 TeV. A remedy could be processing more medium-energy simulation for GRECO, or if only *Fermi* cut-off spectra are used for spectral model tests, statistical fluctuations at 20 TeV and above would have negligible effect on analysis results.

7.3.2   Model-dependent likelihood

To test the hypothesis that gamma rays and neutrinos follow the same light curve and energy spectrum, *Fermi* data will need to be used to create temporal and spectral signal PDFs for event-

wise likelihood. Then analysis software will need to take these PDFs into account when calculating the test statistic. The latter of these tasks would be most easily implemented in the SkyLab software framework.

For example, the signal PDF used in the test statistic will become

$$S_i = S_x(\overrightarrow{x_i}, \sigma_i; \ \overrightarrow{x_{src}}, \sigma_{src}) \cdot S_t(t_i; \ \Phi_{src}(t)) \cdot S_E(E_i; \ \Phi_{src}(E)) \tag{7.4}$$

where S_x is the usual spatial correlation PDF, S_t is a PDF describing the *Fermi*-detected gamma-ray light curve (with some truncation to zero at the edges), and S_E weights the estimated energy of the IceCube event according to the gamma-ray spectrum.

Appendix A

Topocentric Corrections
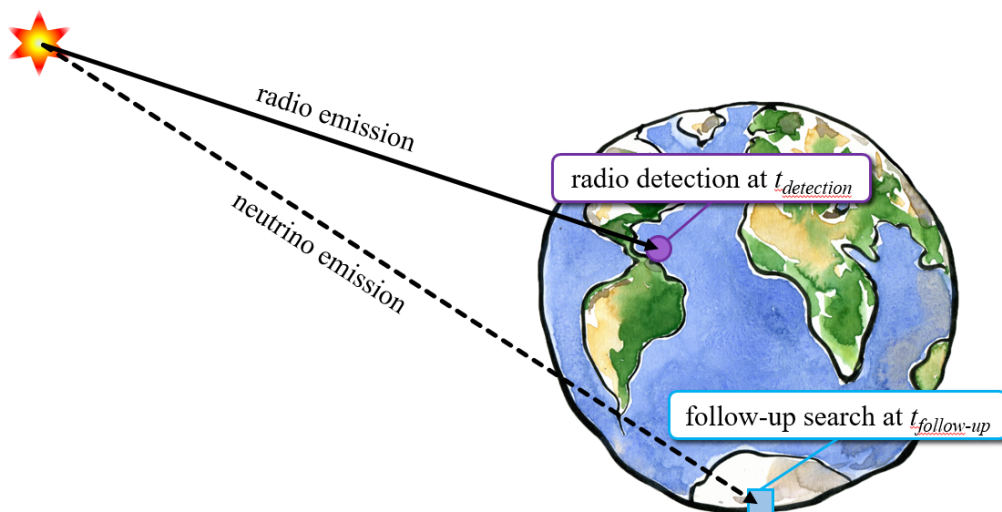
Figure A-1: For short transients ($\Delta T < 1$s), a follow-up search for radio-simultaneous neutrino emission must account for the difference between the radio-transit time to the radio observatory and to IceCube. We call the adjustment of $t_{detection}$ into IceCube's time-frame ($t_{follow-up}$) a *topocentric correction.*

Consider an instantaneous astronomical event occurring at $Dec = +90°$ at time t (reported in UTC) by a hypothetical radio observatory at the North Pole ($lat. = +90°$). If we are interested in searching for coincident signal neutrino emission from this source, and we choose a signal on-time window on the order of milliseconds, we must correct the time of our on-time window for the additional transit time of neutrinos from the North Pole to IceCube. In this example, our on-

time window should be centered at $t + 42\ ms$ – this is the light-transit time of Earth's diameter (neutrinos travel at practically $v = c$ in this energy range).

For sources and observatories that don't form a syzygy[1] with IceCube, the adjustment – called a *topocentric correction* – to IceCube's expected time of neutrino detection is more complicated. Let an FRB be detected at time t with $(RA,\ Dec)_{FRB}$ by a radio observatory with coordinates $(lat.,\ long.)_{Obs}$. Using *PyEphem*, we can find the astronomical coordinates to which the observatory's zenith points at time t: $(RA,\ Dec)_{Obs}$. Multiplying these coordinates by the observatory's distance from Earth's center – $R_{\oplus}$ is a sufficient approximation – gives its coordinates relative to Earth's center.

$$\vec{\alpha} = f((lat.,\ lon.)_{Obs.};\ t_{FRB}) = R_{\oplus} * (RA,\ Dec)_{Obs.} \qquad (A.1)$$

Likewise, we find $(RA,\ Dec)_{IceCube}$ from $(lat.,\ long.)_{IceCube}$.

$$\vec{\beta} = f((lat.,\ lon.)_{IceCube};\ t_{FRB}) = R_{\oplus} * (RA,\ Dec)_{IceCube} \qquad (A.2)$$

The projection of $\vec{\alpha}$ onto $(RA,\ Dec)_{FRB}$ (via dot product) gives the difference in distances for FRB signal to the observatory and to the Earth's center. The difference in projections of $\vec{\alpha}$ and $\vec{\beta}$ onto $(RA,\ Dec)_{FRB}$ is the distance between observatories along the signal's line of transit. This distance divided by c gives the topocentric correction time.

$$\Delta t = \frac{1}{c} \left[\vec{\alpha} \cdot (RA,\ Dec)_{FRB} - \vec{\beta} \cdot (RA,\ Dec)_{FRB} \right] \qquad (A.3)$$

For example, the topocentric correction for the first detection of FRB 121102 by the Arecibo Observatory is $\Delta t = +32$ ms. FRB 121102 lies at $Dec = +33.1°$, and Arecibo lies on the Earth

---

[1] i.e., when the three locations don't form a straight line in space

at $lat. = +18.3°$; for this detection of FRB 121102, its location on the sky at detection time t is separated only $15.8°$ from the Arecibo's zenith. Topocentric corrections for FRB 121102 from Arecibo to IceCube range from $+24$ ms to $+32$ ms.

For reference, the minimum absolute correction among all FRBs (as of July 2017) is for FRB 110627 with $\Delta t = -3$ ms. The maximum absolute correction for which IceCube would expect an earlier signal in UTC is – predictably, because of the source's proximity to the celestial South Pole – FRB 121002 at $Dec = -85.2°$ with $\Delta t = -9$ ms.

A.1   Topocentric Correction Code

```python
#!/usr/bin/env python
import ephem, math, sys
import numpy as np
from datetime import datetime

def observer( longitude, latitude, elevation ):
    obs = ephem.Observer()
    obs.lon = longitude # expects radians (East+/West-)
    obs.lat = latitude # expects radians (North+/South-)
    obs.elevation = elevation # height above sea level in meters
    return obs

def sources( ra, dec, time ):
    if not hasattr(ra, '__len__'): ra = [ra]
    if not hasattr(dec, '__len__'): dec = [dec]
    if type(time) == type(datetime(2010,1,1,0,0,0)): time = [time]
    else:
        print "Error: sources() input 'time' must be a datetime object."
        sys.exit()
    if not len(ra) == len(dec) and len(ra) == len(time):
        print "Error: numbers of source parameters are inconsistent!"
        sys.exit()

    src = {['ra']  : np.array(ra, dtype=float)
           ['dec']: np.array(dec, dtype=float)
           ['t']   : np.array(time, dtype=datetime)}
    return src

def topocentric_correction( detector_obs, followup_obs, sources ):
    """ Return time adjustment for signal transit at follow-up observatory
    :type    detector_obs: ephem.Observer()
    :param   detector_obs: observatory which detected the sources

    :type    followup_obs: ephem.Observer()
    :param   followup_obs: observatory performing follow-up (IceCube)

    :type    detector_obs: sources() object, defined above
    :param   detector_obs: sources (e.g. FRBs) detected by detector_obs
    """
```

```python
        time_diffs = np.zeros(len(sources['ra']))
        for j in range(len(sources['ra'])):
            ra = sources['ra'][j]
            dec = sources['dec'][j]
            t = sources['t'][j]

            detector_obs.date = ephem.Date(t)
            followup_obs.date = ephem.Date(t)

            detector_separation = ephem.separation( detector_obs.radec_of(0., np.pi/2),
        [ra, dec] )
            followup_separation = ephem.separation( followup_obs.radec_of(0., np.pi/2),
        [ra, dec] )

            detector_core_transit = (detector_obs.elevation + 6.317e6) * math.cos(
        detector_separation )
            followup_core_transit = (followup_obs.elevation + 6.317e6) * math.cos(
        followup_separation )

            time_diff = ( detector_core_transit - followup_core_transit ) / 3.e8
            time_diffs[j] = time_diff

        return time_diffs
```

Appendix B

Transient Test Statistic

A test statistic is a single value assigned to an analysis result that is designed to evaluate the likelihood of an observation under separate physics hypotheses. It is typical to define the background, or *null*, hypothesis as the case that none of the observed events are the result of emissions from the source(s) in question. The most simple alternative hypothesis is that n_s signal events in the data were the result of emission from the source(s), however variants may include statements regarding source-wise flux, energy spectrum, or flavor composition, to name a few. The simple signal case is a sufficient generalization for this section.

B.1 Likelihood Construction

The test statistic (TS) is defined as follows:

$$TS := \ln \frac{\mathscr{L}_s(N, \{x_i\}; n_s + n_b)}{\mathscr{L}_0(N, \{x_i\}; n_b)} \tag{B.1}$$

where $\mathscr{L}_s$ is the observed data's likelihood under a signal hypothesis – that n_s signal events were observed from the sources in the test – and $\mathscr{L}_0$ is the background hypothesis where $n_s = 0$.

$$\mathscr{L}(N, \{x_i\}; n_s + n_b) = P_{Poisson}(N; n_s + n_b) \prod_{events} P(x_i) \tag{B.2}$$

$$P(x_i) = \frac{n_s S_i + n_b B_i}{n_s + n_b} \tag{B.3}$$

The transient likelihood $\mathscr{L}$ has two components. The first is a Poisson probability: the probability that in the analyzed data, with $n_s + n_b$ events expected, N are observed (Eq. B.2). This is fundamentally the difference between transient analyses and steady-source analyses, and it results in a larger signal likelihood of spatially coincident events when the expected number of background events is smaller. The second likelihood component represents the product of probabilities of observing each individual event with properties x_i (e.g. $zenith_i$, $azimuth_i$, $energy_i$, etc.). In Eq. B.3, this probability $P(x_i)$ for event i can be considered in two parts: 1. What is the probability that, assuming N is comprised of n_s signal events and n_b background events, this event is signal or background?; 2. given this event's identity as signal or not, what is the likelihood of this event having such properties derived from background parameterization (B_i) or from assumptions of signal emission (S_i)?

In model-independent analyses, B_i is simply the directional component of the background PDF evaluated at x_i's zenith for x_i's data channel (i.e., its year if cuts change year-to-year, or its event filter if multiple are searched). Figure B-1 shows the background PDF for Level2-pass2 MuonFilter data as an example. In an energy-independent, temporally binned analysis, the background likelihood B_i of each event is the value of this PDF at the event's reconstructed direction. This is equivalent to assuming each event PDF is a Dirac delta function, properly multiplying the background PDF and event PDF, and integrating over the sky. For well reconstructed events and/or a background PDF which is nicely monotonic in zenith angle, this assumption is valid.

For the record, the mathematically robust – but prohibitively computationally expensive – method

Level2-pass2 background PDF (zenith only)

Equatorial

0.02 B_i (sr^{-1})   0.2
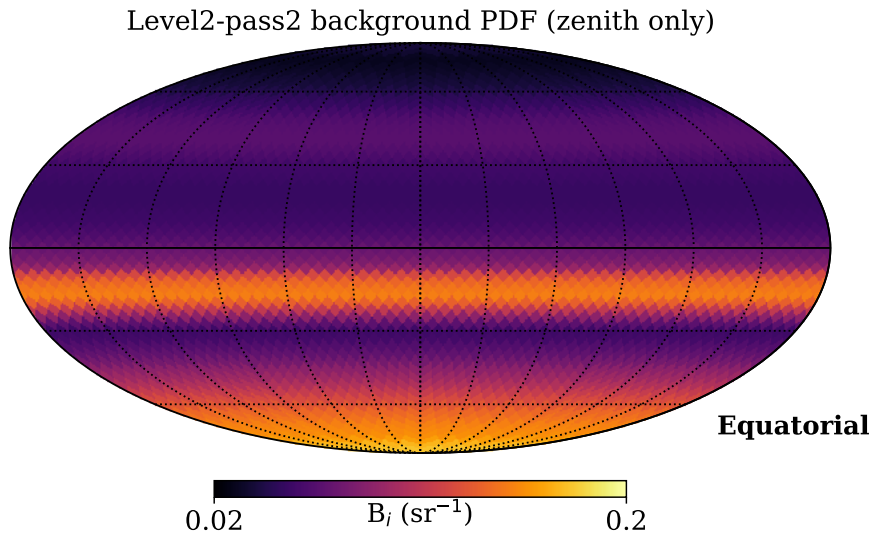
Figure B-1: The background PDF for Level2-pass2 data, parameterized only in zenith angle for simplicity. The value of B_i for an event in the likelihood is assigned according to its location on this sky map. The PDF integrates to 1 over the sky (4π sr).

of calculating B_i is to multiply the whole event PDF with the background PDF and integrate the product over the whole sky. A qualitative example is shown in Figure B-2.

S_i is roughly the height of the event's point spread function (PDF) – approximated as a two-dimensional gaussian radially symmetric on the celestial sphere with standard deviation σ – evaluated at the location of the source whose time-window with which it coincides. More generally, S_i is the renormalized sum of signal PDFs for J_i sources whose on-times contain the event (Eq. B.4). Since our analysis doesn't encounter overlapping on-time windows, there hasn't yet been a need to implement the true S_i, but in general,

$$S_i = \frac{\sum_j^{sources} S_{ij}\delta_{t_i,\Delta T}w_j}{\sum_j^{sources} \delta_{t_i,\Delta T}w_j} \tag{B.4}$$

Each S_{ij} is given a per-source weight of w_j, which for simplicity we've set to unity for all sources. As an example, a more sophisticated analysis could weight each source by its radio fluence. Another factor $\delta_{t_i,\Delta T}$ is added so that only on-time sources contribute to S_i and its normalization. In this
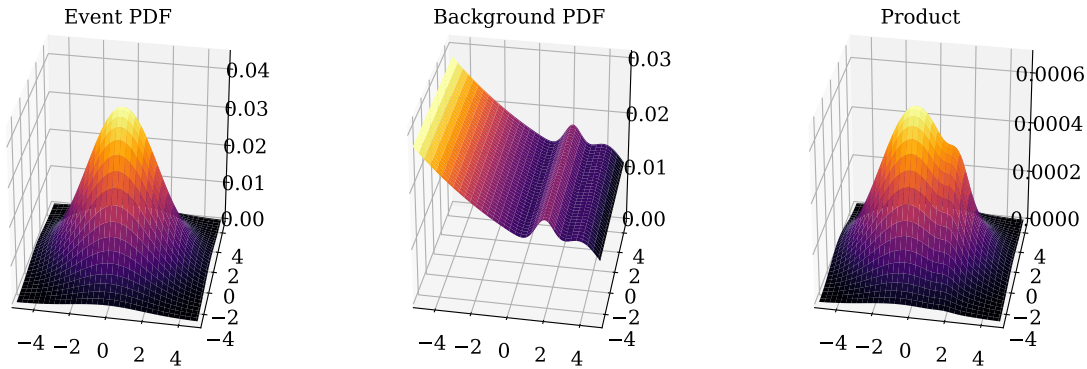
Figure B-2: The product of an arbitrary event PDF with the background PDF in dimensionless Cartesian coordinates. The integral of this product – which has dimensions sr^{-2} – over all space is the true value of B_i, but because of computational limitations, the event PDF is approximated as a Dirac delta function. Therefore in practice, B_i is equivalent to the value of the background PDF at the direction of event i.

analysis, $\delta_{t_i, \Delta T}$ is equal to 1 for one and only one source per event. In the steady source limit (ΔT contains the entire data sample), where all $\delta = 1$, our test statistic becomes that of a point source search, as expected.

As with B_i, the mathematically robust method of calculating S_i is prohibitively time-consuming. Ideally, the event PDF and source PDF would be multiplied, making no assumptions about the shapes of the two distributions. The integral of the product over the sky is S_i, equal to the sum at all points in 4π of the probability that event i originated from (θ, ϕ) and that the source exists at (θ, ϕ) (see Figure B-3). Since the product of two Gaussians is a Gaussian, for well localized sources (e.g., $\sigma_{src} \ll 1°$) and symmetrical Gaussian event PDFs, we often simplify the calculation of S_i to be the height of a 2-D symmetrical Gaussian with $\sigma^2 = \sigma_i{}^2 + \sigma_{src}{}^2$ at a distance $\Delta\Psi$ from the mean (Section B.2). This assumption is valid in the regime where the projection of the PDFs onto the sphere is negligible; in practice, this criterion is $(10°)^2 > \sigma_i{}^2 + \sigma_{src}{}^2$.

B.2 Exercise I: evaluation of signal PDFs

In this exercise I justify the statement made above: when evaluating the signal PDF for an event and source each with a radially symmetric Gaussian distribution and centers separated by $\Delta\Psi$, it
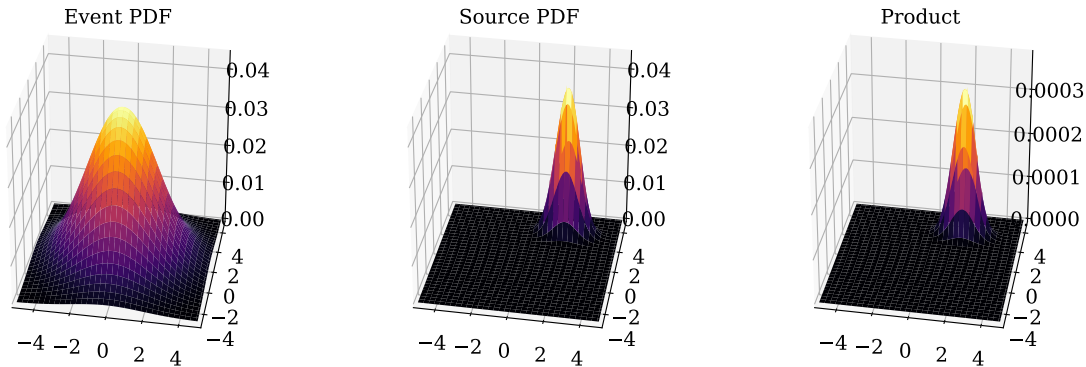
Figure B-3: The product of an event PDF with a source PDF. The integral of the product over all space is the proper value of S_i, but because of computational limitations, both distributions are assumed to be symmetrical 2-D Gaussians, and therefore their product is itself a 2-D Gaussian. In practice, S_i is height of this Gaussian at a distance $\Delta\Psi$ from the mean, where $\Delta\Psi$ is the angular separation between the centers of the event PDF and source PDF.

is sufficient to calculate the height of a distribution with $\sigma^2 = \sigma_i^2 + \sigma_{src}^2$ at a distance $\Delta\Psi$ from the mean.

First, assume a source with directional uncertainty σ_{src} and a coincident event with direction and uncertainty (RA_i, Dec_i) and σ_i. For simplicity, we also consider treatment of the signal PDF for source and event with relatively narrow directional uncertainty, $(10°)^2 > \sigma_i^2 + \sigma_{src}^2$. In this regime, we may use a Cartesian projection of the coordinates as a decent approximation, so let's center our coordinate system on the source and call the event direction (x_i, y_i).

The PDF describing the location of the source is given by

$$P_{src}(x, y) = \frac{1}{2\pi\sigma_{src}^2} \, \exp\left(\frac{-x^2}{2\sigma_{src}^2} + \frac{-y^2}{2\sigma_{src}^2}\right) \tag{B.5}$$

and for the direction of the event,

$$P_i(x, y) = \frac{1}{2\pi\sigma_i^2} \, \exp\left(\frac{-(x - x_i)^2}{2\sigma_i^2} + \frac{-(y - y_i)^2}{2\sigma_i^2}\right) \tag{B.6}$$

Multiplying these two, we have the probability density at each point (x, y) that the source and

event are spatially coincident.

$$P_{S_i}(x, y) = \frac{1}{2\pi\sigma_{src}^2} \frac{1}{2\pi\sigma_i^2} \exp\left(\frac{-x^2}{2\sigma_{src}^2} + \frac{-y^2}{2\sigma_{src}^2} + \frac{-(x - x_i)^2}{2\sigma_i^2} + \frac{-(y - y_i)^2}{2\sigma_i^2}\right) \tag{B.7}$$

Then integrate P_{S_i} over all (x, y), adding the probabilities of spatial coincidence at each point in space, and simplify.

$$
\begin{aligned}
S_i &= \int\limits_{all\ space} P_{S_i}(x, y)\ dx\ dy \\
&= \frac{1}{4\pi^2\sigma_{src}^2\sigma_i^2} \exp\left(\frac{-x_i^2 - y_i^2}{2\sigma_i^2}\right) \int \exp\left(\frac{-x^2}{2\sigma_{src}^2} - \frac{x^2 - 2x_i x}{2\sigma_i^2}\right) dx \int \exp\left(\frac{-y^2}{2\sigma_{src}^2} - \frac{y^2 - 2y_i y}{2\sigma_i^2}\right) dy \\
&= \frac{1}{4\pi^2\sigma_{src}^2\sigma_i^2} \exp\left(\frac{-x_i^2 - y_i^2}{2\sigma_i^2}\right) \frac{\pi}{\frac{1}{2\sigma_{src}^2} + \frac{1}{2\sigma_i^2}} \exp\left(\frac{x_i^2 + y_i^2}{4\sigma_i^4(\frac{1}{2\sigma_{src}^2} + \frac{1}{2\sigma_i^2})}\right) \\
&= \frac{1}{2\pi(\sigma_{src}^2 + \sigma_i^2)} \exp\left(\frac{-\Delta\Psi_{S_i}^2}{2(\sigma_{src}^2 + \sigma_i^2)}\right)
\end{aligned}
\tag{B.8}
$$

For poorly localized events and sources, we instead use the Kent distribution: a probability distribution on the unit sphere S^2. As $\sigma \to \infty$, the Kent distribution returns a uniform probability distribution, and as $\sigma \to 0$, it returns the Dirac delta function.

B.3 Exercise II: limiting case of Poissonian test statistic

In this exercise I show the relationship between the standard point-source test statistic and the Poissonian test statistic used in transient analyses.

Typically in an IceCube steady-source analysis – i.e., no timing information is used – an event sample containing at least 100,000 events is studied for correlation, and the vast majority are known to be unassociated with the source of interest. Still, it is possible for one or more events to contribute significant spatial correlation and for a discovery to be made. The steady-source

likelihood is defined as

$$\mathcal{L}_{Steady} = \prod_{i=1}^{N} \frac{n_s S_i}{N} + \left(1 - \frac{n_s}{N}\right) B_i \tag{B.9}$$

$$TS_{Steady} = \sum_{i=1}^{N} \ln\left(1 + \frac{n_s}{N}\left(\frac{S_i}{B_i} - 1\right)\right) \tag{B.10}$$

In a transient analysis, the event sample considered for correlation is drastically reduced in time based on some physically motivated signal hypothesis. This can result in an on-time event sample expected to contain fewer than one event (e.g., for $\Delta T < 1$ s in the six-year FRB analysis). In these cases, a more powerful likelihood can weight spatially coincident events by an additional factor inversely proportional to the expected number of background events in the on-time. This is accomplished with a Poisson probability in the likelihood.

$$\mathcal{L}_{Transient} = \frac{(n_s + \langle n_b \rangle)^N e^{-(n_s + \langle n_b \rangle)}}{N!} \prod_{i=1}^{N} \frac{n_s S_i + \langle n_b \rangle B_i}{n_s + \langle n_b \rangle} \tag{B.11}$$

$$TS_{Transient} = -n_s + \sum_{i=1}^{N} \ln\left(1 + \frac{n_s S_i}{\langle n_b \rangle B_i}\right) \tag{B.12}$$

In the steady-source limit, $n_s \ll N$ and $n_b/N \approx 1$, therefore

$$\begin{aligned}
TS_{Transient} &= -n_s + \sum_{i=1}^{N} \ln\left(1 + \frac{n_s S_i}{\langle n_b \rangle B_i}\right) \\
&= \sum_{i=1}^{N} \ln\left(1 + \frac{n_s S_i}{\langle n_b \rangle B_i}\right) - \frac{n_s}{N} \\
&\approx \sum_{i=1}^{N} \ln\left(1 + \frac{n_s S_i}{\langle n_b \rangle B_i}\right) + \ln\left(1 - \frac{n_s}{N}\right) \\
&\approx \sum_{i=1}^{N} \ln\left(1 + \frac{n_s S_i}{\langle n_b \rangle B_i} - \frac{n_s}{N}\right) = TS_{Steady}
\end{aligned} \tag{B.13}$$

Appendix C

Muon Filter Azimuthal Asymmetry

In Chapter 6, I show that the distribution of Level 2 MuonFilter events has an unexplained large-scale variation in azimuth (Figure 6-2). This section addresses the possible causes that have been investigated.
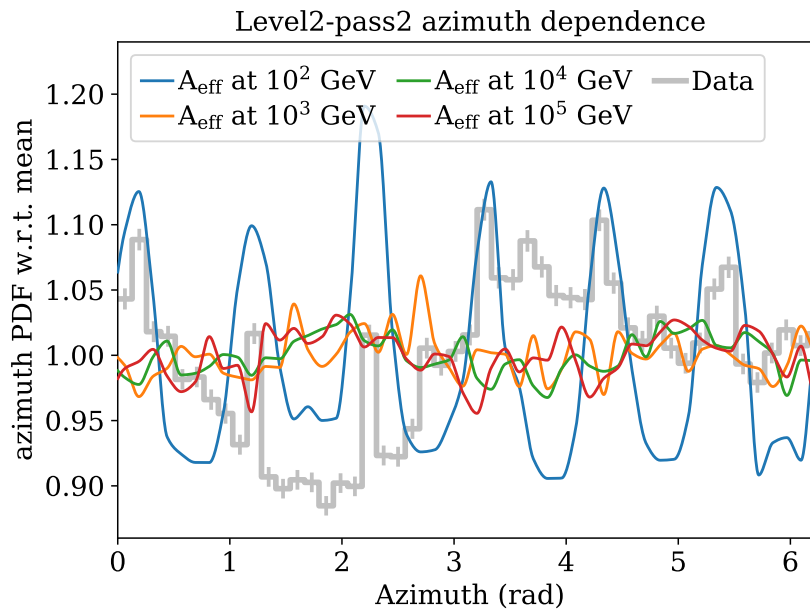
Figure C-1: The azimuthal dependence of ν_μ effective area (i.e., using true neutrino azimuth) at a range of energies does not show the large-scale structure seen in data (gray). Peaks at 10^2 GeV (blue) and at the same azimuth values in the data histogram correspond to string alignment in the detector.
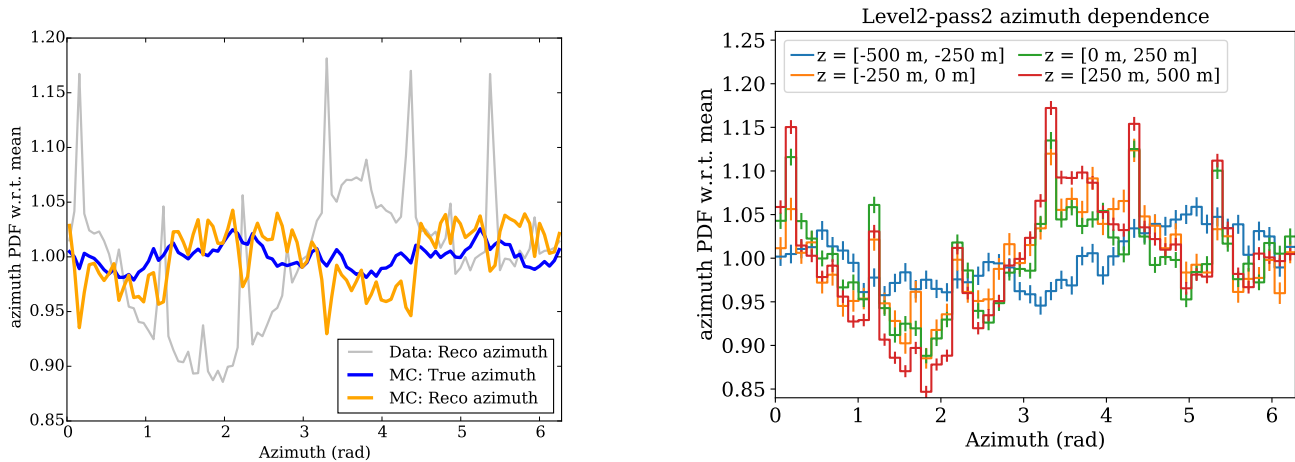
Figure C-2: Left: Simulated neutrino events are generated uniformly in azimuth and do not show the asymmetry in PDFs of either true or reconstructed azimuth. The sinusoidal shape with peaks at 2 rad and 5 rad is expected from the modeled ice anisotropy. **Right:** The azimuthal PDF is split by the height (z) of the best-fit interaction vertex; this assumes every muon is produced by a neutrino interaction in the ice, which is the case as the event sample is dominated by atmospheric muons. Still, this tells us that the anisotropy is greatest among events that enter nearer to the top of the detector.

Figure C-1 shows a check for this feature in Level 2 neutrino simulation data. At energies $\sim 10^2$ GeV, the effective area has peaks as expected at string alignments in IceCube's hexagonal detector grid. At higher energies, these peaks disappear and show a faint two-period sine wave due to ice anisotropy[1]. However, the overall variation in data (gray) is not seen in simulation (Figure C-2).

Figure C-3 splits the azimuth distribution into rows by zenith. Here we see that the feature is contributed to most by events with reconstructed zenith angles at or below the horizon. Since the Level-2 rate at these zenith angles is much higher than the expected rate of atmospheric neutrinos (roughly 0.01 Hz), events in this region are mostly misreconstructed down-going muons. As follow-up work, the error in zenith angle and azimuth on atmospheric muons in this region should be quantified by looking into simulated muon data (using tools like MuonGun and Corsika).

In the southern sky and close to the North Pole, Figure C-3 has six dark purple azimuth values

---

[1]Inhomogeneity in the orientation of ice crystals in the Antarctic ice result in a directional asymmetry of the mean-free path of Cherenkov light. Consequently, events traveling parallel or anti-parallel to this asymmetry are more likely to trigger the detector, causing two peaks in the azimuth distribution [108]. The measured effect is in phase with the sine shape of higher-energy effective areas in Figure C-1 because it is implemented in the IceCube detector simulation. (https://icecube.wisc.edu/ musner/docs/analysis/04_ice_model_systematic/index.html)
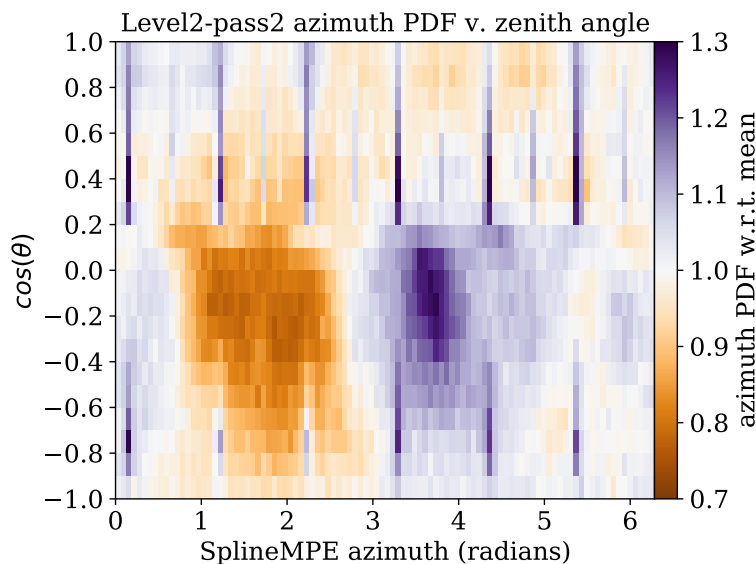
Figure C-3: The azimuthal PDF is split into reconstructed zenith bands (rows) and row-normalized. The average pixel value across a row is 1, with relative excesses in purple and deficits in orange. The azimuth values of six vertical lines of excess correspond to the alignment of nearest neighboring strings in the detector, and faint vertical lines between them correspond to alignment of next-nearest neighbors. Events with reconstructed zenith angles in the horizon and northern sky reveal a large-scale asymmetry with an amplitude of 30%. Seven days of IceCube Level-2 MuonFilter data is shown here total, from runs representing all twelve months and from seven years of IceCube's 86-string configuration: roughly 22 million events.

corresponding to the azimuthal orientation of nearest neighbor strings in the detector. Between those azimuth angles, six softer excesses can be seen in the southern sky which correspond to alignment of muon tracks with next-nearest neighbor strings. There is no obvious geometric explanation for the dominant large-scale asymmetry in event azimuth at the horizon.

Next, I translated the feature into polar coordinates to better visualize it from IceCube's reference frame. Taking data from $90° < \theta < 135°$, I projected event directions onto their respective geographical coordinates in the southern hemisphere ($lat. < 0°$). Figure C-4 shows how some simple geometric rules lead to the conversion from zenith to latitude.

$$-lat. = 90° - (180° - 2(180° - \theta))$$

$$180° - (90° - lat.)/2 = \theta$$
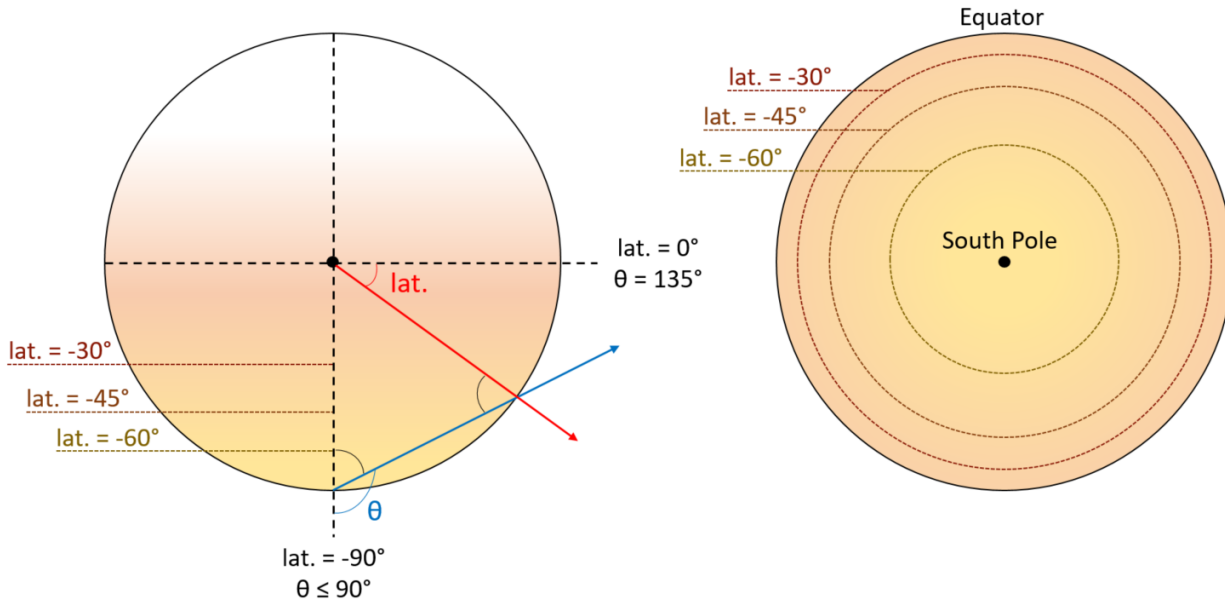
Figure C-4: Left, side view: the relationship between latitude and zenith is demonstrated for latitudes in the southern hemisphere. **Right, polar view**: the Earth as viewed from above the South Pole. Only the southern hemisphere is visible; geographic areas become more distorted towards the equator. This is the viewing scheme for subsequent polar plots in this chapter.

Detector azimuth is defined so that the conversion to longitude satisfies $az. = 0°$ at $long. = 90°$ W and $az. = 90°$ at $long. = 0°$.

In Figure C-5 I draw the great circle passing through both the geomagnetic pole[2] and IceCube to approximate the magnetic field direction at the South Pole. For reference, Figure C-6 shows the detector grid with the same orientation – the sine feature in azimuthal data does not have any clear correlation to grid orientation. Interestingly, the magnetic field line appears to bisect the azimuthal asymmetry.

C.1   The Problem with Magnetism

Earth's magnetic dipole is nearly anti-parallel to its rotational poles; that is, the magnetic pole near the South Pole is actually a magnetic North, so the field lines are directed northward. A proton with a downward trajectory will, via the Lorentz force ($q\mathbf{v} \times \mathbf{B}$, *contorts right hand*), deflect

---

[2]Pole locations taken from http://www.geomag.bgs.ac.uk/education/poles.html
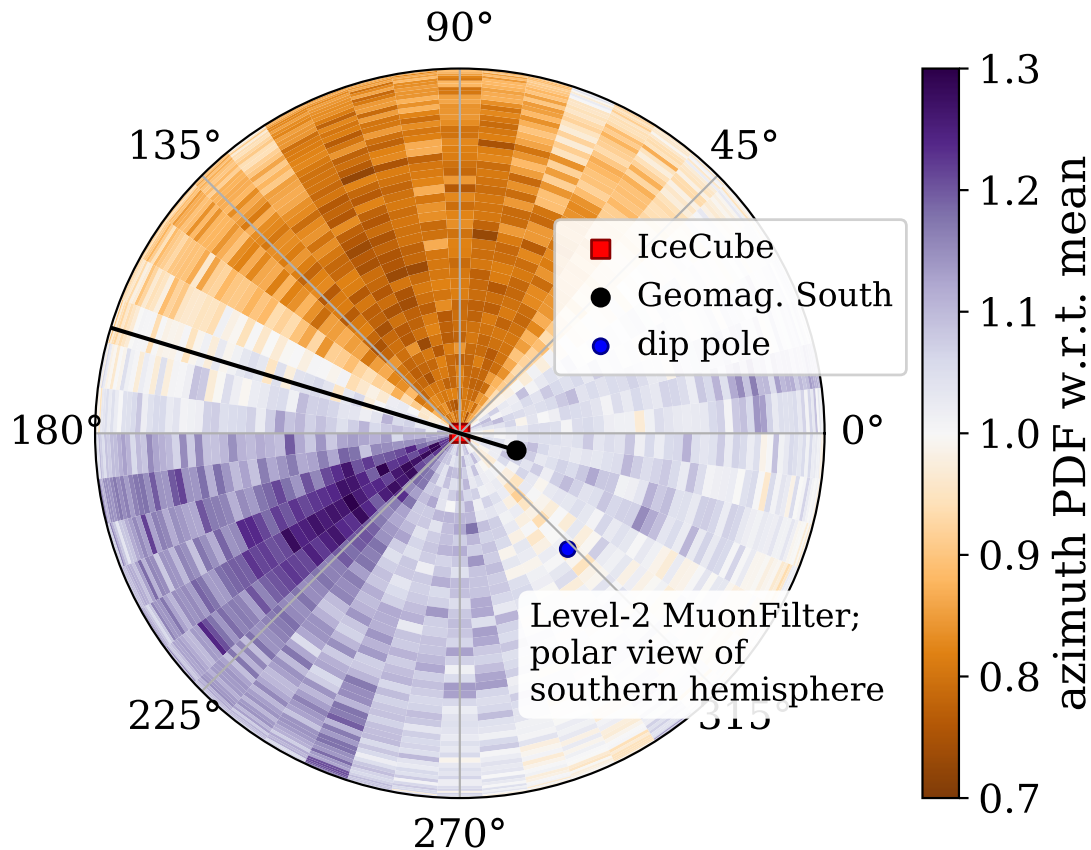
Figure C-5: A view of the azimuthal effect in geographical coordinates from above the South Pole. The southern magnetic dipole and dip pole – where the magnetic field direction is perpendicular to Earth's surface – are shown to estimate the local magnetic field direction at the South Pole. Data is again normalized in zenith bins of equal solid angle, which correspond to concentric rings in the polar view. Here, since the inferred geographical coordinates of each event direction's intersection with Earth's surface are used, only data with reconstructed zenith angle in the range $90° < \theta < 135°$ is shown. Because this is a very loose event selection, I do not imply that these are truly up-going events: they must be almost entirely misreconstructed atmospheric muons, but this alone does not explain the cause of the asymmetry.
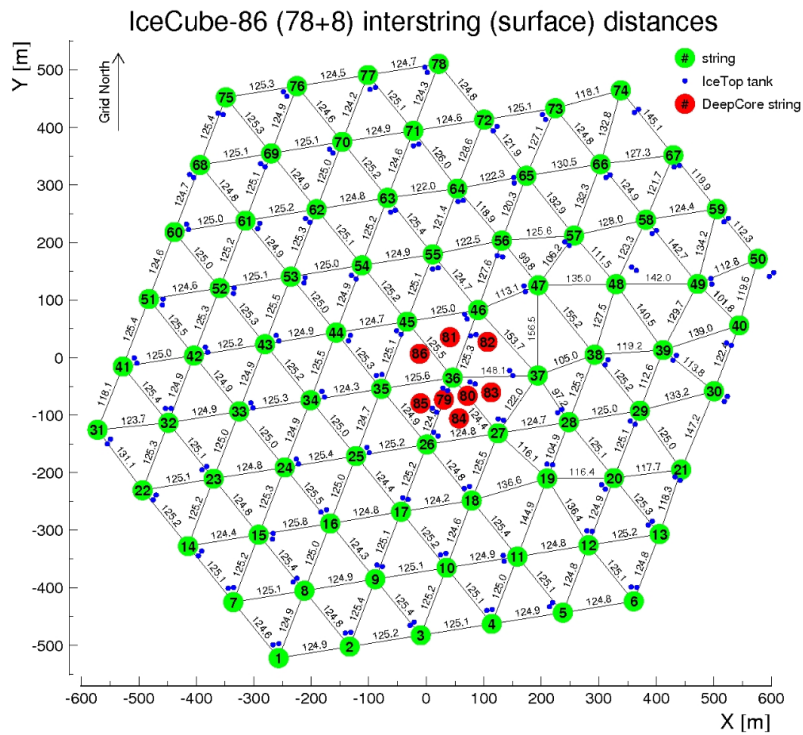
Figure C-6: The orientation of the IceCube detector grid is shown from above, with $az. = 0°$ pointing right and increasing counter-clockwise.

towards the East. For cosmic ray detectors, this results in an excess of events when observing westward and a deficit when observing eastward. The data are so far consistent with an East-West hypothesis for the cause of the large-scale asymmetry.

Furthermore, since the deflection of a particle by the Lorentz force is inversely proportional to its energy, the effect should be larger for lower-energy events. Figure C-7 shows that this is indeed the case, using an energy estimator MuEX in lieu of a direct per-event energy prediction. As a rule of thumb, atmospheric muons with energies less than 300 GeV are physically incapable of penetrating IceCube's glacial overburden due to ionizing losses[3]; therefore, even the lowest-energy muon tracks here are caused by relativistic muons with $\gamma > 1000$.

---

[3]The minimum rate of ionizing energy loss for a muon in ice is $(dE/dx)_{min} \approx 200$ MeV m$^{-1} \rightarrow 300$ GeV/1.5km
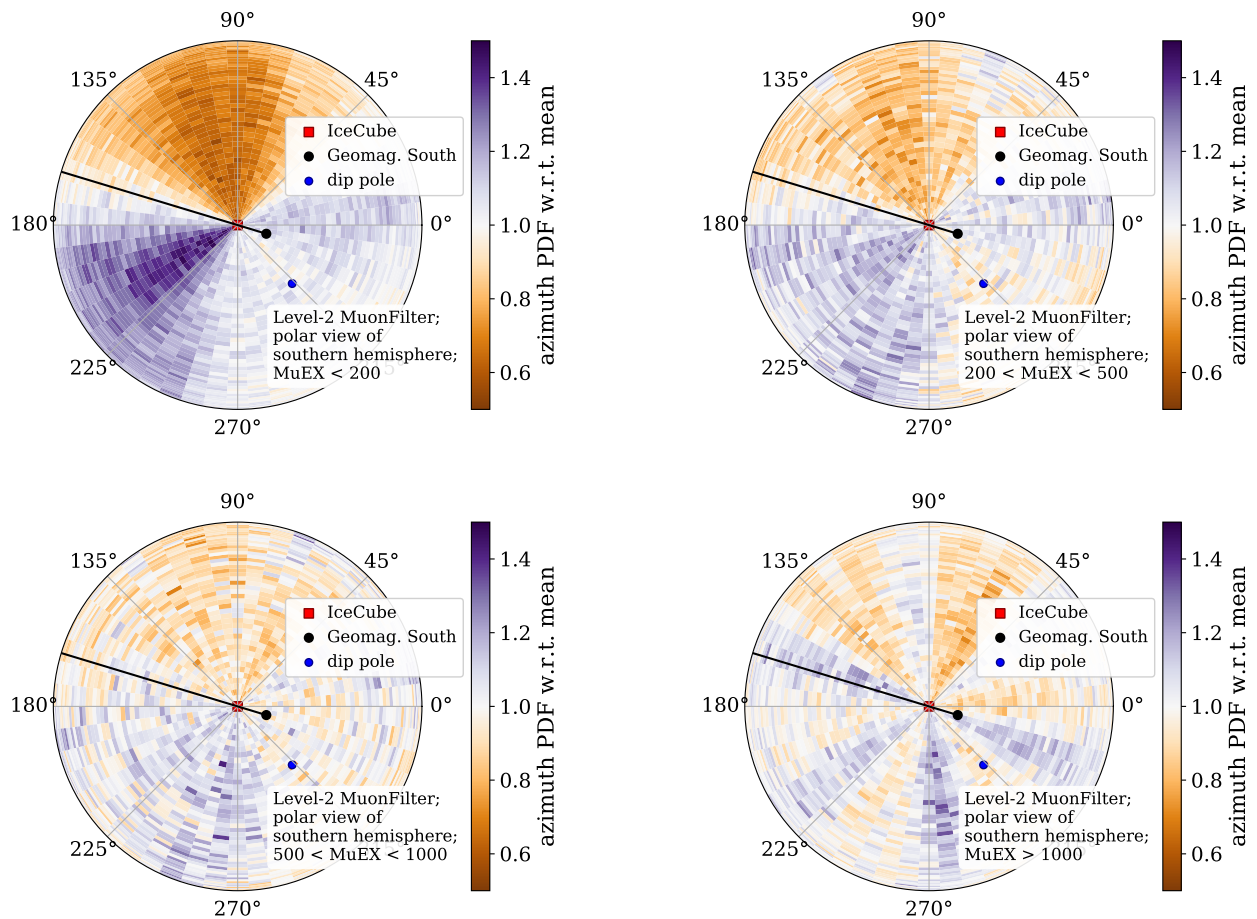
Figure C-7: The azimuthal distribution is shown for increasing values of the unitless energy estimator MuEX: **Top left**: $MuEX < 200$; **Top right**: $200 < MuEX < 500$; **Bottom left**: $500 < MuEX < 1000$; **Bottom right**: $MuEX > 1000$. Each plot has more than 2.5 million events, and each pixel has statistical error less than 5%. Since Level-2 MuonFilter has roughly one billion events per year, these plots could still be made after significant cuts, and subtle asymmetry could still be seen over statistical variations.

For a relativistic muon in a magnetic field, the gyroradius is given by

$$R = \frac{\gamma m v_\perp}{qB} \tag{C.1}$$

$$\approx 3.35 \left(\frac{E}{\text{GeV}}\right) \frac{1}{B} \ \text{m} \tag{C.2}$$

The rest mass of a muon is 105 MeV/c^2, so this equation is valid for muons with energy greater than roughly 1 GeV. At 1 GeV, a muon in a magnetic field of $B = 60$ μT has a gyroradius of about 56 km (using an estimate of $\mathbf{B}$ in Antarctica from some geomagnetic maps); at 100 GeV, R is on the order of Earth's radius. This seems to rule out the effects of Earth's magnetic field on muons themselves after creation in the atmosphere.

The East-West effect in cosmic ray primaries is also diminished at higher energies. Since the products of pion decay are detected at energies an order of magnitude below that of their cosmic ray primary (Section 2.3), the energy above which the East-West effect becomes smaller than 5% in muons and neutrinos is only a few GeV [109]. This seems to disfavor magnetic deflection from being detected by IceCube, so the cause of the azimuthal asymmetry remains unknown.

As a next step, simulated atmospheric events ought to be analyzed for magnetic effects and to quantify the zenith and azimuth components of the angular error on events reconstructed as up-going. Cuts can be made on Level-2 MuonFilter to isolate events that most resemble atmospheric muons; perhaps the asymmetry originates mainly from either the remaining events or from those removed. Additionally, low-energy event selections have been made which look for astrophysical neutrinos in DeepCore. Since the background in these event samples should be largely atmospheric neutrinos, any magnetic effects on the order of 1% or more should be visible with several years of data.
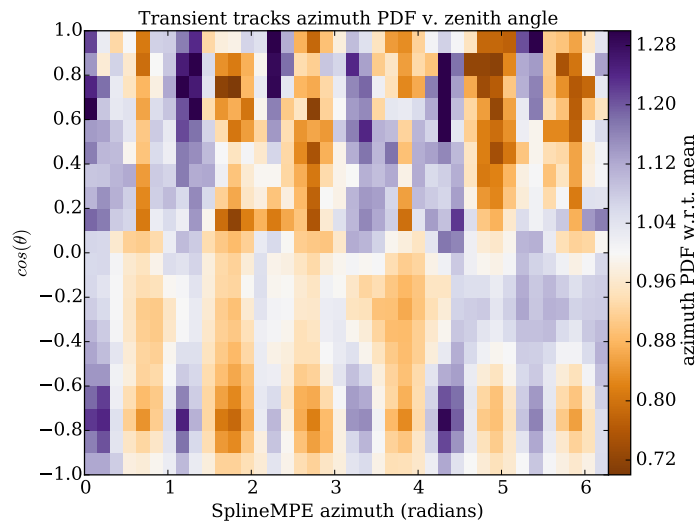
Figure C-8: The azimuthal PDF in normalized zenith angle bins is shown for the data from the six-year FRB analysis. Statistical errors are apparent here, where rows at $cos(\theta) > 0.6$ have fewer than one thousand events. The disappearance of the major asymmetry here suggests that it is caused by down-going atmospheric muons as suspected. However, at $0.1 < cos(\theta) < 0.6$, there might still be the asymmetry in the same azimuth regions: a deficit around 2 radians and an excess around 4 radians.

Appendix D

HitSpoolWriter

This chapter discusses a project I started with Benedikt Riedel and Chris Weaver in the summer of 2014. By 2016, the project had stalled significantly and has since not been seriously revisited. There is still interest in its construction among IceCube members, so the following is meant to serve as documentation for someone picking up where we left off.

D.1 Motivation

During event simulation, real physical aspects of the detector are ignored or approximated for simplicity. Simulated particles travel through the detector, generating simulated photons which propagate to the DOMs, creating simulated digital waveforms which are sent up cables to the surface to determine event triggers. A project called `TriggerSim` simulates the behavior of the physical data acquisition system (pDAQ) at South Pole Station, but its performance under extreme or unusual physics circumstances may not duplicate reality. If, for example, a nearby supernova generated a glut of neutrinos in IceCube, the pDAQ could become overloaded with hits and lose some or all of the data. A tool that can simulate these events and test the real pDAQ response would diagnose these issues before potential major discoveries are squandered. The code that reads DOM hits at the South Pole is called `HitSpoolReader`; therefore this project, which aims to
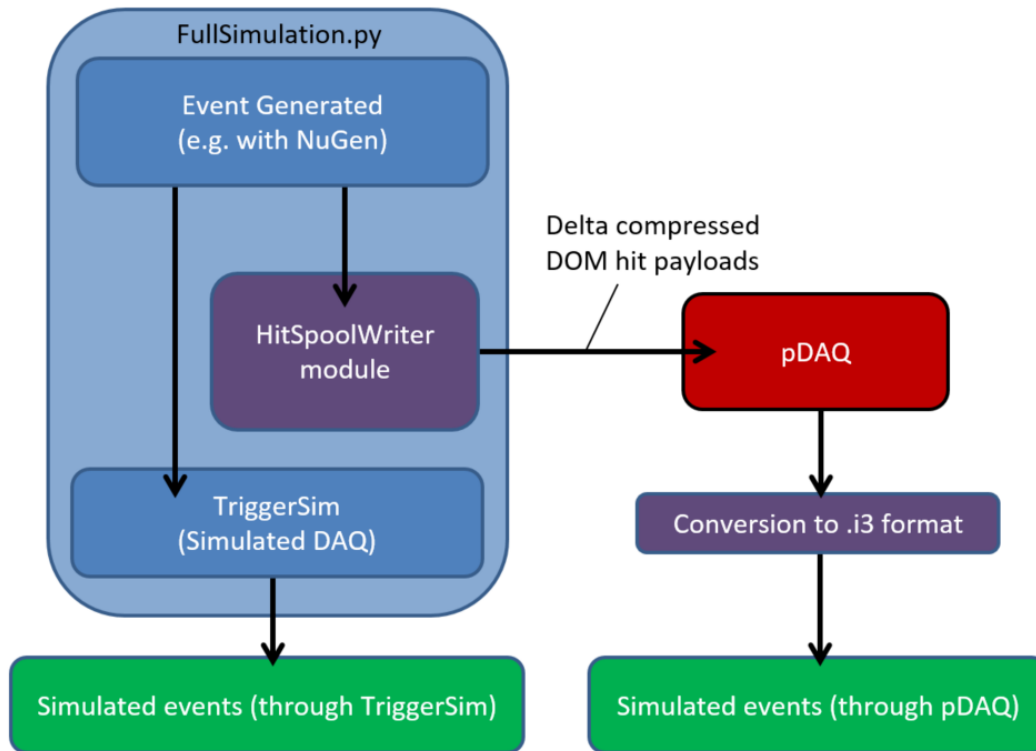
Figure D-1: Overview of HitSpoolWriter project. The HitSpoolWriter module is callable in `FullSimulation.py` and outputs payloads that can be processed by the pDAQ. The pDAQ output is converted into the standard `.i3` event file format and compared to the TriggerSim output.

re-write simulated DOM hits into the hitspool format read by pDAQ is named `HitSpoolWriter`.

D.2   Summary of Work

HitSpoolWriter is under development in IceCube's code sandbox[1]. The module is callable in `FullSimulation.py` with three added parameters: like `-o` to name the output `.i3` file, `-O` names the output hit spool; the event start time and time between events are specified with `-T` and `-t` respectively.

First, hits must be resorted. In simulation, hits are sorted in a dictionary by OMKey (the DOM ID) then launch time. The pDAQ receives lists of time-ordered hits from each string hub. To match reality, hits are resorted by their string then launch time using the DomLaunchSeriesMap and EventHeader objects.

[1] https://code.icecube.wisc.edu/projects/icecube/browser/IceCube/sandbox/sfahey/HitSpoolWriter?order=name
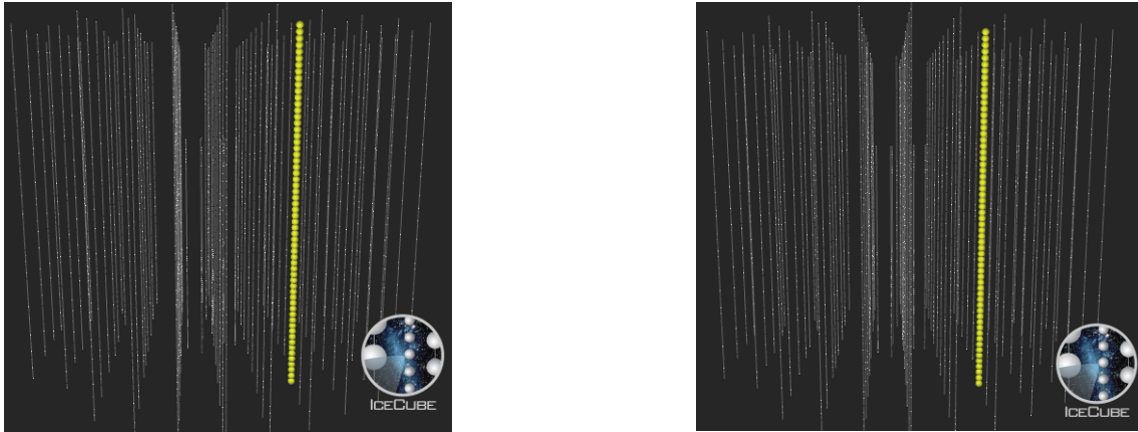
Figure D-2: Left: a TriggerSim frame from simulation of photo-electrons in each DOM on String 43. **Right**: a pDAQ frame of the same test. Qualitatively, the results show that HitSpoolWriter can correctly write hit spools for pDAQ processing.

Second, the hits are written to a binary file using the Delta Compressed DOM Hit payload format[2]. After conversion to binary, a byte-swap function is required. The pDAQ reads data in a big-endian format, meaning it interprets information so that the final digit holds the highest place value; this is the opposite from our traditional little-endian view of data with place value decreasing to the right.

D.2.1   Test 1: light up one string

As an initial test, I ran `FullSimulation.py` with a function that simulated one photo-electron in each DOM on String 43[3]. The HitSpoolWriter module was used and Dave Glowacki processed its output in pDAQ, returning a DAT file that could be converted into `.i3`. The data simulated this string-lighting event at 200 Hz for 10 minutes.

Figure D-2 shows the identical output events from TriggerSim and pDAQ. However, aside from this resemblance, there are some discrepancies between the two outputs.

The TriggerSim output has 120,000 frames as expected. Approximately half have durations of 20 μs, and the rest have durations around 26 μs to 28 μs. Only in the latter group, some DOMs

---

[2]See "Type 3" in https://wiki.icecube.wisc.edu/index.php/Payloads. Additional information on Word1, Word3, and other header information can be found there.

[3]See CreateMCPEs function in /IceCube/sandbox/sfahey/HitSpoolWriter/resources/scripts/fullSimulation.py.

on String 43 report two hits; this set of DOMs is unique to each frame. By contrast, the pDAQ output has 119,560 frames (99.6% of input), of which $\sim$1% have a 20 μs duration and the rest 27 μs to 33 μs. A small number of frames had durations larger than 10 ms due to the slow particle trigger. Many pDAQ frames had a set of DOMs reporting two hits, and for corresponding frames where both outputs had double-hit DOMs, the unique sets of DOMs matched the other output exactly.

D.2.2   Test 2: light one string and add noise

The next test was to repeat the simulation of photo-electrons on String 43 with random noise added via the Vuvuzela module. Figure D-3 shows the outputs which are intended to be identical, but the noise hits are not properly being converted or read by pDAQ.
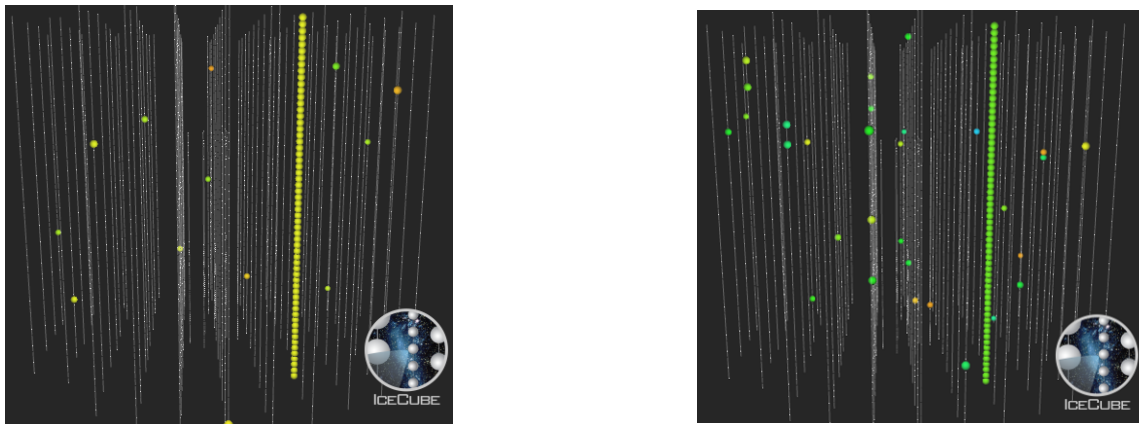
Figure D-3: Left: a TriggerSim frame with noise hits randomly added. **Right**: a pDAQ frame of the same test. The hit spool is written after the noise hits are generated, so we would expect the two frames to appear identical, but they do not. No correlation of noise is found between any two TriggerSim and pDAQ frames.

D.3   Future Work

The cause of discrepancy between TriggerSim and pDAQ in the noise case remains unsolved. As a first step, I recommend selectively disabling triggers in both TriggerSim and pDAQ and repeating the previous tests; it may be that one or more triggers is causing problems with the proper reading of hit times. For example, the SLOP trigger appeared to be causing dropped frames in its 10 ms

trigger window.

Once ordinary simulation events can reliably be duplicated by pDAQ, there are many interesting test cases to consider for improvement of pDAQ triggers: an increased rate in SLC hits as a test for SNDAQ; coincident track events to test recognition of separate muons in the detector; and extremely high-energy events to test detector performance during large data readouts.

Appendix E

Paper: FRB Search with Public Data Release

This appendix contains the published versions of papers for analyses to which I made significant contributions. The first paper, corresponding to Chapter 4 in this thesis, is "A Search for Neutrinos from Fast Radio Bursts with IceCube". It was published in *The Astrophysical Journal* on 8 August 2017 [75].

Using one year of data from an IceCube point-source search, this analysis placed the earliest limits on neutrino emission from FRBs in a binned search for four FRB sources.

A SEARCH FOR NEUTRINOS FROM FAST RADIO BURSTS WITH ICECUBE

Samuel Fahey, Ali Kheirandish, Justin Vandenbroucke[1], and Donglian Xu
Wisconsin IceCube Particle Astrophysics Center and Department of Physics,
University of Wisconsin, Madison, WI 53706, USA
Draft version August 11, 2017

ABSTRACT

We present a search for neutrinos in coincidence in time and direction with four fast radio bursts (FRBs) detected by the Parkes and Green Bank radio telescopes during the first year of operation of the complete IceCube Neutrino Observatory (May 2011 through May 2012). The neutrino sample consists of 138,322 muon neutrino candidate events, which are dominated by atmospheric neutrinos and atmospheric muons but also contain an astrophysical neutrino component. Considering only neutrinos detected on the same day as each FRB, zero IceCube events were found to be compatible with the FRB directions within the estimated 99% error radius of the neutrino directions. Based on the non-detection, we present the first upper limits on the neutrino fluence from fast radio bursts.

Subject headings: neutrinos — radiation mechanisms: non-thermal

1. INTRODUCTION

Fast radio bursts (FRBs) are a new class of astrophysical radio transients of very short (few millisecond) duration. The first was discovered in a 2007 analysis of archival data from the Parkes telescope (Lorimer et al. 2007). A total of 23 unique burst directions have now been detected by five different telescopes (Parkes, Arecibo, Green Bank, UTMOST, and ASKAP; Petroff et al. (2016)). One (and only one) of these directions has been found to repeat, producing at least 17 bursts at different times (Spitler et al. 2016; Scholz et al. 2016). The first claimed host identification and redshift (Keane et al. 2016) for an FRB was later shown to be an active galactic nucleus (Williams & Berger 2016). However, after precise localization of the repeating burst by the VLA, an optical host galaxy was found (Chatterjee et al. 2017), and its redshift was determined to be 0.19 (Tendulkar et al. 2017). Given their rate of detection by radio surveys performed with relatively low exposure time and field of view, the rate of FRBs across the full (4π) sky is estimated to be several thousand per day (Champion et al. 2016), about 10% of the core-collapse supernova rate (Murase et al. 2016).

The origin and emission mechanism of these bursts is unknown. Models have proliferated and include the birth of black holes from supramassive neutron stars (Falcke, H. & Rezzolla, L. 2014) and giant flares from magnetars (Pen & Connor 2015). Their large dispersion measures indicate an extragalactic origin, but they could also originate in Galactic sources enshrouded in dense plasma (Loeb et al. 2014). Only one burst has been proven to repeat, and the same burst is the only one proven to be extragalactic. While the repetition rules out a cataclysmic model for that source, other bursts could be produced in cataclysmic scenarios. While leptonic emission is the default assumption in most models, hadronic emission mechanisms or association with hadronic emission regions are also possible, with implications for cosmic rays and neutrino emission (Li et al. 2014).

A 15-50 keV gamma-ray transient of ∼300 s duration, coincident with FRB 131104 with a statistical significance of ∼3 sigma, was reported by DeLaunay et al. (2016). No other afterglow or counterpart has been detected. If this is a genuine counterpart, the gamma-ray fluence is ∼6 orders of magnitude greater than the radio fluence, raising the energy budget for modeling the emission and for additional counterparts.

In addition to energy budget considerations, there are two additional constraints in modeling neutrino emission from FRBs: (1) the neutrino emission region must be dense enough in target matter or radiation to produce neutrinos, but not dense enough to absorb radio emission if it is produced in the same region; (2) it is difficult to cool hadrons quickly and thereby produce neutrino emission on short time scales. Nevertheless, target radiation fields and baryons are expected in the environment surrounding many possible FRB progenitors (Murase et al. 2016).

Because of their very short duration, prompt counterparts are most likely to be detected either by coordinated observation campaigns or serendipitously, in the latter case most likely by wide-field instruments. Because there is still so little known about the nature of fast radio bursts, it is essential to perform model-independent searches using a variety of wide-field instruments spanning multiple wavelengths and messengers.

IceCube is a cubic-kilometer neutrino detector located at the geographic South Pole. It consists of an array of 5160 digital optical modules encompassing a gigaton of ice as the active volume (IceCube Collaboration 2017a). With sensitivity to all neutrino flavors over the full sky including both hemispheres, the IceCube detector enables a wide range of science (IceCube Collaboration 2006).

IceCube has discovered a diffuse astrophysical neutrino flux between several TeV and several PeV (IceCube Collaboration 2013a,b, 2014a, 2015a,b,c, 2016a). Many of the neutrino events originate far from the Galactic plane and are therefore likely to be extragalactic. Although the diffuse flux is detected with high statistical significance in multiple distinct detection channels, no evidence for dis-

[1] justin.vandenbroucke@wisc.edu

2

crete sources has been found, either in searches for clustering of the neutrinos or in cross-correlation with catalogs of source candidates (IceCube Collaboration 2014b). The origin of the astrophysical neutrinos remains unknown. The majority of the astrophysical flux is not produced by gamma-ray bursts (IceCube Collaboration 2012, 2015d, 2017b) or star-forming galaxies (Bechtol et al. 2017).

2. NEUTRINO SAMPLE

The event sample used in this analysis is part of a multi-year data set optimized to search for point sources of astrophysical neutrinos. The event selection is described in detail in IceCube Collaboration (2014b). The first year of events and accompanying details (including the effective area of the event selection as a function of energy and declination) were recently released (IceCube Collaboration 2016b). For each event, the data release includes the time of the event truncated to integer Modified Julian Day (MJD), the best-fit energy and direction, and an estimate of the direction uncertainty (50% containment radius).

The data set includes a total of 138,322 events from 333 days of livetime spanning May 2011 to May 2012 (MJD 55694 through 56062), with a roughly equal number of events from the northern and southern hemispheres. The data reduction and event reconstruction procedures are detailed in IceCube Collaboration (2014b). Events with declination greater than $-5°$ are considered "up-going" (northern hemisphere) events and are predominantly atmospheric neutrinos. "Down-going" (southern hemisphere) events reconstructed to originate from declination less than $-5°$ are dominated by cosmic-ray-induced atmospheric muons and high-energy muon bundles (multiple muons produced in the same extensive air shower).
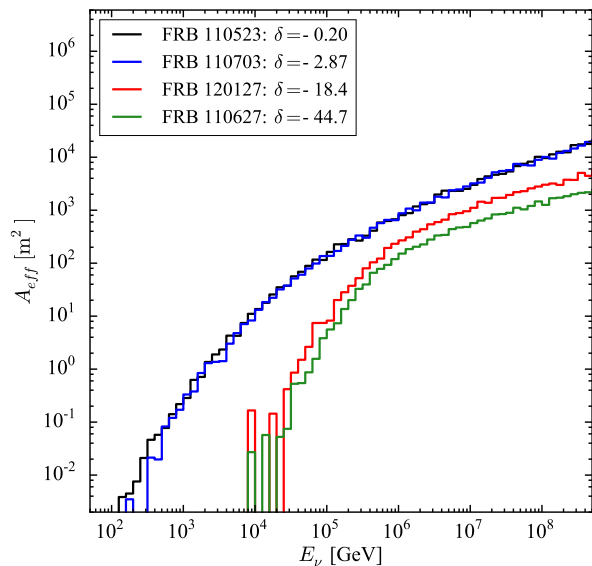
As discussed in IceCube Collaboration (2014b), the event selection was performed separately for the northern and southern hemispheres with boosted decision trees. In the up-going region, the ice and the Earth act as a shield for atmospheric muons, so a high-purity neutrino sample with a wide energy range and low energy threshold is obtained. In the down-going region, high-energy neutrinos are also retained, but a high-purity neutrino sample cannot be as easily achieved due to the atmospheric muons. In order to bring the atmospheric muon contamination under control, a higher energy threshold was applied in the southern sky.

Figure 1 shows the muon neutrino effective area of the IceCube event selection as a function of energy in the direction of each FRB. At every energy the effective area is smaller in the southern sky than near the celestial equator due to the tight cuts necessary to reduce the cosmic-ray muon background in the southern sky. In the southern sky, fluctuations are visible in the effective area curves near the energy threshold (~20 TeV), likely due to statistical fluctuations in the Monte Carlo used to calculate the curves.

The rate of detected events in the sample varies from day to day due to natural causes such as seasonal variation in the production of atmosphere neutrinos and muons (Tilav et al. 2010) and due to detector effects such as downtime. We estimated the size of possible downtime effects from the number of IceCube events detected on the day of each FRB. The event counts are (in time order of FRB occurrence) 423, 395, 342, and 465. Because the event count on each day is within ~20% of the average count per day in the full sample (375), detector deadtime was likely not substantial on any of the FRB days.

Figure 2 shows the event rate in this sample as a function of declination, averaged over right ascension and time during the year. Because of the higher energy

Figure 1. Neutrino effective area as a function of energy for the event selection used in this analysis, in the direction of each FRB. The declination δ of each FRB is given (in degrees) in the legend. The effective area in the southern sky is less than that near the celestial equator due to tighter cuts used to reduce the atmospheric muon background in the southern sky.

Figure 2. Event rate in the IceCube data sample as a function of declination, averaged over right ascension within each declination band. The declination of each FRB is shown for reference. The rate is normalized per calendar day between MJD 55694 and 56062 (369 days), not per day of livetime.

threshold applied in the southern hemisphere to counteract the high atmospheric muon rate, the event rate varies by only a factor of ∼2 acros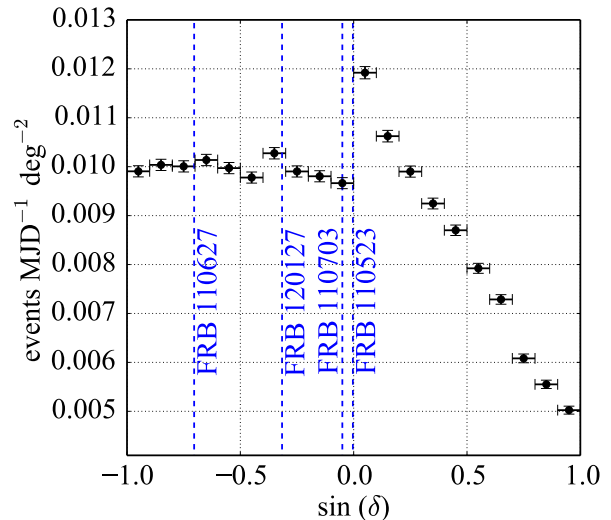s the sky. The average rate is 0.009 events per square degree (roughly the area of the point-spread function) per day. Detection of a single event compatible with the direction of an FRB and detected on the same day as the FRB would therefore be interesting.
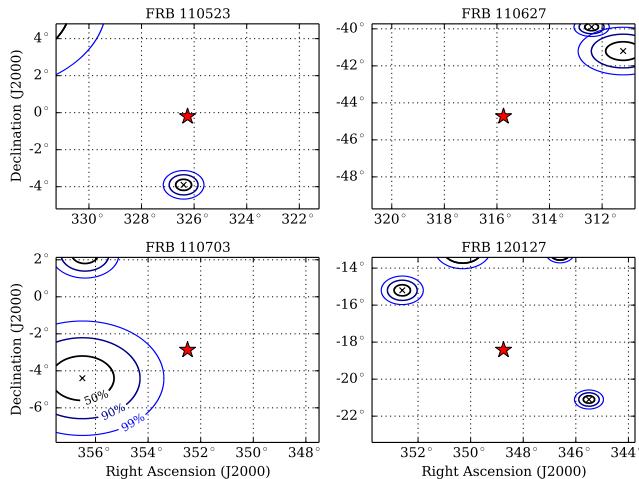
3. COINCIDENCE SEARCH

Figure 3. The region of interest centered on each FRB (⋆) in this sample is shown in equatorial coordinates in Cartesian projection. The best-fit direction of each IceCube event is indicated with an ×. The 50%-containment circle for each event is shown, as is an estimate of the 90%- and 99%-containment circles under the approximation that the point spread function is a radially symmetric two-dimensional Gaussian distribution.

Four FRBs have been detected in the year spanned by this IceCube event sample: FRB 110523 (Masui et al. 2015), FRB 110627, FRB 110703, and FRB 120127 (Thornton et al. 2013). Two are near the celestial equator and two are well south of it. Because the IceCube event times are truncated to integer MJD, temporal coincidence with these FRBs can only be tested on the one-day time scale. For each FRB, the radio burst detection time was truncated to integer MJD and the angular distance to each IceCube event on the same day was calculated. The localization error of each FRB is ∼0.2° or better (Thornton et al. 2013; Masui et al. 2015), negligible in this analysis.

We assume for this search that the point-spread function for each event can be approximated by a radially symmetric two-dimensional Gaussian. Under this assumption, the radius of the 90% and 99% error circles can be determined from the 50% error circle by multiplying by a factor of 1.82 and 2.58, respectively. Figure 3 shows these error circles for coincident (on the same truncated MJD as the FRB) events near each of the FRBs. The nearest (relative to its error circle) coincident event is separated by 4.27° from FRB 110703 on MJD 55745, with a 50% angular error of 1.2°.

4. RESULTS AND CONCLUSION

Because there is no IceCube event consistent with the time and direction of any of the four FRBs analyzed,
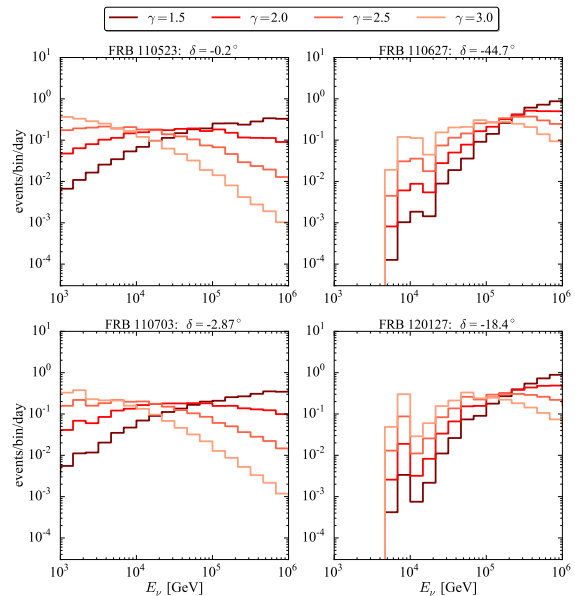
Figure 4. Energy distribution of events that would be detected if the neutrino flux saturated our upper limits. Each curve is determined by multiplying the power-law spectral model by the detector effective area and normalizing so that the integral is 2.3 events (the 90% confidence level upper limit on the event rate given that zero events were detected). Several power law indices (γ) were tested.

we proceed to constrain the neutrino emission associated with each burst. Using the Poisson distribution, we construct a 90% confidence level upper limit on the neutrino fluence by finding the fluence that would produce on average 2.3 detected neutrinos.

The expected number of muon neutrinos detected from a source at zenith angle θ is

$$N_{\nu_\mu + \overline{\nu}_\mu} = \int \phi(E_\nu)\, A_{eff}(E_\nu, \theta)\, dE_\nu\, dt, \qquad (1)$$

where $\phi(E_\nu)$ is the neutrino flux at earth and A_{eff} is the IceCube effective area as a function of neutrino energy and zenith angle. We used the effective area corresponding to the event selection and selected $A_{eff}(E_\nu)$ for each FRB based on its declination (Figure 1). In order to constrain the neutrino flux, we assume the flux to be a power law given by

$$\phi(E_\nu) = \phi_0 \Big(\frac{E_\nu}{E_0}\Big)^{-\gamma}. \qquad (2)$$

We set the normalization energy, E_0, to 100 TeV and consider four different spectral indices ranging from 1.5 to 3. To calculate the expected number of events we perform the integral in Equation 1 from 1 TeV to 1 PeV in neutrino energy.

Figure 4 shows for each burst the distribution of event energies that IceCube would detect for various power-law neutrino spectra. The shape of each curve is determined by multiplying the flux by the effective area, and each curve is normalized to 2.3 total events, i.e. to the 90% confidence level upper limit on the expected number of events detected from the burst. As the figure shows,

4

the tightest limits arise from the FRBs found near the celestial equator. This is a result of IceCube's effective area peaking in this direction.

For the two bursts well south of the celestial equator, the effective area curves at these declinations have large fluctuations near ∼10 TeV, likely due to statistical uncertainty close to the energy threshold in the Monte Carlo used to determine the effective area. This is the cause of the fluctuations seen at ∼10 TeV in the right two panels of Figure 4.
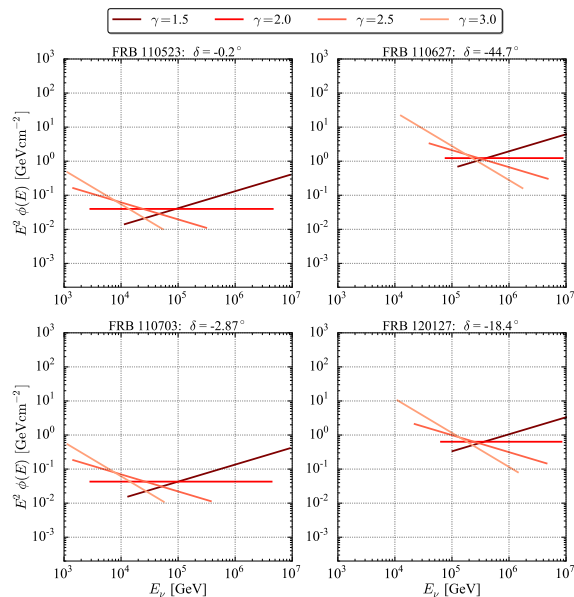

Figure 5. Upper limits (90% confidence level) on the time-integrated neutrino flux from each FRB, assuming a power-law neutrino spectrum with index γ. Each upper limit is drawn over the energy range that contains the central 90% of events that would be detected (the central 90% of the distribution shown in Figure 4), i.e. the core energy range within which the analysis is sensitive for each burst and spectral model.

Figure 5 shows the corresponding time-integrated flux upper limits for several assumed spectral models for each FRB.

The neutrino fluence (time-integrated energy flux) is

$$f = \int_{E_{min}}^{E_{max}} E\,\phi(E)\,dE\,dt, \qquad (3)$$

where $E_{min} = 1$ TeV and $E_{max} = 1$ PeV. Table 1 shows the neutrino fluence upper limit for each burst for $\gamma = 2.0$.

In the future, a more sensitive search can be performed for high-energy neutrinos from these and additional FRBs both by analyzing subsequent years of Ice-Cube data and by using a looser event selection with greater effective area and greater background rate but on shorter time scales (extending from the one-day scale studied here over a range of scales all the way down to the intrinsic ∼10 ms FRB duration), similar to the strategy used for gamma-ray-burst neutrino searches (Ice-Cube Collaboration 2012, 2015d, 2017b). Furthermore, an IceCube search for lower-energy (MeV scale) neutrinos can be performed using an analysis strategy similar to that used for nearby supernovae (IceCube Collaboration 2011).

Using a complementary approach to derive an upper limit on the neutrino fluence per average FRB, we divide the all-sky diffuse neutrino flux by the all-sky FRB rate. The result is shown in Figure 6 and yields a more stringent upper limit than the per-burst analysis. Note that these two sets of upper limits test different hypotheses. The per-burst analysis tests whether there is significant neutrino emission from any particular burst, while the calculation using the diffuse neutrino flux treats all FRBs as a single homogeneous population. That is, if all FRBs across the sky (several thousand per day, the vast majority of which are not radio detected) were to produce a neutrino fluence saturating our per-burst upper limits, then they would produce a total diffuse astrophysical neutrino flux greater than that measured by IceCube.

Additional FRB observations are needed to determine whether there are sub-classes (e.g. repeating and non-repeating, or extragalactic and Galactic) of FRBs. Based on other astrophysical transients such as supernovae and gamma-ray bursts, sub-classes would not be surprising. The discovery of FRB sub-classes would bridge the gap between the two approaches by enabling searches for neutrino emission from individual sub-classes each with a lower rate than the total. It may be possible in the future to detect neutrino emission from a particular sub-class of FRBs.

In the absence of FRB sub-classes, stacking many FRBs in the future will enable even tighter constraints than those derived from the diffuse astrophysical neutrino flux. Interferometric arrays expected to begin operation in 2017 could detect 30 or more FRBs per day, or ∼10^4 per year (Rajwade & Lorimer 2017). For short time windows approaching the radio emission duration (∼10 ms), an IceCube search stacking as many as 10^4 to 10^5 bursts will have a total background expectation of 10^{-4} to 10^{-3} events, and the constraints will become tighter than those derived directly from the diffuse neutrino flux.

Detection of a neutrino FRB signal in this analysis would have indicated a hadronic process, providing a strong constraint on FRB origins and emission mechanisms. It would have also constituted the first evidence for a high-energy astrophysical neutrino source. In the absence of a detection, we have calculated upper limits on each burst as well as a comparison to the total diffuse astrophysical neutrino flux. The expected onslaught of FRB detections in the near future will enable sensitive searches for neutrino emission by stacking thousands of bursts. We encourage theoretical work to provide quantitative predictions that can be tested by these searches.

Table 1
Characteristics of each fast radio burst (right ascension, declination, time, radio fluence, and telescope) and of the nearest IceCube event detected on that day (angular distance from FRB, error radius). The final column gives the 90% confidence level upper limit on the neutrino fluence from the burst assuming the neutrino spectrum is a power law with index 2.0.

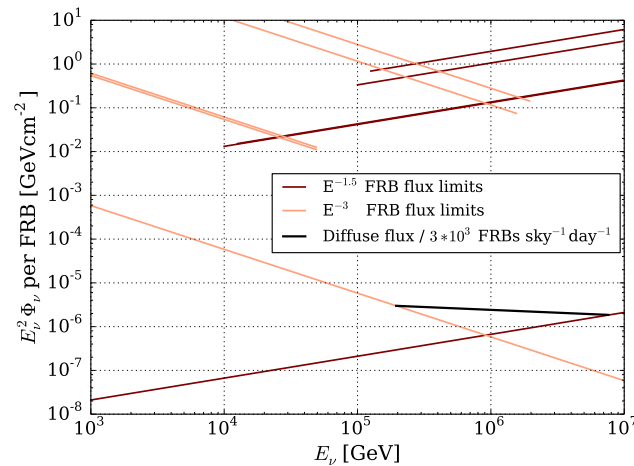| FRB	R.A.	Dec.	FRB MJD	Radio fluence (GeV cm^{-2})	Telescope	$\Delta\Psi_{\nu-\mathrm{FRB}}$	ν error (50%)	$f^{90\%}$ (GeV cm^{-2})
110523	21h45′	-00°12′	55704.63	2.37×10^{-15}	Green Bank	3.70°	0.3°	0.184
110627	21h03′	-44°44′	55739.90	1.75×10^{-15}	Parkes	4.85°	0.5°	4.84
110703	23h30′	-02°52′	55745.79	4.49×10^{-15}	Parkes	4.27°	1.2°	0.184
120127	23h15′	-18°25′	55953.34	1.50×10^{-15}	Parkes	4.07°	0.2°	2.76

Figure 6. The neutrino fluence upper limits for spectral indices 1.5 and 3.0 from Figure 5 (upper curves) are compared to limits for the same indices derived by the constraint that FRBs not over-produce the diffuse astrophysical ν_μ flux observed by IceCube at any particular neutrino energy, assuming equal neutrino flux from each of 3×10^3 FRBs per sky per day. The simple limits derived from the total diffuse emission are currently more constraining than the limits set by the dedicated FRB search. Stacking many FRBs will enable even stronger constraints.

REFERENCES

Bechtol, K., Ahlers, M., Mauro, M. D., Ajello, M., & Vandenbroucke, J. 2017, The Astrophysical Journal, 836, 47. http://stacks.iop.org/0004-637X/836/i=1/a=47
Champion, D. J., et al. 2016, Monthly Notices of the Royal Astronomical Society: Letters, 460, L30. http://mnrasl.oxfordjournals.org/content/460/1/L30.abstract
Chatterjee, S., Law, C. J., Wharton, R. S., et al. 2017, Nature, 541, 58
DeLaunay, J. J., Fox, D. B., Murase, K., et al. 2016, The Astrophysical Journal Letters, 832, L1. http://stacks.iop.org/2041-8205/832/i=1/a=L1
Falcke, H., & Rezzolla, L. 2014, Astronomy and Astrophysics, 562, A137
IceCube Collaboration. 2006, Astroparticle Physics, 26, 155 . http://www.sciencedirect.com/science/article/pii/S0927650506000855
—. 2011, Astron. Astrophys., 535, A109, [Erratum: Astron. Astrophys.563,C1(2014)]
—. 2012, Nature, 484, 351
—. 2013a, Phys. Rev. Lett., 111, 021103. http://link.aps.org/doi/10.1103/PhysRevLett.111.021103
—. 2013b, Science, 342, doi:10.1126/science.1242856
—. 2014a, Phys. Rev. Lett., 113, 101101. http://link.aps.org/doi/10.1103/PhysRevLett.113.101101
—. 2014b, The Astrophysical Journal, 796, 109. http://stacks.iop.org/0004-637X/796/i=2/a=109
—. 2015a, Phys. Rev. D, 91, 022001. http://link.aps.org/doi/10.1103/PhysRevD.91.022001
—. 2015b, Phys. Rev. Lett., 115, 081102. http://link.aps.org/doi/10.1103/PhysRevLett.115.081102
—. 2015c, The Astrophysical Journal, 809, 98. http://stacks.iop.org/0004-637X/809/i=1/a=98
—. 2015d, The Astrophysical Journal Letters, 805, L5. http://stacks.iop.org/2041-8205/805/i=1/a=L5
—. 2016a, The Astrophysical Journal, 833, 3. http://stacks.iop.org/0004-637X/833/i=1/a=3
—. 2016b, Search for point sources with the first year of IC86 data. IceCube Neutrino Observatory. Dataset, IceCube Neutrino Observatory. http://dx.doi.org/10.21234/B4159R
—. 2017a, Journal of Instrumentation, 12, P03012. http://stacks.iop.org/1748-0221/12/i=03/a=P03012
—. 2017b, ArXiv e-prints, arXiv:1702.06868
Keane, E. F., et al. 2016, Nature, 530, 453. http://dx.doi.org/10.1038/nature17140
Li, X., et al. 2014, The Astrophysical Journal, 797, 33. http://stacks.iop.org/0004-637X/797/i=1/a=33
Loeb, A., Shvartzvald, Y., & Maoz, D. 2014, MNRAS, 439, L46
Lorimer, D. R., et al. 2007, Science, 318, 777
Masui, K., et al. 2015, Nature, 528, 523. http://dx.doi.org/10.1038/nature15769
Murase, K., Kashiyama, K., & Mszros, . 2016, Monthly Notices of the Royal Astronomical Society, 461, 1498. +http://dx.doi.org/10.1093/mnras/stw1328
Pen, U.-L., & Connor, L. 2015, The Astrophysical Journal, 807, 179. http://stacks.iop.org/0004-637X/807/i=2/a=179
Petroff, E., Barr, E. D., Jameson, A., et al. 2016, Publications of the Astronomical Society of Australia, 33, doi:10.1017/pasa.2016.35
Rajwade, K. M., & Lorimer, D. R. 2017, Monthly Notices of the Royal Astronomical Society, 465, 2286. +http://dx.doi.org/10.1093/mnras/stw2914
Scholz, P., Spitler, L. G., Hessels, J. W. T., et al. 2016, The Astrophysical Journal, 833, 177. http://stacks.iop.org/0004-637X/833/i=2/a=177
Spitler, L. G., et al. 2016, Nature, 531, 202. http://dx.doi.org/10.1038/nature17168
Tendulkar, S. P., Bassa, C. G., Cordes, J. M., et al. 2017, The Astrophysical Journal Letters, 834, L7. http://stacks.iop.org/2041-8205/834/i=2/a=L7
Thornton, D., et al. 2013, Science, 341, 53
Tilav, S., et al. 2010, arXiv:1001.0776
Williams, P. K. G., & Berger, E. 2016, The Astrophysical Journal Letters, 821, L22. http://stacks.iop.org/2041-8205/821/i=2/a=L22

Appendix F

Paper: Six-year FRB Analysis

The second paper, corresponding to Chapter 5 in this thesis, is "A Search for Neutrino Emission from Fast Radio Bursts with Six Years of IceCube Data." It was published in *The Astrophysical Journal* on 23 April 2018 [76].

Using six years of high-energy track-like data, this analysis improved limits on neutrino emission from FRBs over timescales ranging from 0.01 s to 2 days. Limits are reported separately for the average per-source emission from the FRB source class, for the largest neutrino flux among all known FRB sources, and for each source individually.

Additional calculations discuss the outlook for sensitivity improvement given the expected increase in future FRB detections. A comparison of IceCube's effective area to that of ANTARES is provided to highlight respective regions of best detection efficiency, motivating a joint search for FRBs using IceCube and neutrino telescopes in the northern hemisphere like ANTARES and KM3NET. s

arXiv:1712.06277v1 [astro-ph.HE] 18 Dec 2017

A SEARCH FOR NEUTRINO EMISSION FROM FAST RADIO BURSTS WITH SIX YEARS OF ICECUBE DATA

ICECUBE COLLABORATION[a]: M. G. AARTSEN[1], M. ACKERMANN[2], J. ADAMS[1], J. A. AGUILAR[3], M. AHLERS[4], M. AHRENS[5], I. AL SAMARAI[6], D. ALTMANN[7], K. ANDEEN[8], T. ANDERSON[9], I. ANSSEAU[3], G. ANTON[7], C. ARGÜELLES[10], J. AUFFENBERG[11], S. AXANI[10], H. BAGHERPOUR[1], X. BAI[12], J. P. BARRON[13], S. W. BARWICK[14], V. BAUM[15], R. BAY[16], J. J. BEATTY[17,18], J. BECKER TJUS[19], K.-H. BECKER[20], S. BENZVI[21], D. BERLEY[22], E. BERNARDINI[2], D. Z. BESSON[23], G. BINDER[24,16], D. BINDIG[20], E. BLAUFUSS[22], S. BLOT[2], C. BOHM[5], M. BÖRNER[25], F. BOS[19], D. BOSE[26], S. BÖSER[15], O. BOTNER[27], E. BOURBEAU[4], J. BOURBEAU[28], F. BRADASCIO[2], J. BRAUN[28], L. BRAYEUR[29], M. BRENZKE[11], H.-P. BRETZ[2], S. BRON[6], J. BROSTEAN-KAISER[2], A. BURGMAN[27], T. CARVER[6], J. CASEY[28], M. CASIER[29], E. CHEUNG[22], D. CHIRKIN[28], A. CHRISTOV[6], K. CLARK[30], L. CLASSEN[31], S. COENDERS[32], G. H. COLLIN[10], J. M. CONRAD[10], D. F. COWEN[9,33], R. CROSS[21], M. DAY[28], J. P. A. M. DE ANDRÉ[34], C. DE CLERCQ[29], J. J. DELAUNAY[9], H. DEMBINSKI[35], S. DE RIDDER[36], P. DESIATI[28], K. D. DE VRIES[29], G. DE WASSEIGE[29], M. DE WITH[37], T. DEYOUNG[34], J. C. DÍAZ-VÉLEZ[28], V. DI LORENZO[15], H. DUJMOVIC[26], J. P. DUMM[5], M. DUNKMAN[9], E. DVORAK[12], B. EBERHARDT[15], T. EHRHARDT[15], B. EICHMANN[19], P. ELLER[9], P. A. EVENSON[35], S. FAHEY[28], A. R. FAZELY[38], J. FELDE[22], K. FILIMONOV[16], C. FINLEY[5], S. FLIS[5], A. FRANCKOWIAK[2], E. FRIEDMAN[22], T. K. GAISSER[35], J. GALLAGHER[39], L. GERHARDT[24], K. GHORBANI[28], W. GIANG[13], T. GLAUCH[32], T. GLÜSENKAMP[7], A. GOLDSCHMIDT[24], J. G. GONZALEZ[35], D. GRANT[13], Z. GRIFFITH[28], C. HAACK[11], A. HALLGREN[27], F. HALZEN[28], K. HANSON[28], D. HEBECKER[37], D. HEEREMAN[3], K. HELBING[20], R. HELLAUER[22], S. HICKFORD[20], J. HIGNIGHT[34], G. C. HILL[40], K. D. HOFFMAN[22], R. HOFFMANN[20], T. HOINKA[25], B. HOKANSON-FASIG[28], K. HOSHINA[28,53], F. HUANG[9], M. HUBER[32], K. HULTQVIST[5], M. HÜNNEFELD[25], S. IN[26], A. ISHIHARA[41], E. JACOBI[2], G. S. JAPARIDZE[42], M. JEONG[26], K. JERO[28], B. J. JONES[43], P. KALACZYNSKI[11], W. KANG[26], A. KAPPES[31], T. KARG[2], A. KARLE[28], U. KATZ[7], M. KAUER[28], A. KEIVANI[9], J. L. KELLEY[28], A. KHEIRANDISH[28], J. KIM[26], M. KIM[41], T. KINTSCHER[2], J. KIRYLUK[44], T. KITTLER[7], S. R. KLEIN[24,16], G. KOHNEN[45], R. KOIRALA[35], H. KOLANOSKI[37], L. KÖPKE[15], C. KOPPER[13], S. KOPPER[46], J. P. KOSCHINSKY[11], D. J. KOSKINEN[4], M. KOWALSKI[37,2], K. KRINGS[32], M. KROLL[19], G. KRÜCKL[15], J. KUNNEN[29], S. KUNWAR[2], N. KURAHASHI[47], T. KUWABARA[41], A. KYRIACOU[40], M. LABARE[36], J. L. LANFRANCHI[9], M. J. LARSON[4], F. LAUBER[20], M. LESIAK-BZDAK[44], M. LEUERMANN[11], Q. R. LIU[28], C. J. LOZANO MARISCAL[31], L. LU[41], J. LÜNEMANN[29], W. LUSZCZAK[28], J. MADSEN[48], G. MAGGI[29], K. B. M. MAHN[34], S. MANCINA[28], R. MARUYAMA[49], K. MASE[41], R. MAUNU[22], F. MCNALLY[28], K. MEAGHER[3], M. MEDICI[4], M. MEIER[25], T. MENNE[25], G. MERINO[28], T. MEURES[3], S. MIARECKI[24,16], J. MICALLEF[34], G. MOMENTÉ[15], T. MONTARULI[6], R. W. MOORE[13], M. MOULAI[10], R. NAHNHAUER[2], P. NAKARMI[46], U. NAUMANN[20], G. NEER[34], H. NIEDERHAUSEN[44], S. C. NOWICKI[13], D. R. NYGREN[24], A. OBERTACKE POLLMANN[20], A. OLIVAS[22], A. O'MURCHADHA[3], E. O'SULLIVAN[5], T. PALCZEWSKI[24,16], H. PANDYA[35], D. V. PANKOVA[9], P. PEIFFER[15], J. A. PEPPER[46], C. PÉREZ DE LOS HEROS[27], D. PIELOTH[25], E. PINAT[3], M. PLUM[8], D. PRANAV[50], P. B. PRICE[16], G. T. PRZYBYLSKI[24], C. RAAB[3], L. RÄDEL[11], M. RAMEEZ[4], K. RAWLINS[51], I. C. REA[32], R. REIMANN[11], B. RELETHFORD[47], M. RELICH[41], E. RESCONI[32], W. RHODE[25], M. RICHMAN[47], S. ROBERTSON[40], M. RONGEN[11], C. ROTT[26], T. RUHE[25], D. RYCKBOSCH[36], D. RYSEWYK[34], T. SÄLZER[11], S. E. SANCHEZ HERRERA[13], A. SANDROCK[25], J. SANDROOS[15], M. SANTANDER[46], S. SARKAR[4,52], S. SARKAR[13], K. SATALECKA[2], P. SCHLUNDER[25], T. SCHMIDT[22], A. SCHNEIDER[28], S. SCHOENEN[11], S. SCHÖNEBERG[19], L. SCHUMACHER[11], D. SECKEL[35], S. SEUNARINE[48], J. SOEDINGREKSO[25], D. SOLDIN[35], M. SONG[22], G. M. SPICZAK[48], C. SPIERING[2], J. STACHURSKA[2], M. STAMATIKOS[17], T. STANEV[35], A. STASIK[2], J. STETTNER[11], A. STEUER[15], T. STEZELBERGER[24], R. G. STOKSTAD[24], A. STÖSSL[41], N. L. STROTJOHANN[2], T. STUTTARD[4], G. W. SULLIVAN[22], M. SUTHERLAND[17], I. TABOADA[50], J. TATAR[24,16], F. TENHOLT[19], S. TER-ANTONYAN[38], A. TERLIUK[2], G. TEŠIĆ[9], S. TILAV[35], P. A. TOALE[46], M. N. TOBIN[28], S. TOSCANO[29], D. TOSI[28], M. TSELENGIDOU[7], C. F. TUNG[50], A. TURCATI[32], C. F. TURLEY[9], B. TY[28], E. UNGER[27], M. USNER[2], J. VANDENBROUCKE[28], W. VAN DRIESSCHE[36], N. VAN EIJNDHOVEN[29], S. VANHEULE[36], J. VAN SANTEN[2], M. VEHRING[11], E. VOGEL[11], M. VRAEGHE[36], C. WALCK[5], A. WALLACE[40], M. WALLRAFF[11], F. D. WANDLER[13], N. WANDKOWSKY[28], A. WAZA[11], C. WEAVER[13], M. J. WEISS[9], C. WENDT[28], J. WERTHEBACH[25], S. WESTERHOFF[28], B. J. WHELAN[40], K. WIEBE[15], C. H. WIEBUSCH[11], L. WILLE[28], D. R. WILLIAMS[46], L. WILLS[47], M. WOLF[28], J. WOOD[28], T. R. WOOD[13], E. WOOLSEY[13], K. WOSCHNAGG[16], D. L. XU[28], X. W. XU[38], Y. XU[44], J. P. YANEZ[13], G. YODH[14], S. YOSHIDA[41], T. YUAN[28], AND M. ZOLL[5]

[1] Dept. of Physics and Astronomy, University of Canterbury, Private Bag 4800, Christchurch, New Zealand

[2] DESY, D-15738 Zeuthen, Germany

[3] Université Libre de Bruxelles, Science Faculty CP230, B-1050 Brussels, Belgium

[4] Niels Bohr Institute, University of Copenhagen, DK-2100 Copenhagen, Denmark

[5] Oskar Klein Centre and Dept. of Physics, Stockholm University, SE-10691 Stockholm, Sweden

[6] Département de physique nucléaire et corpusculaire, Université de Genève, CH-1211 Genève, Switzerland

[7] Erlangen Centre for Astroparticle Physics, Friedrich-Alexander-Universität Erlangen-Nürnberg, D-91058 Erlangen, Germany

[8] Department of Physics, Marquette University, Milwaukee, WI, 53201, USA

[9] Dept. of Physics, Pennsylvania State University, University Park, PA 16802, USA

[10] Dept. of Physics, Massachusetts Institute of Technology, Cambridge, MA 02139, USA

[11] III. Physikalisches Institut, RWTH Aachen University, D-52056 Aachen, Germany

[12] Physics Department, South Dakota School of Mines and Technology, Rapid City, SD 57701, USA

[13] Dept. of Physics, University of Alberta, Edmonton, Alberta, Canada T6G 2E1

[a] analysis@icecube.wisc.edu

2

[14]Dept. of Physics and Astronomy, University of California, Irvine, CA 92697, USA

[15]Institute of Physics, University of Mainz, Staudinger Weg 7, D-55099 Mainz, Germany

[16]Dept. of Physics, University of California, Berkeley, CA 94720, USA

[17]Dept. of Physics and Center for Cosmology and Astro-Particle Physics, Ohio State University, Columbus, OH 43210, USA

[18]Dept. of Astronomy, Ohio State University, Columbus, OH 43210, USA

[19]Fakultät für Physik & Astronomie, Ruhr-Universität Bochum, D-44780 Bochum, Germany

[20]Dept. of Physics, University of Wuppertal, D-42119 Wuppertal, Germany

[21]Dept. of Physics and Astronomy, University of Rochester, Rochester, NY 14627, USA

[22]Dept. of Physics, University of Maryland, College Park, MD 20742, USA

[23]Dept. of Physics and Astronomy, University of Kansas, Lawrence, KS 66045, USA

[24]Lawrence Berkeley National Laboratory, Berkeley, CA 94720, USA

[25]Dept. of Physics, TU Dortmund University, D-44221 Dortmund, Germany

[26]Dept. of Physics, Sungkyunkwan University, Suwon 440-746, Korea

[27]Dept. of Physics and Astronomy, Uppsala University, Box 516, S-75120 Uppsala, Sweden

[28]Dept. of Physics and Wisconsin IceCube Particle Astrophysics Center, University of Wisconsin, Madison, WI 53706, USA

[29]Vrije Universiteit Brussel (VUB), Dienst ELEM, B-1050 Brussels, Belgium

[30]SNOLAB, 1039 Regional Road 24, Creighton Mine 9, Lively, ON, Canada P3Y 1N2

[31]Institut für Kernphysik, Westfälische Wilhelms-Universität Münster, D-48149 Münster, Germany

[32]Physik-department, Technische Universität München, D-85748 Garching, Germany

[33]Dept. of Astronomy and Astrophysics, Pennsylvania State University, University Park, PA 16802, USA

[34]Dept. of Physics and Astronomy, Michigan State University, East Lansing, MI 48824, USA

[35]Bartol Research Institute and Dept. of Physics and Astronomy, University of Delaware, Newark, DE 19716, USA

[36]Dept. of Physics and Astronomy, University of Gent, B-9000 Gent, Belgium

[37]Institut für Physik, Humboldt-Universität zu Berlin, D-12489 Berlin, Germany

[38]Dept. of Physics, Southern University, Baton Rouge, LA 70813, USA

[39]Dept. of Astronomy, University of Wisconsin, Madison, WI 53706, USA

[40]Department of Physics, University of Adelaide, Adelaide, 5005, Australia

[41]Dept. of Physics and Institute for Global Prominent Research, Chiba University, Chiba 263-8522, Japan

[42]CTSPS, Clark-Atlanta University, Atlanta, GA 30314, USA

[43]Dept. of Physics, University of Texas at Arlington, 502 Yates St., Science Hall Rm 108, Box 19059, Arlington, TX 76019, USA

[44]Dept. of Physics and Astronomy, Stony Brook University, Stony Brook, NY 11794-3800, USA

[45]Université de Mons, 7000 Mons, Belgium

[46]Dept. of Physics and Astronomy, University of Alabama, Tuscaloosa, AL 35487, USA

[47]Dept. of Physics, Drexel University, 3141 Chestnut Street, Philadelphia, PA 19104, USA

[48]Dept. of Physics, University of Wisconsin, River Falls, WI 54022, USA

[49]Dept. of Physics, Yale University, New Haven, CT 06520, USA

[50]School of Physics and Center for Relativistic Astrophysics, Georgia Institute of Technology, Atlanta, GA 30332, USA

[51]Dept. of Physics and Astronomy, University of Alaska Anchorage, 3211 Providence Dr., Anchorage, AK 99508, USA

[52]Dept. of Physics, University of Oxford, 1 Keble Road, Oxford OX1 3NP, UK

[53]Earthquake Research Institute, University of Tokyo, Bunkyo, Tokyo 113-0032, Japan

ABSTRACT

We present a search for coincidence between IceCube TeV neutrinos and fast radio bursts (FRBs). During the search period from 2010 May 31 to 2016 May 12, a total of 29 FRBs with 13 unique locations have been detected in the whole sky. An unbinned maximum likelihood method was used to search for spatial and temporal coincidence between neutrinos and FRBs in expanding time windows, in both the northern and southern hemispheres. No significant correlation was found in six years of IceCube data. Therefore, we set upper limits on neutrino fluence emitted by FRBs as a function of time window duration. We set the most stringent limit obtained to date on neutrino fluence from FRBs with an E^{-2} energy spectrum assumed, which is 0.0021 GeV cm^{-2} per burst for emission timescales up to ~10^2 seconds from the northern hemisphere stacking search.

1. INTRODUCTION

Fast radio bursts (FRBs) are a new class of astrophysical phenomenon characterized by bright broadband radio emission lasting only a few milliseconds. Since the first FRB discovered in 2007 in archival data from the Parkes Radio Telescope (Lorimer et al. 2007), more than 20 FRBs have been detected by a total of five observatories (Spitler et al. 2014; Masui et al. 2015; Caleb et al. 2017; Bannister et al. 2017). This rules out the hypothesis of instrumental or terrestrial origin of these phenomena. The number of FRBs detected together with the duration and solid angle searched imply an all-sky FRB occurrence rate of a few thousand per day (Thornton et al. 2013; Spitler et al. 2014), which is consistent with 10% of the supernova rate (Murase et al. 2016). The burst durations suggest that FRB progenitors are very compact, with light-transit distances on the order of hundreds of kilometers. The dispersion measures – the time delay of lower frequency signal components, which is proportional to the column density of free electrons along the line of sight – of the detected FRBs are significantly greater than the Milky Way alone could provide (Cordes et al. 2016), and the majority of sources have been detected at high Galactic latitudes, indicating extragalactic origin. The distances of the FRBs extracted from their dispersion measures, however, are only upper limits and precise measurements are yet to be determined, most likely from multi-wavelength observations.

The nature of FRBs is still under heated debate, and a multitude of models have been proposed for the FRB progenitors, the majority of which involve strong magnetic fields and leptonic acceleration. Some models predict millisecond radio bursts from cataclysmic events such as dying stars (Falcke & Rezzolla 2014), neutron star mergers (Totani 2013), or evaporating black holes (Rees 1977). In 2015, 16 additional bursts were detected from the direction of FRB 121102 (Spitler et al. 2014; Scholz et al. 2016), spaced out non-periodically by timescales ranging from seconds to days. This indicates that the cataclysmic scenario is not true at least for this repeating FRB. A multi-wavelength follow-up campaign identified this FRB's host dwarf galaxy at a distance of ~1 Gpc (Chatterjee et al. 2017). It is unclear whether FRB 121102 is representative of FRBs as a source class or if repetitions are possible for only a subclass of FRBs.

While leptonic acceleration is typically the default assumption for FRB emission in most models, hadronic acceleration is also possible in the associated regions of the progenitors, which would lead to production of high-energy cosmic rays and neutrinos (Li et al. 2014). It has been proposed that cosmological FRBs could link to exotic phenomena such as oscillations of superconducting cosmic strings (Ye et al. 2017), and some authors predict that such cosmic strings could also produce ultra-high energy cosmic rays and neutrinos, from super heavy particle decays (Berezinsky et al. 2009; Lunardini & Sabancilar 2012). Therefore, both multi-wavelength and multi-messenger follow-ups can provide crucial information to help decipher the origin of FRBs. Here, the IceCube telescope offers the opportunity to search for neutrinos correlated with FRBs.

The IceCube Neutrino Observatory consists of 5160 digital optical modules (DOMs) instrumenting one cubic kilometer of Antarctic ice from depths of 1450 m to 2450 m at the geographic South Pole (Aartsen et al. (IceCube Collaboration) 2017e). Charged products of neutrino interactions in the ice create Cherenkov photons which are observed by the DOMs and allow the reconstruction of the initial neutrino energy, direction, and interaction type. Charged-current muon neutrino interactions create muons, which travel along straight paths in the ice, resulting in events with directional resolution $\lesssim 1°$ at energies above 1 TeV (Maunu 2016). The detector – fully installed since 2010 – collects data from the whole sky with an up-time higher than 99% per year, enabling real-time alerts to other instruments and analysis of archival data as a follow-up to interesting signals detected by other observatories.

IceCube has discovered a diffuse astrophysical neutrino flux in the TeV to PeV energy range (Aartsen et al. (IceCube Collaboration) 2013b,a, 2014, 2015a,c, 2016a). The arrival directions of these neutrinos are consistent with an isotropic distribution, indicating a majority of them have originated from extragalactic sources. Although tau neutrinos are yet to be identified among the observed flux (Aartsen et al. (IceCube Collaboration) 2016b), the flavor ratio is found to be consistent with $\nu_e : \nu_\mu : \nu_\tau = 1$: 1 : 1 from analyses which combined multiple data sets (Aartsen et al. (IceCube Collaboration) 2015b) and with events starting inside the detector for all flavor channels. (Aartsen et al. (IceCube Collaboration) 2015d, 2017d). Close-to-equal flavor ratio is another feature of astrophysical neutrinos which have traversed astronomical distances and hence have reached full mixing (Argüelles et al. 2015; Bustamante et al. 2015). While the astrophysical neutrino flux has been detected in multiple channels with high significance, neither clustering in space or time nor cross correlations to catalogs have been found (Aartsen et al. (IceCube Collaboration) 2017a). The once promising sources for high-energy neutrinos such as gamma ray bursts (Abbasi et al. (IceCube Collaboration) 2012; Aartsen et al. (IceCube Collaboration) 2015e, 2017b) and blazars (Aartsen et al. (IceCube Collaboration) 2017c) have been disfavored as the major contributors to the observed flux. To date, the origin of the astrophysical neutrinos remains a mystery.

In Fahey et al. (2017), an analysis of four FRBs with one year of IceCube data was reported. Here we present the results

4

Table 1. For IceCube data during which an FRB was detected, the event rates, numbers of events, and respective livetimes are shown. Here, "IC79" indicates the first year of data used in this analysis, when the IceCube array consisted of 79 strings; "IC86-1", "IC86-2", etc. denote subsequent years of data from the completed 86-string array. The median angular uncertainty among events in each sample is given as a 90% containment radius, assuming each event reconstruction to have a 2-D Gaussian point-spread function. Since the event reconstruction becomes more accurate for higher energy events, the southern data sets have smaller median angular uncertainties as a consequence of harder energy cuts to reduce atmospheric background. Year-to-year variations in event rate and $\sigma_{90\%}$ are the result of event selection methods aimed to maximize sensitivity independently for each data set's corresponding set of sources in a previous search for GRBs, as described in Section 2.

Northern ($\delta > -5°$) Data	Start date	End date	Rate (mHz)	Events	Livetime (days)	$\sigma_{90\%}$
IC86-1	2011-05-13	2012-05-15	3.65	107,612	341.9	2.13°
IC86-2	2012-05-15	2013-05-02	5.50	157,754	332.2	2.68°
IC86-3	2013-05-02	2014-05-06	6.20	193,320	362.2	2.79°
IC86-4	2014-05-06	2015-05-15	6.17	197,311	369.8	2.79°
IC86-5	2015-05-15	2016-05-12	6.07	186,600	356.8	2.83°
Southern ($\delta < -5°$) Data	Start date	End date	Rate (mHz)	Events	Livetime (days)	$\sigma_{90\%}$
IC79	2010-05-31	2011-05-13	2.46	67,474	314.6	1.02°
IC86-1	2011-05-13	2012-05-15	1.90	58,982	359.6	1.10°
IC86-2	2012-05-15	2013-05-02	3.18	91,485	328.6	1.05°
IC86-3	2013-05-02	2014-05-06	3.23	100,820	358.6	1.04°
IC86-4	2014-05-06	2015-05-18	1.90	60,500	350.7	1.04°

of a more sophisticated study in search of high-energy neutrinos from 29 FRBs using the IceCube Neutrino Observatory. The paper is structured as follows: Section 2 describes the event sample used. We then discuss the analysis method, search strategies and background modeling in Section 3. In Section 4, we present the sensitivities and discovery potentials based on the analysis method and search strategies established in Section 3. We then report the final results and their interpretation in Section 5. Finally, we conclude and discuss the future prospects for FRB follow-ups with IceCube in Section 6.

2. EVENT SAMPLE

The data used in this analysis are assembled from muon neutrino candidate events selected in previous analyses in search of prompt neutrino coincidence with gamma ray bursts (GRBs) (Aartsen et al. (IceCube Collaboration) 2015e, 2017b). It consists of ten data sets: five years of data from the northern hemisphere and five from the southern hemisphere (Table 1). Due to the effects of atmospheric muon contamination, which are strong in the south and negligible in the north, the data samples are constructed in two "hemispheres" separated at a declination of $\delta = -5°$. The northern selection extends to $-5°$ rather than $0°$ declination because there is still sufficient Earth overburden at $-5°$ for efficient absorption of atmospheric muons.

2.1. *Northern data set*

The northern data samples ($\delta > -5°$) cover five years of IceCube operation from 2011 May 13 to 2016 May 12, during which 20 northern FRBs were detected (Table 2): three each from a unique source and 17 bursts from FRB 121102. In the northern hemisphere, the Earth filters out cosmic ray-induced atmospheric muons, so the data samples consist primarily of atmospheric muon neutrinos with a median energy on the order of 1 TeV. The event rate in the northern hemisphere increases from 3.5 mHz in the first year (Aartsen et al. (IceCube Collaboration) 2015e) to 6 mHz in later years (Aartsen et al. (IceCube Collaboration) 2017b), as shown in Figure 1. This year-to-year variation is due largely to two combined effects: first, the initial event selections treat each year of the IceCube data sample independently due to filter and data processing scheme updates in the early years of IceCube operation; second, each data sample was separately optimized for sensitivity to its corresponding set of GRBs[1].

Within each year, a seasonal variation of the background rate can also be seen (Aartsen et al. (IceCube Collaboration) 2013c). In the Austral summer, the warming atmosphere expands and increases the average height and mean free path of products from cosmic-ray interactions, allowing pions to more frequently decay into $\mu + \nu_\mu$[2] and increasing the overall rate of atmospheric muons and neutrinos in IceCube. The phase of the seasonal variation in the northern sample is the same as that in the southern

---

[1] In the northern data set, the IC86-1 sample was optimized for sensitivity to a *stacking* search for GRBs. In later years, sensitivity to a *max-burst* search was instead optimized, accounting for the large year-to-year rate fluctuation between samples IC86-1 and IC86-2 (see Figure 1, Table 1).

[2] IceCube cannot differentiate between neutrinos and anti-neutrinos, so here ν_μ denotes both neutrinos and anti-neutrinos

sample because the northern sample is dominated by events between +15° and −5° in declination (Figure 2), which corresponds to production in the atmosphere at latitudes between −60° and −90°.

2.2. *Southern data set*

The southern data samples ($\delta < -5°$) consist of five years of data from 2010 May 31 to 2015 May 18, during which nine southern FRBs were detected. The year-to-year event rate, 2-3.5 mHz, is lower than that of the northern samples due mainly to a higher energy threshold imposed to reduce background from atmospheric muons and the asymmetric separation of hemispheres which makes the northern hemisphere ~20% larger in solid angle than the southern (Aartsen et al. (IceCube Collaboration) 2017b). The southern samples are dominated by down-going atmospheric muons with median energy on the order of 10 TeV. The effective area of IceCube to neutrino events which pass the event selection can be seen in Figure 3, where the effective area has been determined for the declination of each FRB in this analysis.
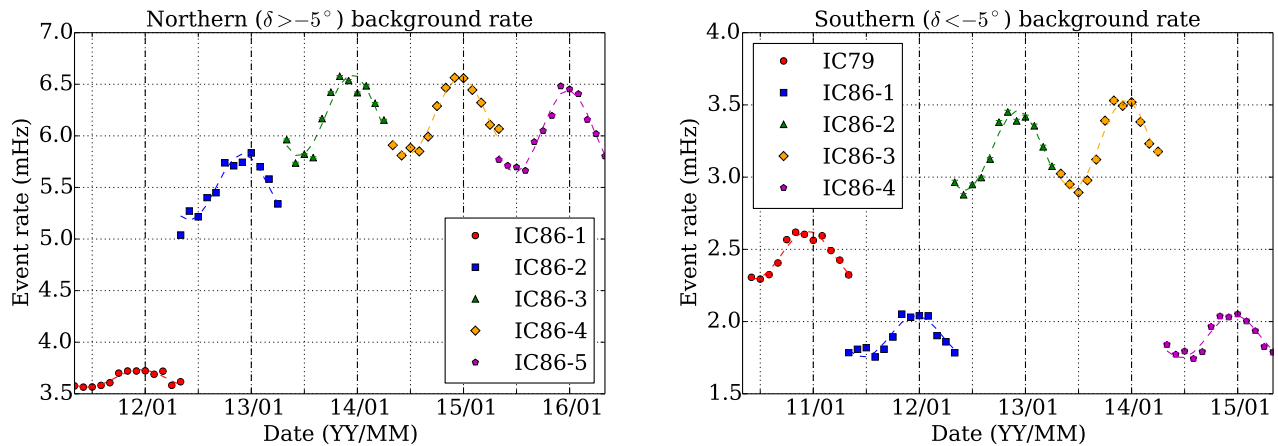

Figure 1. Event rates are shown for each data sample, binned by month and fit yearly with one period of a sine function. Year-to-year rate fluctuations reflect changes in event selection methods, not physical changes to the detector, while seasonal variation within each year is the result of the temperature dependence of atmospheric properties which affect atmospheric muon rates. In the northern hemisphere, seasonal variation accounts for a 2-5% amplitude (mean-to-peak) variation in the year-averaged rate. In the southern hemisphere, the amplitude of this fluctuation is 7-10%.
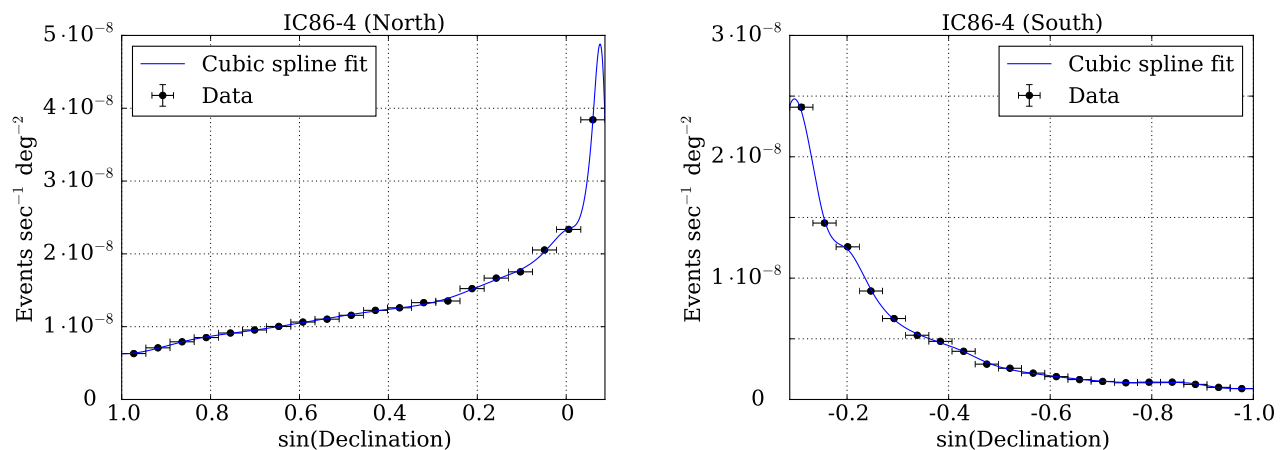

Figure 2. The distribution of events in reconstructed declination is shown for a representative year of off-time data in each hemisphere. Data samples are binned into 20 bins of equal width in sin(declination) and fit with a cubic polynomial spline with endpoints equal to the first and last bin values.

Table 2. 29 FRBs are included in this search: in the north, 20 bursts from 4 unique source locations, and in the south, 9 bursts each with a unique location. For each FRB, arrival time and dispersion-measure-corrected burst duration are provided with RA and Dec (J2000), as well as the IceCube data sample being recorded during its detection. For FRB 121102, which has been found to repeat, we label individual bursts with "b0", "b1", etc., sorted chronologically by time of detection. FRB 121002 was detected as two bursts separated by ~1 ms. It is treated as a single burst in this analysis, but we give both burst durations for completeness.

Northern ($\delta > -5°$) FRBs	Time (UTC)	Duration (ms)	RA	Dec	IceCube Data Sample
FRB 110523	2011-05-23 15:06:19.738	1.73	21h 45′	-00° 12′	IC86-1
FRB 110703	2011-07-03 18:59:40.591	< 4.3	23h 30′	-02° 52′	IC86-1
FRB 121102 b0	2012-11-02 06:47:17.117	3.3	05h 32′	33° 05′	IC86-2
FRB 130628	2013-06-28 03:58:00.02	< 0.05	09h 03′	03° 26′	IC86-3
FRB 121102 b1	2015-05-17 17:42:08.712	3.8	05h 32′	33° 05′	IC86-4
FRB 121102 b2	2015-05-17 17:51:40.921	3.3	05h 32′	33° 05′	IC86-4
FRB 121102 b3	2015-06-02 16:38:07.575	4.6	05h 32′	33° 05′	IC86-5
FRB 121102 b4	2015-06-02 16:47:36.484	8.7	05h 32′	33° 05′	IC86-5
FRB 121102 b5	2015-06-02 17:49:18.627	2.8	05h 32′	33° 05′	IC86-5
FRB 121102 b6	2015-06-02 17:49:41.319	6.1	05h 32′	33° 05′	IC86-5
FRB 121102 b7	2015-06-02 17:50:39.298	6.6	05h 32′	33° 05′	IC86-5
FRB 121102 b8	2015-06-02 17:53:45.528	6.0	05h 32′	33° 05′	IC86-5
FRB 121102 b9	2015-06-02 17:56:34.787	8.0	05h 32′	33° 05′	IC86-5
FRB 121102 b10	2015-06-02 17:57:32.020	3.1	05h 32′	33° 05′	IC86-5
FRB 121102 b11	2015-11-13 08:32:42.375	6.73	05h 32′	33° 05′	IC86-5
FRB 121102 b12	2015-11-19 10:44:40.524	6.10	05h 32′	33° 05′	IC86-5
FRB 121102 b13	2015-11-19 10:51:34.957	6.14	05h 32′	33° 05′	IC86-5
FRB 121102 b14	2015-11-19 10:58:56.234	4.30	05h 32′	33° 05′	IC86-5
FRB 121102 b15	2015-11-19 11:05:52.492	5.97	05h 32′	33° 05′	IC86-5
FRB 121102 b16	2015-12-08 04:54:40.262	2.50	05h 32′	33° 05′	IC86-5
Southern ($\delta < -5°$) FRBs	Time (UTC)	Duration (ms)	RA	Dec	IceCube Data Sample
FRB 110220	2011-02-20 01:55:48.957	5.6	22h 34′	-12° 24′	IC79
FRB 110627	2011-06-27 21:33:17.474	< 1.4	21h 03′	-44° 44′	IC86-1
FRB 120127	2012-01-27 08:11:21.723	< 1.1	23h 15′	-18° 25′	IC86-1
FRB 121002	2012-10-02 13:09:18.402	2.1; 3.7	18h 14′	-85° 11′	IC86-2
FRB 130626	2013-06-26 14:56:00.06	< 0.12	16h 27′	-07° 27′	IC86-3
FRB 130729	2013-07-29 09:01:52.64	< 4	13h 41′	-05° 59′	IC86-3
FRB 131104	2013-11-04 18:04:01.2	< 0.64	06h 44′	-51° 17′	IC86-3
FRB 140514	2014-05-14 17:14:11.06	2.8	22h 34′	-12° 18′	IC86-4
FRB 150418	2015-04-18 04:29:05.370	0.8	07h 16′	-19° 00′	IC86-4

3. ANALYSIS METHODS

3.1. *Unbinned likelihood method*

An unbinned maximum likelihood method is used to search for spatial and temporal coincidence of neutrino events with detected FRBs (Aartsen et al. (IceCube Collaboration) 2015f). In a given coincidence window ΔT centered on the time of detection of each FRB, the likelihood of observing N events for an expected $(n_s + n_b)$ events is

$$\mathscr{L}(N, \{x_i\}; n_s + n_b) = \frac{(n_s + n_b)^N}{N!} \cdot \exp\left[-(n_s + n_b)\right] \cdot \prod_{i=1}^{N} \frac{n_s S(x_i) + n_b B(x_i)}{n_s + n_b} \tag{1}$$

where n_s and n_b are the expected number of observed signal and background events, x_i is the reconstructed direction and estimated angular uncertainty for each event i, $S(x_i)$ is the signal PDF – taken to be a radially symmetric 2D Gaussian with standard deviation σ_i – evaluated for the angular separation between event i and the FRB with which it is temporally coincident, and $B(x_i)$ is the background PDF for the data sample to which event i belongs evaluated at the declination of event i. The uncertainties of the FRB locations are taken into account in $S(x_i)$, but they are significantly smaller than the median angular uncertainty of the data. In any
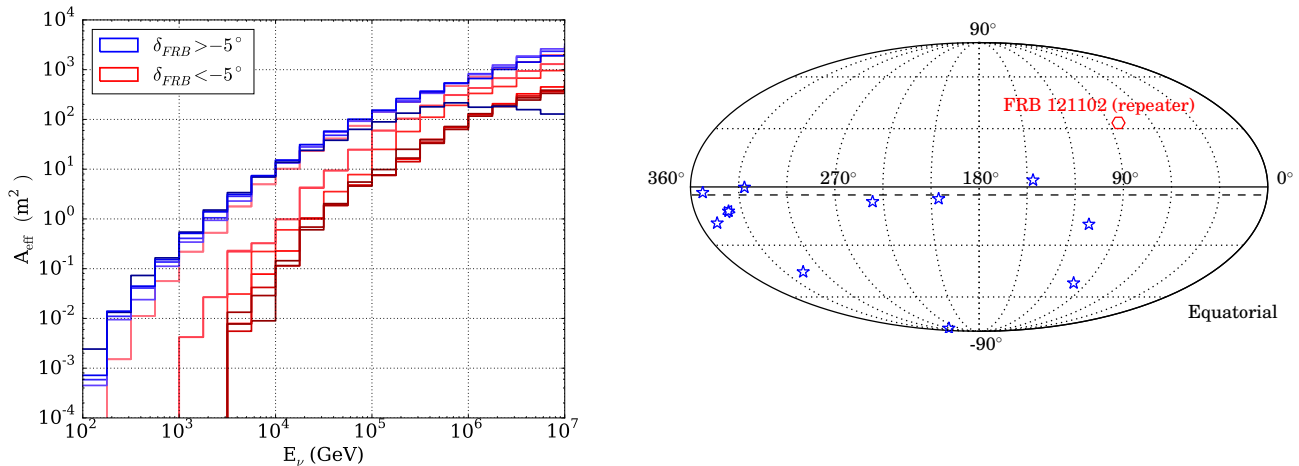
Figure 3. *Left*: the effective area of IceCube to muon neutrinos with energies 100 GeV - 10 PeV is shown for the event selection applied to this analysis' data samples. The effective area was calculated for a declination range $\Delta \sin(\delta) = 0.04$ centered on the declination of each FRB using the event selection corresponding each FRB's respective year of data. In total, 15 unique curves are plotted (three curves are calculated for FRB 121102, one for each year during which it was detected), although they sometimes overlap. Northern- and southern-sky FRBs are plotted in blue and red respectively, with a color scale for each corresponding to declination (darker near poles and lighter near celestial equator). In the southern hemisphere, IceCube's energy cuts to reduce atmospheric muon contamination result in a smaller effective area at lower energies. In the northern hemisphere, the effective area of IceCube benefits from shielding by the Earth from muons until, at energies above 100 TeV, the increased neutrino-nucleon cross section results in significant absorption of up-going neutrinos. However, because of the declinations of these FRBs, this effect is only easily seen here for FRB 121102 ($\delta = 33°$, dark blue curve), for which A_{eff} begins to decrease at 1 PeV. *Right*: FRB locations in the sky. The FRB 121102 (red hexagon) has repeated 16 times, and the other FRBs (blue stars) have not been observed to repeat.

time window ΔT, the N events are those which IceCube detected within $\pm\Delta$T$/2$ of any FRB detection. Before background event rates and PDFs were calculated, *on-time data* – data collected within ± 2 days of any FRB detection – were removed from the samples until all analysis procedures were determined. The remaining data (>1700 days of data per hemisphere) are considered *off-time data*, which we used to determine background characteristics to prevent artificial bias from affecting the results of our search. Figure 2 shows examples of off-time data distributions for both northern and southern hemispheres.

A generic test statistic (TS) is used in this analysis, defined as the logarithmic ratio of the likelihood of the alternative hypothesis $\mathscr{L}(N, \{x_i\}; n_s + n_b)$ and that of the null hypothesis $\mathscr{L}_0(N, \{x_i\}; n_b)$, which can be written as

$$\mathrm{TS} = -n_s + \sum_{i=1}^{N} \ln \left[1 + \frac{n_s S(x_i)}{n_b B(x_i)} \right] \tag{2}$$

The TS is maximized with respect to n_s to find the most probable number of signal-like events among N temporally coincident events. n_b is calculated by multiplying time-dependent background rate for each FRB, modeled from off-time data, by ΔT.

Two search strategies are implemented based on this test statistic. The *stacking* search tests the hypothesis that the astrophysical class of FRBs emits neutrinos. In this search, n_s and n_b are the total number of expected signal and background events contained in the time windows of an entire list of FRBs for the hemisphere. One TS value (with its corresponding n_s) is returned for an ensemble of N events which consist of on-time events from all the bursts. This TS represents the significance of correlation between the events analyzed and the source class as a whole. The *max-burst* search tests the hypothesis that one or a few bright sources emit neutrinos regardless of source classification. In this search, n_s and n_b are evaluated separately for each FRB. A TS-n_s pair is calculated for each FRB considering only the events coincident with its time window. The most statistically significant of these TS (and its corresponding n_s) is returned as the max-burst TS value of the ensemble.

Since neutrino emission mechanisms and potential neutrino arrival times relative to the time of radio detection are unknown, we employ a model-independent search using an expanding time window, similar to a previous search for prompt neutrino emission

from gamma ray bursts by IceCube which found no correlation (Abbasi et al. (IceCube Collaboration) 2012). Starting with $\Delta T = 0.01$ s centered on each FRB, we search a series of time windows expanding by factors of two, i.e. $\Delta T = 2^j \cdot (0.01\text{ s})$ for $j = 0, 1, 2, ..., 24$. We stop expanding at a time window size of 1.94 days (167772.16 s), where the background becomes significant. For the repeating burst FRB 121102 with burst separations less than the largest time window searched, time windows of consecutive bursts stop expanding when otherwise they would overlap.

In the northern max-burst search, a bright radio burst with a flux of 7.5 Jy detected by the LOFAR radio array (Stewart et al. 2016) was included. This LOFAR burst was detected on 2011 December 24 at 04:33 UTC, near the North Celestial Pole (RA = $22^h53^m47.1^s$, DEC = $+86°21'46.4''$) and lasted ~11 minutes. The burst was not consistent with an FRB, so it was not included in the stacking search, during which some degree of uniformity among the stacked source class was required.

3.2. Background ensembles

For each search method and hemisphere, we simulate 10^9 background-only Monte Carlo pseudo-experiments for every ΔT. This is done by first finding the seasonal variation-adjusted background rate (from Figure 1) for each FRB in the hemisphere. The product of these rates and ΔT gives a set of mean values for the Poisson distributions from which background events will be drawn. In a single trial, the number of events in the time window of each FRB is randomly drawn, and each event is assigned spatial coordinates which are uniform in detector azimuth and have declination values drawn from the PDFs shown in Figure 2. An angular uncertainty for each event is also randomly assigned from the angular distribution of the off-time data (Maunu 2016). The TS value for the trial is maximized with respect to n_s and the process is repeated for 10^9 trials, forming a TS distribution for the background-only hypothesis.

For example, Figure 4 shows the background-only TS distribution for the southern stacking search at $\Delta T = 10485.76$ s. Negative TS values are rounded to zero for the purposes of calculating the significance of analysis results. Building a TS distribution in this manner implicitly factors in a trials factor for the number of bursts searched, since increasing the number of sources inflates the TS values of both the analysis result and the background-only distribution. However, there is an additional trials factor when searching in overlapping time windows, so the cross-time-window trials factor must be accounted for when calculating significance values.
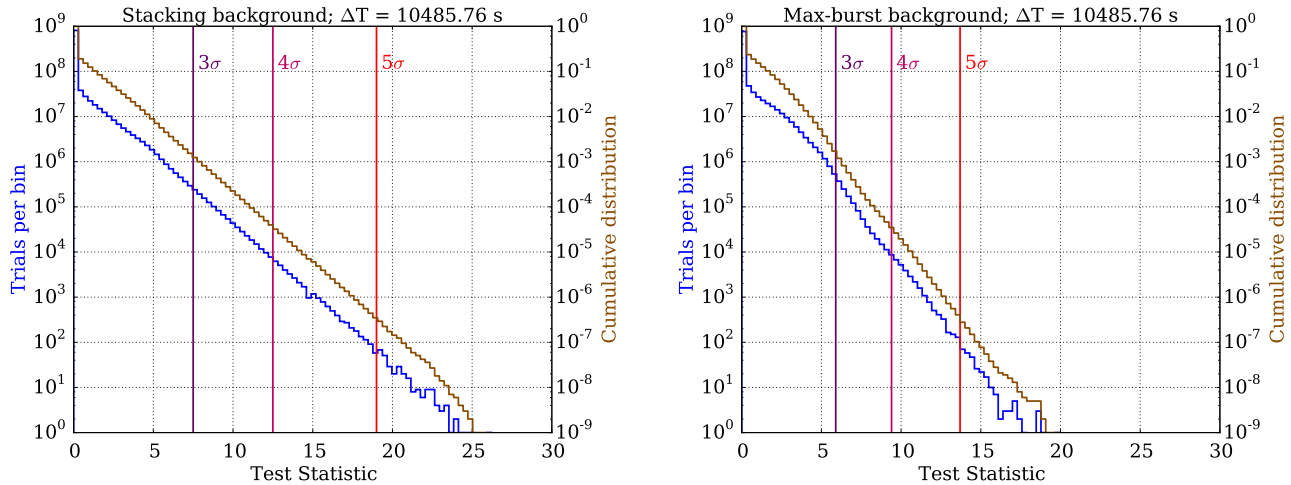

Figure 4. TS distributions are shown for 10^9 background-only Monte Carlo trials in the southern stacking and max-burst searches at $\Delta T = 10485.76$ s. Significance thresholds (e.g. 5σ) are determined using the corresponding p-value for one tail of a normal distribution. In the low-background regime, each trial is unlikely to contain any spatially coincident events, thus the majority of trials are more background-like than signal-like, returning a negative TS value. These are rounded to zero, resulting in low-background TS distributions peaked sharply at TS = 0. As ΔT increases, the height of the background TS distribution at TS = 0 approaches 50% of trials as expected.

For each search, the analysis procedure returns the most optimal time window and the corresponding TS-n_s pair, as determined by the p-value of the observed TS in the background-only distribution. Post-trial p-values are obtained by investigating more ensembles of background-only trials. For each trial, a set of events is injected for the largest ΔT following the background-only procedure described above. Then, for each ΔT, a TS value is calculated relative to its corresponding subset of events which are

randomly selected from the total event set. The most significant of these TS values has a p-value which becomes one background-only pre-trial p-value. These trials are repeated 10^5 times, forming a pre-trial p-value distribution. The position of the pre-trial p-value from the search on on-time data in this distribution determines its post-trial p-value.

4. SENSITIVITY

The sensitivity and discovery potential are calculated by injecting signal events following an assumed unbroken power law energy spectrum (E^{-2}, $E^{-2.5}$, and E^{-3}) on top of injected background events. The injected signal fluence (time integrated flux, denoted as F) is found which yields a certain probability of obtaining a certain significance in the background-only TS distribution (Neyman 1937; Aartsen et al. (IceCube Collaboration) 2017b). Specifically, sensitivity and discovery potential are defined as the minimum signal fluences required to surpass, respectively, the median in 90% of the trials and the 5σ point in 90% of the trials. Figure 5 shows the sensitivities and 5σ discovery potentials for both hemispheres and search strategies. The searches in the northern hemisphere are roughly an order of magnitude more sensitive than those in the south, because of the differences in effective area as described in Section 2.

At $\Delta T = 0.01$ s, we expect fewer than 0.001 background events all-hemisphere per trial in each search. As a result, the median background-only TS value is zero for all ΔT until it becomes more probable than not that a background event is injected near an FRB location, resulting in a non-zero TS value. In general, the sensitivity remains constant in a ΔT range that is relatively background-free and transitions to a monotonically increasing function in background-dominated ΔT. We still search all of these low-background ΔT because the discovery potential increases even in the small background regime (Figure 5).
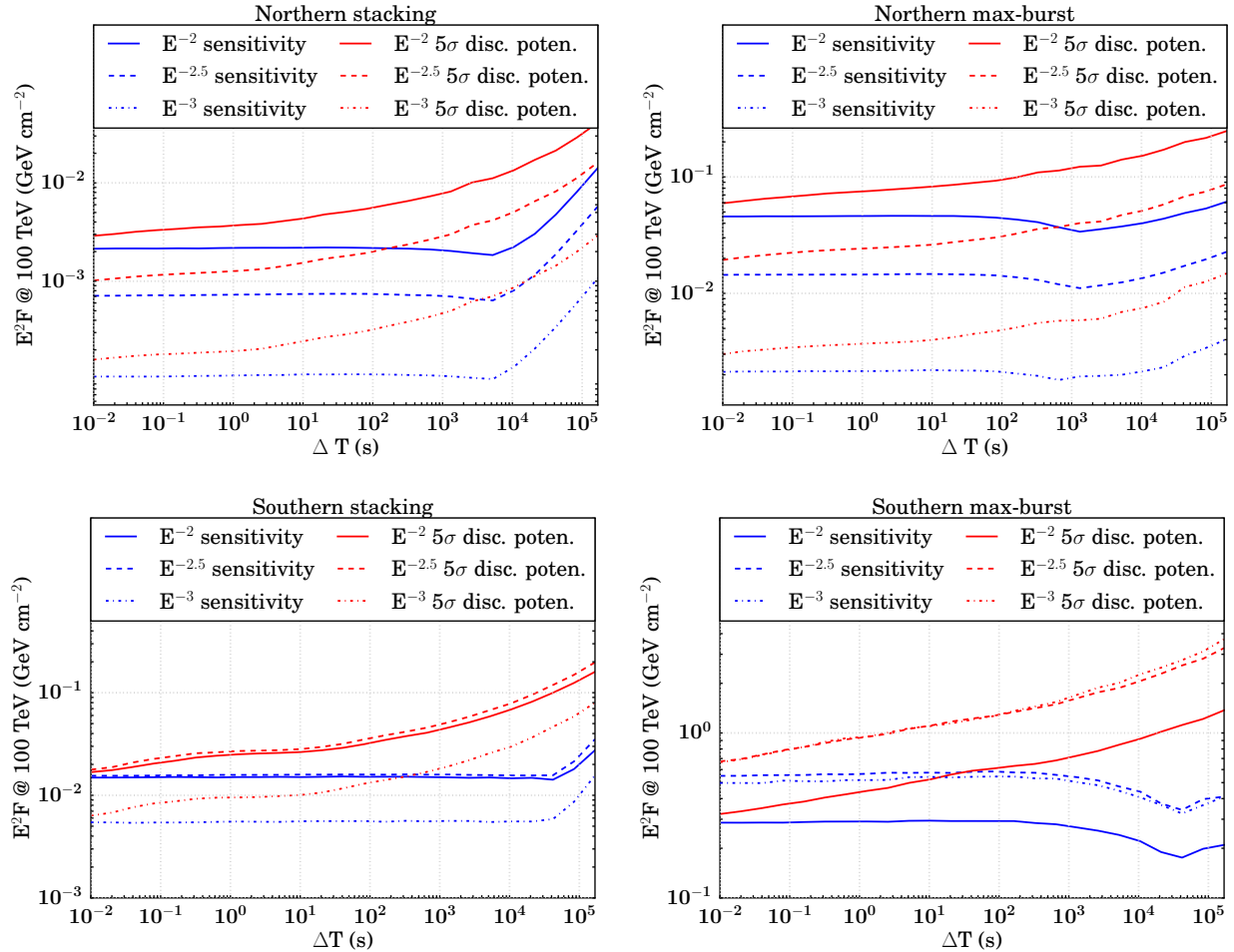

Figure 5. Sensitivity and 5σ discovery potential (90% confidence level) versus time-window size are shown for the northern hemisphere stacking, northern max-burst, southern stacking, and southern max-burst searches. The values plotted are E^2 times the time-integrated flux per burst at 100 TeV, for signal spectra of E^{-2}, $E^{-2.5}$, and E^{-3}.

Table 3. Analysis results are summarized for searches in both the northern and southern hemispheres. Where a most significant TS is found, the timing and directional separation of the event which most contributed to that TS value are provided. In the southern stacking test, the TS values for all time windows are zero; there is no ΔT searched which is more signal-like than background-like.

Northern ($\delta > -5°$)	best fit TS	best fit n_s	most significant event ($t - t_{\mathrm{FRB}}$, $\Delta\Psi$)	pre-trial p (post-trial p)	optimal ΔT	coincident FRB
max-burst test	3.90	0.99	(+200.806 s, 2.31°)	0.034 (0.25)	655.36 s	FRB121102 repeater 2015/06/02 16:38:07.575 UTC
stacking test	1.41	1.01	(+200.806 s, 2.31°)	0.074 (0.375)	655.36 s	FRB121102 repeater 2015/06/02 16:38:07.575 UTC

Southern ($\delta < -5°$)	best fit TS	best fit n_s	most significant event ($t - t_{\mathrm{FRB}}$, $\Delta\Psi$)	pre-trial p (post-trial p)	optimal ΔT	coincident FRB
max-burst test	0.64	0.78	(-16.9 hrs, 0.20°)	0.412 (0.84)	167772.16 s	FRB 140514 2014/05/14 17:14:11.06 UTC
stacking test	0	0	–	1.0 (1.0)	–	–

As a result of our methodology, there is a point in the background transition region where the sensitivity fluence appears to improve. Where the median of the background TS distribution is zero, the 90% sensitivity threshold for signal injection remains constant. But when ΔT is growing, there are more background events in each trial which can give rise to non-zero TS values, so the injected fluence necessary to meet the criteria for sensitivity is less. Once the median background TS value becomes non-zero, the sensitivity increases as expected.

5. RESULTS

After correcting for trials factors induced by 25 overlapping time windows searched, no significant correlation between neutrino events and FRBs is found (nor with the LOFAR burst). The most significant pre-trial p-value ($p = 0.034$) is found in the northern max-burst search at $\Delta T = 655.36$ s, with best-fit TS and n_s of 3.90 and 0.99 respectively. The post-trial p-value for this search is $p = 0.25$. In the same ΔT, the northern stacking search returned a best-fit TS and n_s of 1.41 and 1.01 respectively, corresponding to a pre-trial p-value $p = 0.074$ and post-trial p-value $p = 0.375$. The most signal-like event for both searches occurred 200.806 s after FRB 121102 b3, with an angular separation of 2.31° and estimated angular uncertainty of 1.31°.

In the southern hemisphere, the max-burst search returns the most significant pre-trial p-value ($p = 0.412$) at $\Delta T = 167772.16$ s with TS and n_s of 0.64 and 0.78, for a post-trial p-value of $p = 0.84$. In the southern stacking search, no TS value greater than zero was ever obtained for all ΔT. Even for the largest ΔT, where the southern max-burst search returned a positive TS value at one FRB, the order-of-magnitude increase in background for 9 FRBs stacked sufficiently diminished the significance of the events. Analysis results are summarized in Table 3, and sky maps of the events which most contributed to the results of each hemisphere are shown in Figure 6.

To set upper limits on the neutrino emission from FRBs, we use the same method which determines sensitivity, using the observed TS rather than the background-only median as a significance threshold. For most ΔT, both the background median and analysis result TS values are zero, resulting in an upper limit equal to the sensitivity (Figure 7). The northern stacking search returned the most constraining 90% confidence level upper limit for E^{-2} neutrino emission from FRBs among all four searches in this analysis, $E^2F = 0.0021$ GeV cm^{-2} per burst.

This process has been repeated for each source separately to calculate per-burst upper limits (see Table 4). E^{-2} fluence upper limits were determined by running background and signal-injection trials for a source list containing only one FRB, repeated for each unique source and for each year in which FRB 121102 was detected.

6. CONCLUSION AND OUTLOOK

In a search for muon neutrinos from 29 FRBs detected from 2010 May 31 to 2016 May 12, no significant correlation has been found. In both hemispheres, several events were found to be spatially coincident with some FRBs but also consistent with background.

Therefore, we set upper limits on neutrino emission from FRBs as a function of time window searched. For a E^{-2} energy spectrum, the most stringent limit on neutrino fluence per burst is $E^2F = 0.0021$ GeV cm^{-2}, obtained from the shortest time window (10 ms) in the northern stacking search. This limit is much improved in comparison to a previous search with only one
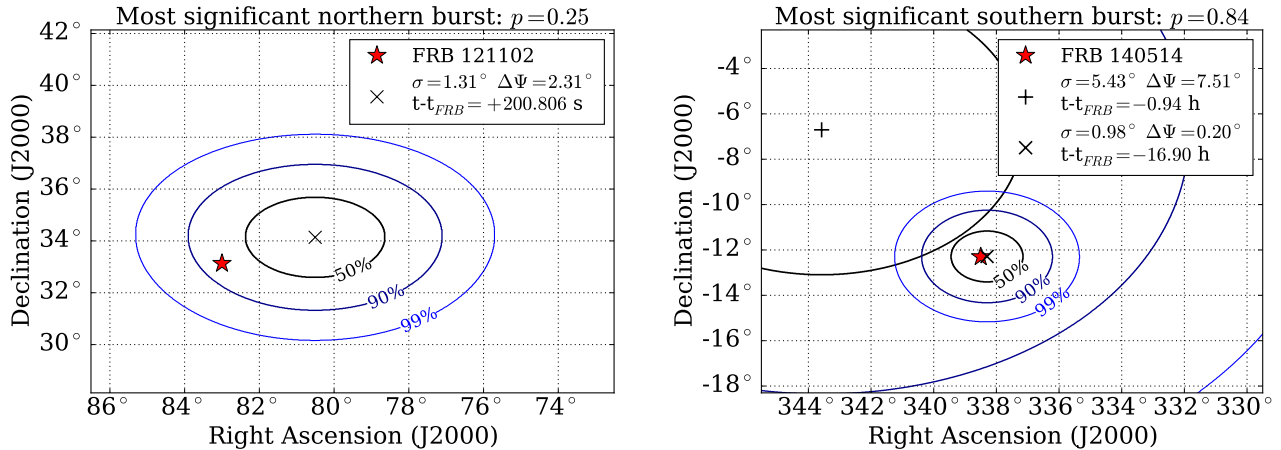
Figure 6. *Left*: The most signal-like event in both northern searches was detected 200.806 s after the radio detection of FRB 121102 b3. The directional reconstruction of this event has an angular separation $\Delta\Psi = 2.31°$ with the FRB and an estimated error $\sigma = 1.31°$. Event reconstruction contours are drawn for confidence intervals of 50%, 90%, and 99%, taking the reconstruction as a radially symmetric 2-D Gaussian. FRB directional uncertainty ($\ll 1°$) is taken into account in this analysis, but not shown for this scale. The post-trial p-value for this max-burst search is $p = 0.25$. *Right*: The most signal-like event in the southern searches was coincident with FRB 140514, with which two events' 90%-confidence intervals overlap. One event was detected 0.94 hours before the detection of FRB 140514 with reconstructed angular separation $\Delta\Psi = 7.51°$ and estimated error $\sigma = 5.43°$. The second was detected only in the largest time window, 16.90 hours before the FRB, with $\Delta\Psi = 0.20°$ and $\sigma = 0.98°$. Although this event appears remarkably coincident with the location of FRB 140514, its significance suffers from the high background rate of the time window in which it first appears. Its angular uncertainty is also roughly twice the median angular uncertainty of its background sample, reducing the contribution its signal PDF $S(x_i)$ has on the TS value. The post-trial p-value for this max-burst search is $p = 0.84$.

Table 4. Neutrino fluence upper limits (90% confidence) are constructed assuming an E^{-2} spectrum. The limits have been calculated for each burst individually for the $\Delta T = 0.01$ s time window and are shown here as $E^2 F$. Each burst from FRB 121102 has a limit corresponding to the year of data during which it was detected.

| FRB	Dec	E^{-2} fluence upper limit (GeV cm^{-2})
FRB 121002	-85° 11′	1.16
FRB 131104	-51° 17′	1.03
FRB 110627	-44° 44′	0.963
FRB 150418	-19° 00′	0.331
FRB 120127	-18° 25′	0.318
FRB 110220	-12° 24′	0.184
FRB 140514	-12° 18′	0.192
FRB 130626	-07° 27′	0.153
FRB 130729	-05° 59′	0.136
FRB 110703	-02° 52′	0.0575
FRB 110523	-00° 12′	0.0578
FRB 130628	03° 26′	0.0643
FRB 121102 b0	33° 05′	0.0932
FRB 121102 b1-b2	33° 05′	0.0925
FRB 121102 b3-b16	33° 05′	0.0919
LOFAR transient	86° 22′	0.164
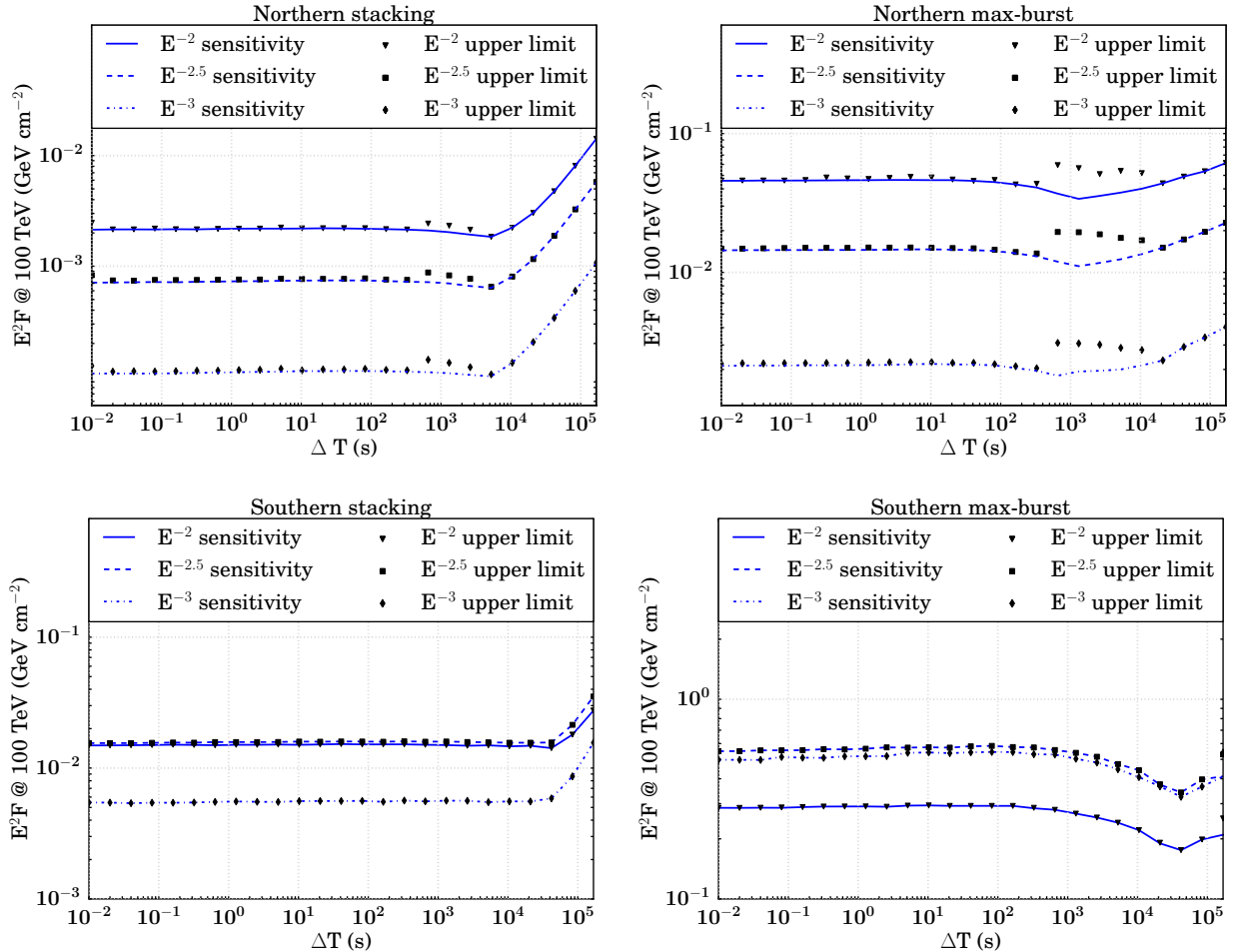
Figure 7. Sensitivity and upper limits (90% confidence level) per burst versus ΔT for the stacking and max-burst search in each hemisphere. For the largest ΔT's, in the case that an upper limit fluctuates below the sensitivity, we make the conservative choice to raise the upper limit to the sensitivity value.

year of IceCube data and using a binned likelihood method (Fahey et al. 2017). The limits set in this paper are also the most constraining ones on neutrinos from FRBs for neutrino energies above 1 TeV.

At the moment, we can set even more constraining limits on high-energy neutrino emission from FRBs using IceCube's astrophysical ν_μ flux measurement (Aartsen et al. (IceCube Collaboration) 2016a), assuming the current catalog of detected FRBs is representative of a homogeneous source class. Using an estimated all-sky FRB occurrence rate of 3,000 sky^{-1} day^{-1} (Macquart & Ekers 2017), the ν_μ fluence per FRB at 100 TeV cannot exceed $E^2F = 1.9 \cdot 10^{-6}$ GeV cm^{-2} for an emission spectrum of E^{-2}; otherwise, FRBs would contribute more than the entire measured astrophysical ν_μ flux. The astrophysical flux used here is extrapolated from a fit at energies of 194 TeV – 7.8 PeV, so it is only a rough estimate of the maximum neutrino emission from FRBs in the energy range this analysis concerns.

With newly operating radio observatories like CHIME (CHIME Scientific Collaboration 2017), we expect on the order of 1,000 FRBs to be discovered quasi-isotropically each year, which will improve the sensitivity of IceCube to a follow-up stacking search by orders of magnitude (Figure 8). Future analyses using IceCube data may also benefit from a more inclusive dataset, allowing a higher overall rate of muon-like and cascade-like events in exchange for increased sensitivity at $\Delta T < 1,000$ s. Cascade-like events do not contain muons, and as a result provide an angular resolution on the order of $10°$. However, a coincident event may still provide potential for high significance in very short time windows, where background is low. Furthermore, if some sub-class of FRBs is associated with nearby supernovae, MeV-scale neutrinos can be searched in the IceCube supernova stream which looks for a sudden increase in the overall noise rate of the detector modules (Abbasi et al. (IceCube Collaboration) 2011).

The ANTARES neutrino observatory is most sensitive in the southern hemisphere, where the majority of FRB sources have

been detected to date. Higher FRB detection rate (due to more observation time) from the southern hemisphere also provides ANTARES the opportunities for rapid follow-up observations when FRBs are caught in real time (Petroff et al. 2017). However, we emphasize that IceCube also has excellent sensitivity in much of the southern hemisphere. In Figure 9, we provide a quantitative comparison of the effective areas of the two observatories, which can serve as a useful reference when future FRBs are detected at arbitrary declinations. At energies above 50 TeV, the effective area of IceCube to neutrinos is the highest of any neutrino observatory across the entire (4π) sky (Figure 9). For $E_\nu < 50$ TeV, particularly where $\sin(\delta) < -0.33$, ANTARES com-
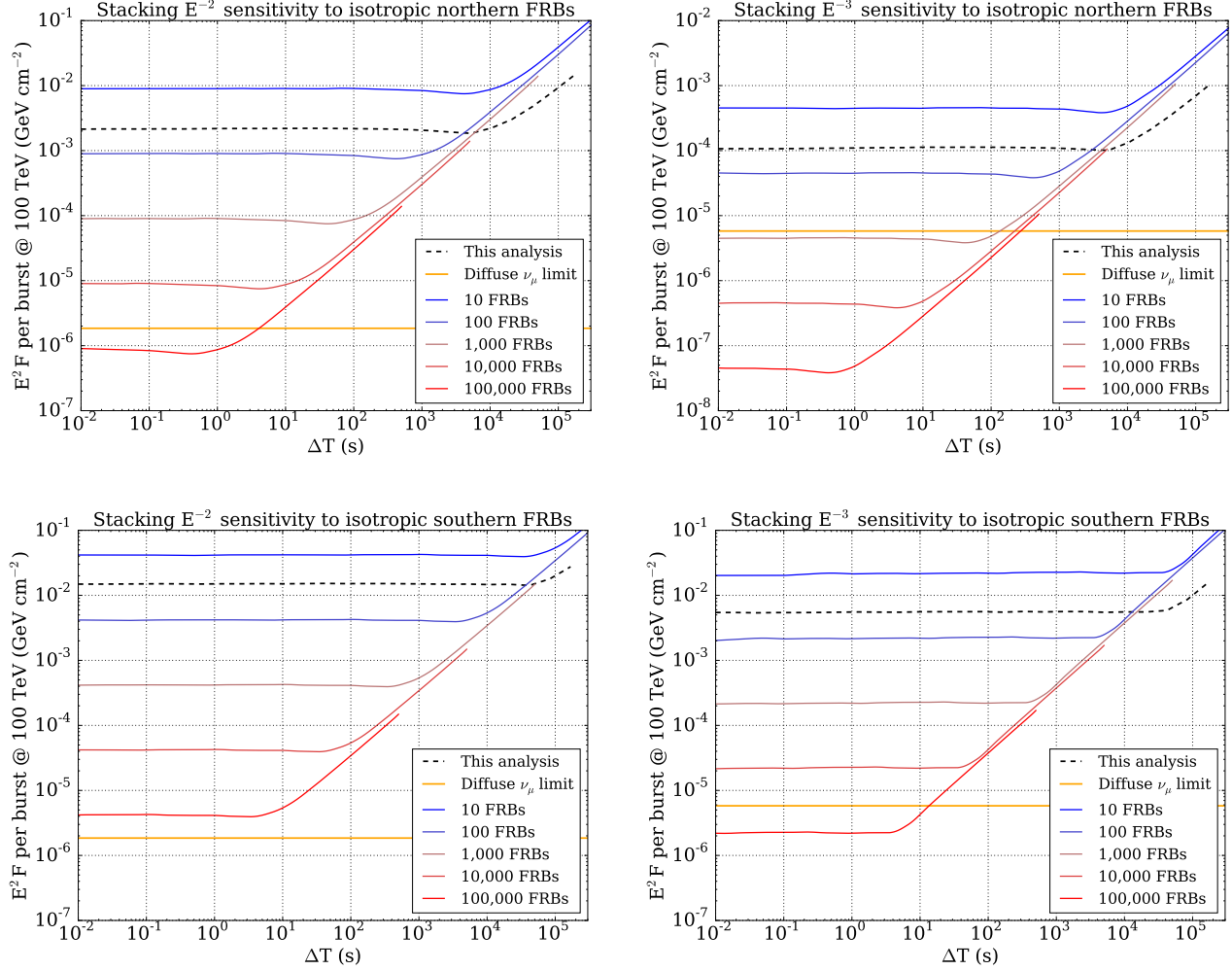
Figure 8. The stacking sensitivity to FRBs relies on the number and locations of sources detected. Since the list of detected FRBs is expected to grow exponentially in the coming years and without significant directional bias, the per-burst sensitivity to an isotropic hemisphere of FRBs has been calculated for a range of source list sizes. Sensitivity vs. ΔT is shown for two emission spectra, E^{-2} and E^{-3}, in each hemisphere for source list sizes ranging from $10 - 100,000$ FRBs. The respective stacking sensitivities from this analysis are overlaid for comparison, with total fluence divided by the number of sources – 9 in the south, 20 in the north – for *per-burst* fluence. These sensitivities outperform the expected sensitivity to an isotropic sky because the FRBs in this analysis were of higher-than-isotropic declination on average. Since our background rates peak at the horizon, the rate of coincident background events in stacking trials was lower than would be expected from an isotropic distribution of FRBs as well. This lowers the baseline for the stacking sensitivity curve and moves the up-turn at large ΔT to the right, as shown by the crossover near 10^4 s in each plot. For comparison, the limits set by constraining the total all-sky FRB fluence to be less than or equal to IceCube's astrophysical ν_μ flux are provided, assuming an FRB occurrence rate of 3,000 sky^{-1} day^{-1}. With data optimized specifically for sensitivity to FRBs and an orders-of-magnitude larger FRB source list, we expect future limits to improve upon those set by IceCube's diffuse astrophysical neutrino flux.
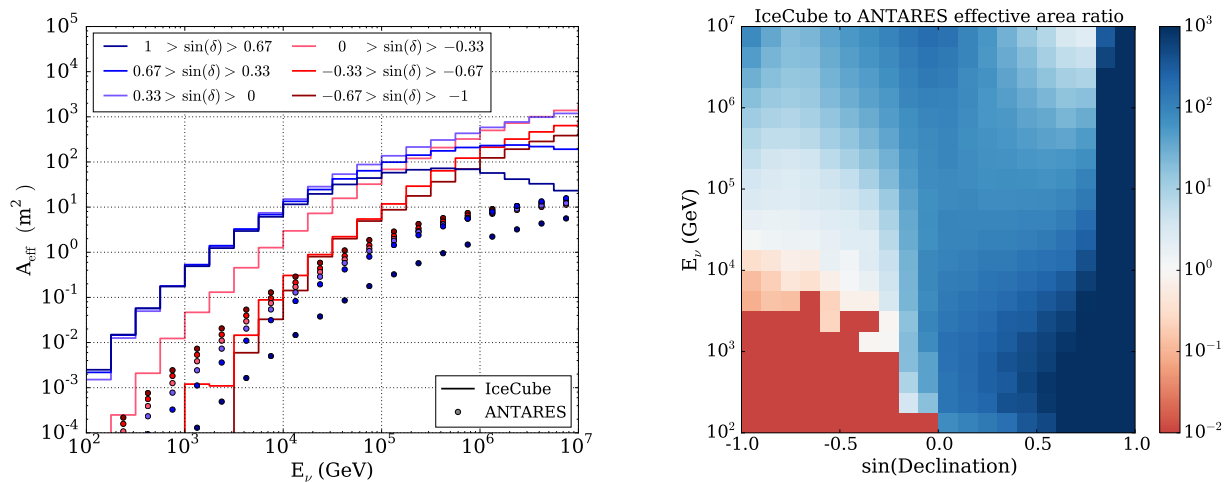
Figure 9. *Left*: The effective area of IceCube to muon neutrinos with energies 100 GeV - 10 PeV is shown for the event selection applied to this analysis' data samples. For comparison, the effective area of the ANTARES observatory's point-source event selection is shown over the same range (circles). Below 1 TeV, the effective area of ANTARES is greater for most of the southern sky and that of IceCube dominates in the north. Above 50 TeV, IceCube's effective area dominates in all declinations in the energy range for which data are available. *Right*: A 2-dimensional plot shows the ratio of the effective areas of IceCube to ANTARES over energy and declination, with a bin-width of 0.1 in $\sin(\delta)$ and bin-height equal to one quarter of a decade in energy. Where ANTARES provides a non-zero effective area, but IceCube's is equal to zero for this event selection, the ratio plotted is the scale minimum 10^{-2}; likewise, where the converse is true, the ratio plotted is the scale maximum 10^3.

plements IceCube in searches for isotropic transient sources, achieving greater effective area in $1/3$ of the sky. Since ANTARES is not located at a pole, the zenith angle of any astrophysical source changes throughout the day, thus detector overburden and sensitivity are time-dependent. Therefore, the effective areas provided by ANTARES for a given declination band are the day-averaged values (Adrian-Martinez et al. 2014). A joint stacking analysis between IceCube and ANTARES (Adrian-Martinez et al. 2016a,b) could maximize the sensitivity of neutrino searches from FRBs across the full sky. Furthermore, with the implementation of the expanding time window techniques, IceCube can now follow up on generic fast transients rapidly, enabling monitoring of the transient sky in the neutrino sector (Aartsen et al. (IceCube Collaboration) 2017f).

REFERENCES

Aartsen et al. (IceCube Collaboration). 2013a, Science, 342   —. 2013b, Phys. Rev. Lett., 111, 021103

—. 2013c, proc. 33rd ICRC, 0492
—. 2014, Phys. Rev. Lett., 113, 101101
—. 2015a, Phys. Rev. D, 91, 022001
—. 2015b, Astrophys. J., 809, 98
—. 2015c, Phys. Rev. Lett., 115, 081102
—. 2015d, Phys. Rev. Lett., 114, 171102
—. 2015e, Astrophys. J. Lett., 805, L5
—. 2015f, Astrophys. J., 805, L5
—. 2016a, Astrophys. J., 833, 3
—. 2016b, Phys. Rev., D93, 022001
—. 2017a, Astrophys. J., 835, 151
—. 2017b, Astrophys. J., 843, 112
—. 2017c, Astrophys. J., 835, 45
—. 2017d, arXiv:1710.01191 [astro-ph.HE]
—. 2017e, JINST, 12, P03012
—. 2017f, Astropart. Phys., 92, 30
Abbasi et al. (IceCube Collaboration). 2011, Astron. Astrophys., 535, A109,
    [Erratum: Astron. Astrophys.563,C1(2014)]
—. 2012, Nature, 484, 351
Adrian-Martinez, S., et al. 2014, Astrophys. J., 786, L5
—. 2016a, Phys. Rev., D93, 122010
—. 2016b, Astrophys. J., 823, 65
Argüelles, C. A., Katori, T., & Salvado, J. 2015, Phys. Rev. Lett., 115,
    161303
Bannister, K., Shannon, R., Macquart, J., et al. 2017, Astrophys. J., 841, L12
Berezinsky, V., Olum, K. D., Sabancilar, E., & Vilenkin, A. 2009, Phys.
    Rev., D80, 023014
Bustamante, M., Beacom, J. F., & Winter, W. 2015, Phys. Rev. Lett., 115,
    161302
Caleb, M., Flynn, C., Bailes, M., et al. 2017, Mon. Not. Roy. Astron. Soc.,
    468, 3746

Chatterjee, S., Law, C. J., Wharton, R. S., et al. 2017, Nature, 541, 58
CHIME Scientific Collaboration. 2017, Astrophys. J., 844, 161
Cordes, J. M., Wharton, R. S., Spitler, L. G., Chatterjee, S., & Wasserman, I.
    2016, arXiv:1605.05890 [astro-ph.HE]
Fahey, S., Kheirandish, A., Vandenbroucke, J., & Xu, D. 2017, Astrophys.
    J., 845, 14
Falcke, H., & Rezzolla, L. 2014, Astron. Astrophys., 562, A137
Li, X., Zhou, B., He, H.-N., Fan, Y.-Z., & Wei, D.-M. 2014, Astrophys. J.,
    797, 33
Lorimer, D. R., Bailes, M., McLaughlin, M. A., Narkevic, D. J., &
    Crawford, F. 2007, Science, 318, 777
Lunardini, C., & Sabancilar, E. 2012, Phys. Rev., D86, 085008
Macquart, J.-P., & Ekers, R. 2017, arXiv:1710.11493 [astro-ph.HE]
Masui, K., Lin, H.-H., Sievers, J., et al. 2015, Nature, 528, 523
Maunu, R. 2016, PhD thesis, University of Maryland (College Park, Md.)
Murase, K., Kashiyama, K., & Mészáros, P. 2016, Mon. Not. Roy. Astron.
    Soc., 461, 1498
Neyman, J. 1937, Phil. Trans. Roy. Soc. Lond., A236, 333
Petroff, E., et al. 2017, Mon. Not. Roy. Astron. Soc., 469, 4465
Rees, M. J. 1977, Nature, 266, 333
Scholz, P., Spitler, L. G., Hessels, J. W. T., et al. 2016, Astrophys. J., 833,
    177
Spitler, L. G., Cordes, J. M., Hessels, J. W. T., et al. 2014, Astrophys. J.,
    790, 101
Stewart, A. J., Fender, R. P., Broderick, J. W., et al. 2016, Mon. Not. Roy.
    Astron. Soc., 456, 2321
Thornton, D., Stappers, B., Bailes, M., et al. 2013, Science, 341, 53
Totani, T. 2013, Pub. Astron. Soc. Jpn., 65, L12
Ye, J., Wang, K., & Cai, Y.-F. 2017, Eur. Phys. J., C77, 720

Bibliography

[1] B. P. Abbott et al. LIGO: The Laser interferometer gravitational-wave observatory. *Rept. Prog. Phys.*, 72:076901, 2009.

[2] F. Acernese et al. Status of VIRGO. *Class. Quant. Grav.*, 22:S869–S880, 2005.

[3] B. P. Abbott et al. Observation of Gravitational Waves from a Binary Black Hole Merger. *Phys. Rev. Lett.*, 116(6):061102, 2016.

[4] J. M. Weisberg, D. J. Nice, and J. H. Taylor. Timing Measurements of the Relativistic Binary Pulsar PSR B1913+16. *Astrophys. J.*, 722:1030–1034, 2010.

[5] T. Akutsu et al. KAGRA: 2.5 Generation Interferometric Gravitational Wave Detector. 2018.

[6] C. S. Unnikrishnan. IndIGO and LIGO-India: Scope and plans for gravitational wave research and precision metrology in India. *Int. J. Mod. Phys.*, D22:1341010, 2013.

[7] Xin-Chun Hu, Xiao-Hong Li, Yan Wang, Wen-Fan Feng, Ming-Yue Zhou, Yi-Ming Hu, Shou-Cun Hu, Jian-Wei Mei, and Cheng-Gang Shao. Fundamentals of the orbit and response for TianQin. *Class. Quant. Grav.*, 35(9):095008, 2018.

[8] V. F. Hess. Über Beobachtungen der durchdringenden Strahlung bei sieben Freiballonfahrten. *Physikalische Zeitschrift*, 13:1084–1091, November 1912.

[9] R. Abbasi et al. Measurement of the Anisotropy of Cosmic Ray Arrival Directions with IceCube. *Astrophys. J.*, 718:L194, 2010.

[10] M. Amenomori et al. On Temporal Variations of the Multi-TeV Cosmic Ray Anisotropy using the Tibet III Air Shower Array. *Astrophys. J.*, 711:119–124, 2010.

[11] C. Patrignani et al. Review of Particle Physics. *Chin. Phys.*, C40(10):100001, 2016.

[12] Alexander Aab et al. The Pierre Auger Cosmic Ray Observatory. *Nucl. Instrum. Meth.*, A798:172–213, 2015.

[13] Ellen G. Zweibel. The microphysics and macrophysics of cosmic rays. *Physics of Plasmas*, 20(5):055501, 2013.

[14] Yousaf Butt. Beyond the myth of the supernova-remnant origin of cosmic rays. *Nature*, 460:701–704, 2009.

[15] R. W. Klebesadel, I. B. Strong, and R. A. Olson. Observations of Gamma-Ray Bursts of Cosmic Origin. *Astrophysical Journal Letters*, 182:L85, June 1973.

[16] M. Su, T. R. Slatyer, and D. P. Finkbeiner. Giant Gamma-ray Bubbles from Fermi-LAT: Active Galactic Nucleus Activity or Bipolar Galactic Wind? *Astrophysical Journal*, 724:1044–1082, December 2010.

[17] R. Buehler, J. D. Scargle, R. D. Blandford, L. Baldini, M. G. Baring, A. Belfiore, E. Charles, J. Chiang, F. D'Ammando, C. D. Dermer, S. Funk, J. E. Grove, A. K. Harding, E. Hays, M. Kerr, F. Massaro, M. N. Mazziotta, R. W. Romani, P. M. Saz Parkinson, A. F. Tennant, and M. C. Weisskopf. Gamma-Ray Activity in the Crab Nebula: The Exceptional Flare of 2011 April. *Astrophysical Journal*, 749:26, April 2012.

[18] Paolo Desiati. IceCube: Toward a km3 Neutrino Telescope. In *Proceedings, 20th European Cosmic Ray Symposium (ECRS 2006): Lisbon, Portugal, September 5-8, 2006*, pages S5–73, 2006.

[19] Bruce T. Cleveland, Timothy Daily, Jr. Raymond Davis, James R. Distel, Kenneth Lande, C. K. Lee, Paul S. Wildenhain, and Jack Ullman. Measurement of the solar electron neutrino flux with the homestake chlorine detector. *The Astrophysical Journal*, 496(1):505, 1998.

[20] Edward Kearns, Takaaki Kajita, and Yoji Totsuka. Detecting massive neutrinos. *Scientific American*, 281(2):64–71, 1999.

[21] Bernhard Voigt. *Sensitivity of the IceCube detector for ultra-high energy electron-neutrino events*. PhD thesis, Humboldt-Universität zu Berlin, Mathematisch-Naturwissenschaftliche Fakultät I, 2008.

[22] Stefaan Tavernier. *Experimental Techniques in Nuclear and Particle Physics*. Springer, Berlin, Germany, 2010.

[23] I. M. Frank and I. E. Tamm. Coherent visible radiation of fast electrons passing through matter. *Compt. Rend. Acad. Sci. URSS*, 14(3):109–114, 1937. [Usp. Fiz. Nauk93,no.2,388(1967)].

[24] Stephen G. Warren and Richard E. Brandt. Optical constants of ice from the ultraviolet to the microwave: A revised compilation. *Journal of Geophysical Research*, 113(D14), 2008.

[25] Dmitry Chirkin and Wolfgang Rhode. Muon Monte Carlo: A High-precision tool for muon propagation through matter. 2004.

[26] M. G. Aartsen et al. The IceCube Neutrino Observatory: Instrumentation and Online Systems. *JINST*, 12(03):P03012, 2017.

[27] M. G. Aartsen et al. Evidence for High-Energy Extraterrestrial Neutrinos at the IceCube Detector. *Science*, 342:1242856, 2013.

[28] M. G. Aartsen et al. Evidence for Astrophysical Muon Neutrinos from the Northern Sky with IceCube. *Phys. Rev. Lett.*, 115(8):081102, 2015.

[29] J. G. Learned and K. Mannheim. High-energy neutrino astrophysics. *Ann. Rev. Nucl. Part. Sci.*, 50:679–749, 2000.

[30] Kai Schatto. *Stacked searches for high-energy neutrinos from blazars with IceCube.* Univ., Mainz, 2014.

[31] M. G. Aartsen et al. Observation of High-Energy Astrophysical Neutrinos in Three Years of IceCube Data. *Phys. Rev. Lett.*, 113:101101, 2014.

[32] M. G. Aartsen et al. All-sky Search for Time-integrated Neutrino Emission from Astrophysical Sources with 7 yr of IceCube Data. *Astrophys. J.*, 835(2):151, 2017.

[33] M. G. Aartsen et al. Development of a General Analysis and Unfolding Scheme and its Application to Measure the Energy Spectrum of Atmospheric Neutrinos with IceCube. *Eur. Phys. J.*, C75(3):116, 2015.

[34] Delia Tosi. Astrophysical neutrinos: IceCube highlights. *Nucl. Part. Phys. Proc.*, 291-293:167–174, 2017.

[35] M. G. Aartsen et al. Neutrino emission from the direction of the blazar TXS 0506+056 prior to the IceCube-170922A alert. *Science*, 361(6398):147–151, 2018.

[36] M.G. Aartsen et al. Multimessenger observations of a flaring blazar coincident with high-energy neutrino IceCube-170922A. *Science*, 361(6398):eaat1378, 2018.

[37] M. G. Aartsen et al. The contribution of Fermi-2LAC blazars to the diffuse TeV-PeV neutrino flux. *Astrophys. J.*, 835(1):45, 2017.

[38] M. G. Aartsen et al. Search for Transient Astrophysical Neutrino Emission with IceCube-DeepCore. *Astrophys. J.*, 816(2):75, 2016.

[39] M. G. Aartsen et al. Constraints on Galactic Neutrino Emission with Seven Years of IceCube Data. *Astrophys. J.*, 849(1):67, 2017.

[40] M. G. Aartsen et al. Search for Prompt Neutrino Emission from Gamma-Ray Bursts with IceCube. *Astrophys. J.*, 805(1):L5, 2015.

[41] M. G. Aartsen et al. Constraints on minute-scale transient astrophysical neutrino sources. *Submitted to: Phys. Rev. Lett.*, 2018.

[42] Thomas Callister, Jonah Kanner, and Alan Weinstein. Gravitational-Wave Constraints on the Progenitors of Fast Radio Bursts. *Astrophys. J.*, 825(1):L12, 2016.

[43] A. A. Penzias and R. W. Wilson. A Measurement of Excess Antenna Temperature at 4080 Mc/s. *Astrophys. J.*, 142:419–421, July 1965.

[44] H. Al Noori, M. S. E. Roberts, D. Champion, M. McLaughlin, Scott Ransom, and P. S. Ray. A search for extragalactic pulsars in the local group galaxies IC 10 and Barnard's galaxy. In *Journal of Physics Conference Series*, volume 869 of *Journal of Physics Conference Series*, 2017.

[45] Maura A. McLaughlin et al. Transient radio bursts from rotating neutron stars. *Nature*, 439:817, 2006.

[46] S. Burke-Spolaor. Rotating Radio Transients and their place among pulsars. In Joeri van Leeuwen, editor, *Neutron Stars and Pulsars: Challenges and Opportunities after 80 years*, volume 291 of *IAU Symposium*, pages 95–100, March 2013.

[47] E. F. Keane and M. A. McLaughlin. Rotating radio transients. *Bulletin of the Astronomical Society of India*, 39:333–352, September 2011.

[48] D. R. Lorimer, M. Bailes, M. A. McLaughlin, D. J. Narkevic, and F. Crawford. A bright millisecond radio burst of extragalactic origin. *Science*, 318(5851):777–780, 2007.

[49] S. Burke-Spolaor et al. Radio Bursts with Extragalactic Spectral Characteristics Show Terrestrial Origins. *The Astrophysical Journal*, 727, 2011.

[50] L. G. Spitler et al. Fast Radio Burst Discovered in the Arecibo Pulsar ALFA Survey. *Astrophys. J.*, 790(2):101, 2014.

[51] E. Petroff et al. Identifying the source of perytons at the Parkes radio telescope. *Mon. Not. Roy. Astron. Soc.*, 451(4):3933–3940, 2015.

[52] Kiyoshi Masui et al. Dense magnetized plasma associated with a fast radio burst. *Nature*, 528:523, 2015.

[53] J. I. Katz. Fast radio bursts — A brief review: Some questions, fewer answers. *Mod. Phys. Lett.*, A31(14):1630013, 2016.

[54] E. Petroff et al. A survey of FRB fields: Limits on repeatability. *Mon. Not. Roy. Astron. Soc.*, 454(1):457–462, 2015.

[55] L. G. Spitler et al. A Repeating Fast Radio Burst. *Nature*, 531:202, 2016.

[56] Martin J Rees. A better way of searching for black-hole explosions? *Nature*, 266(5600):333–334, 1977.

[57] Heino Falcke and Luciano Rezzolla. Fast radio bursts: the last sign of supramassive neutron stars. *Astron. Astrophys.*, 562:A137, 2014.

[58] Tomonori Totani. Cosmological Fast Radio Bursts from Binary Neutron Star Mergers. *Pub. Astron. Soc. Jpn.*, 65:L12, 2013.

[59] E. Petroff, M. J. Keith, S. Johnston, W. van Straten, and R. M. Shannon. Dispersion measure variations in a sample of 168 pulsars. *Mon. Not. Roy. Astron. Soc.*, 435:1610, 2013.

[60] Bi-Ping Gong. Variation of dispersion measure: evidence of geodetic precession of binary pulsars. 2003.

[61] E. Y. Nugaev, G. I. Rubtsov, and Y. V. Zhezher. Probing Milky Way's hot gas halo density distribution using the dispersion measure of pulsars. *ArXiv e-prints*, September 2015.

[62] J. M. Cordes, R. S. Wharton, L. G. Spitler, S. Chatterjee, and I. Wasserman. Radio Wave Propagation and the Provenance of Fast Radio Bursts. *ArXiv e-prints*, 2016.

[63] E. F. Keane and E. Petroff. Fast radio bursts: search sensitivities and completeness. *Mon. Not. Roy. Astron. Soc.*, 447:2852, 2015.

[64] D. J. Champion et al. Five new fast radio bursts from the HTRU high-latitude survey at Parkes: first evidence for two-component bursts. *Mon. Not. Roy. Astron. Soc.*, 460(1):L30–L34, 2016.

[65] A. Rane, D. R. Lorimer, S. D. Bates, N. McMann, M. A. McLaughlin, and K. Rajwade. A search for rotating radio transients and fast radio bursts in the Parkes high-latitude pulsar survey. *Mon. Not. Roy. Astron. Soc.*, 455(2):2207–2215, 2016.

[66] M. Caleb et al. The first interferometric detections of Fast Radio Bursts. *Mon. Not. Roy. Astron. Soc.*, 468(3):3746–3756, 2017.

[67] R. M. Shannon et al. The dispersion–brightness relation for fast radio bursts from a wide-field survey. *Nature*, 2018.

[68] J. W. T. Hessels. Fast Radio Bursts and their Possible Neutron Star Origins. In *J.W.T. Hessels 2017 J. Phys.: Conf. Ser. 932 012025, J.W.T. Hessels 2017 J. Phys.: Conf. Ser. 932 012025*, 2018.

[69] CHIME Collaboration. The CHIME Fast Radio Burst Project: System Overview. *Astrophys. J., archivePrefix =*.

[70] J. J. DeLaunay, D. B. Fox, K. Murase, P. Mészáros, A. Keivani, C. Messick, M. A. Mostafá, F. Oikonomou, G. Tešić, and C. F. Turley. Discovery of a transient gamma-ray counterpart to FRB 131104. *Astrophys. J.*, 832(1):L1, 2016.

[71] R. M. Shannon and V. Ravi. Radio-interferometric monitoring of FRB 131104: A coincident AGN flare, but no evidence for a cosmic fireball. *Astrophys. J.*, 837(2):L22, 2017.

[72] Shao-Qiang Xi, Pak-Hin Thomas Tam, Fang-Kun Peng, and Xiang-Yu Wang. Search for GeV counterparts to fast radio bursts with Fermi. *Astrophys. J.*, 842(1):L8, 2017.

[73] S. Chatterjee et al. The direct localization of a fast radio burst and its host. *Nature*, 541:58, 2017.

[74] Shriharsh P. Tendulkar et al. The Host Galaxy and Redshift of the Repeating Fast Radio Burst FRB 121102. *Astrophys. J.*, 834(2):L7, 2017.

[75] Samuel Fahey, Ali Kheirandish, Justin Vandenbroucke, and Donglian Xu. A search for neutrinos from fast radio bursts with IceCube. *Astrophys. J.*, 845(1):14, 2017.

[76] M. G. Aartsen et al. A Search for Neutrino Emission from Fast Radio Bursts with Six Years of IceCube Data. *Astrophys. J.*, 857(2):117, 2018.

[77] A. Albert et al. Search for high-energy neutrinos in coincidence with Fast Radio Bursts with the ANTARES neutrino telescope. 2018.

[78] R. Abbasi et al. Search for Muon Neutrinos from Gamma-ray Bursts with the IceCube Neutrino Telescope. *Astrophys. J.*, 710:346–359, February 2010.

[79] D. Thornton et al. A Population of Fast Radio Bursts at Cosmological Distances. *Science*, 341(6141):53–56, 2013.

[80] Yue Zhang, Jin-Jun Geng, and Yong-Feng Huang. Fast Radio Bursts from the collapse of Strange Star Crusts. *Astrophys. J.*, 858(2):88, 2018.

[81] J. J. Geng and Y. F. Huang. Fast Radio Bursts: Collisions between Neutron Stars and Asteroids/Comets. *Astrophys. J.*, 809(1):24, 2015.

[82] Z. G. Dai, J. S. Wang, X. F. Wu, and Y. F. Huang. Repeating Fast Radio Bursts from Highly Magnetized Pulsars Travelling through Asteroid Belts. *Astrophys. J.*, 829(1):27, 2016.

[83] E. Platts, A. Weltman, A. Walters, S. P. Tendulkar, J. E. B. Gordin, and S. Kandhai. A Living Theory Catalogue for Fast Radio Bursts. 2018.

[84] M. G. Aartsen et al. Searches for Extended and Point-like Neutrino Sources with Four Years of IceCube Data. *Astrophys. J.*, 796(2):109, 2014.

[85] Jim Braun, Jon Dumm, Francesco De Palma, Chad Finley, Albrecht Karle, and Teresa Montaruli. Methods for point source analysis in high energy neutrino telescopes. *Astropart. Phys.*, 29:299–305, 2008.

[86] Michael Richman. *A Search For Muon Neutrinos Coincident With Gamma-Ray Bursts Using IceCube.* PhD thesis, University of Maryland (College Park, Md.), 2015. doi:10.13016/M2CS5W.

[87] Ryan Maunu. *A Search for Muon Neutrinos in Coincidence with Gamma-Ray Bursts in the Southern Hemisphere Sky Using the IceCube Neutrino Observatory.* PhD thesis, University of Maryland (College Park, Md.), 2016. doi:10.13016/M2449P.

[88] M. G. Aartsen et al. Searches for Time Dependent Neutrino Sources with IceCube Data from 2008 to 2012. *Astrophys. J.*, 807(1):46, 2015.

[89] Aartsen et al. (IceCube Collaboration). The IceCube Neutrino Observatory Part II: Atmospheric and Diffuse UHE Neutrino Searches of All Flavors. 2013. Proc. 33rd ICRC, 0492.

[90] Liam Connor and Emily Petroff. On detecting repetition from fast radio bursts. *Astrophys. J.*, 861(1):L1, 2018.

[91] M. G. Aartsen et al. The IceCube Neutrino Observatory - Contributions to ICRC 2017 Part II: Properties of the Atmospheric and Astrophysical Neutrino Flux. 2017.

[92] E. Petroff, E. D. Barr, A. Jameson, E. F. Keane, M. Bailes, M. Kramer, V. Morello, D. Tabbara, and W. van Straten. FRBCAT: The Fast Radio Burst Catalogue. *Publ. Astron. Soc. Austral.*, 33:e045, 2016.

[93] D. E. Osterbrock. Who Really Coined the Word Supernova? Who First Predicted Neutron Stars? In *American Astronomical Society Meeting Abstracts*, volume 33 of *Bulletin of the American Astronomical Society*, page 1330, December 2001.

[94] A. H. Joy. Spectroscopic Observations of AE Aquarii. *Astrophysical Journal*, 120:377, November 1954.

[95] J. A. Crawford and R. P. Kraft. An Intrepetation of AE Aquarii. *Astrophysical Journal*, 123:44, January 1956.

[96] M. J. Darnley, V. A. R. M. Ribeiro, M. F. Bode, R. A. Hounsell, and R. P. Williams. On the Progenitors of Galactic Novae. *Astrophysical Journal*, 746:61, February 2012.

[97] J. W. Truran and M. Livio. On the frequency of occurrence of oxygen-neon-magnesium white dwarfs in classical nova systems. *Astrophysical Journal*, 308:721–727, September 1986.

[98] G. L. Bryan and S. Kwok. Energy distributions of symbiotic novae. *Astrophys. J.*, 368:252–260, February 1991.

[99] A. A. Abdo et al. Gamma-Ray Emission Concurrent with the Nova in the Symbiotic Binary V407 Cygni. *Science*, 329:817–821, 2010.

[100] M. Ackermann et al. Fermi Establishes Classical Novae as a Distinct Class of Gamma-Ray Sources. *Science*, 345:554–558, 2014.

[101] A. Franckowiak, P. Jean, M. Wood, C. C. Cheung, and S. Buson. Search for Gamma-ray Emission from Galactic Novae with the Fermi-LAT. *Astron. Astrophys.*, 609:A120, 2018.

[102] Kwan-Lok Li et al. A Nova Outburst Powered by Shocks. *Nat. Astron.*, 1(10):697–702, 2017.

[103] E. Aydi et al. Multiwavelength observations of V407 Lupi (ASASSN-16kt) – a very fast nova erupting in an intermediate polar. *Mon. Not. Roy. Astron. Soc.*, 480(1):572–609, 2018.

[104] Brian D. Metzger, Damiano Caprioli, Indrek Vurm, Andrei M. Beloborodov, Imre Bartos, and Andrey Vlasov. Novae as Tevatrons: Prospects for CTA and IceCube. *Mon. Not. Roy. Astron. Soc.*, 457(2):1786–1795, 2016.

[105] Jacob Daughhetee. *Search for neutrino transients using IceCube and DeepCore*. PhD thesis, Georgie Tech, 2015.

[106] S. Adrian-Martinez et al. Search for Cosmic Neutrino Point Sources with Four Year Data of the ANTARES Telescope. *Astrophys. J.*, 760:53, 2012.

[107] M. G. Aartsen et al. Determining neutrino oscillation parameters from atmospheric muon neutrino disappearance with three years of IceCube DeepCore data. *Phys. Rev.*, D91(7):072004, 2015.

[108] M. G. Aartsen et al. The IceCube Neutrino Observatory Part VI: Ice Properties, Reconstruction and Future Developments. In *Proceedings, 33rd International Cosmic Ray Conference (ICRC2013): Rio de Janeiro, Brazil, July 2-9, 2013*, 2013.

[109] E. Richard et al. Measurements of the atmospheric neutrino flux by Super-Kamiokande: energy spectra, geomagnetic effects, and solar modulation. *Phys. Rev.*, D94(5):052001, 2016.